
Electronic Thesis and Dissertation Repository

10-25-2018 2:00 PM

Quantitative Analysis of Three-Dimensional Cone-Beam Computed Tomography Using Image Quality Phantoms

Rudy Baronette, *The University of Western Ontario*

Supervisor: Holdsworth, David W., *The University of Western Ontario*

Co-Supervisor: Teeter, Matthew G., *The University of Western Ontario*

A thesis submitted in partial fulfillment of the requirements for the Master of Science degree in Medical Biophysics

© Rudy Baronette 2018

Follow this and additional works at: <https://ir.lib.uwo.ca/etd>



Part of the [Medical Biophysics Commons](#)

Recommended Citation

Baronette, Rudy, "Quantitative Analysis of Three-Dimensional Cone-Beam Computed Tomography Using Image Quality Phantoms" (2018). *Electronic Thesis and Dissertation Repository*. 5797.
<https://ir.lib.uwo.ca/etd/5797>

This Dissertation/Thesis is brought to you for free and open access by Scholarship@Western. It has been accepted for inclusion in Electronic Thesis and Dissertation Repository by an authorized administrator of Scholarship@Western. For more information, please contact wlsadmin@uwo.ca.

Abstract

In the clinical setting, weight-bearing static 2D radiographic imaging and supine 3D radiographic imaging modalities are used to evaluate radiographic changes such as, joint space narrowing, subchondral sclerosis, and osteophyte formation. These respective imaging modalities cannot distinguish between tissues with similar densities (2D imaging), and do not accurately represent functional joint loading (supine 3D imaging). Recent advances in cone-beam CT (CBCT) have allowed for scanner designs that can obtain weight-bearing 3D volumetric scans. The purpose of this thesis was to analyze, design, and implement advanced imaging techniques to quantify image quality parameters of reconstructed image volumes generated by a commercially-available CBCT scanner, and a novel ceiling-mounted CBCT scanner. In addition, imperfections during rotation of the novel ceiling-mounted CBCT scanner were characterized using a 3D printed calibration object with a modification to the single marker bead method, and prospective geometric calibration matrices.

Keywords

cone-beam CT, geometric calibration, image-based corrections, image quality, joint space narrowing, joint loading, knee, osteoarthritis, quantitative analysis, single-plane fluoroscopy, weight-bearing

Co-Authorship Statement

The following thesis contains manuscripts intended for publication within scientific journals. Chapter 2 is an original manuscript entitled, “Quantitative Performance Evaluation of a Peripheral Cone-Beam Computed Tomography Scanner with Weight-bearing Capabilities.” The manuscript is co-authored by Rudolphe J. Baronette, Xunhua Yuan, Steven I. Pollmann, Matthew G. Teeter, and David W. Holdsworth. In my role as a MSc candidate, I participated in designing the study, performed cone-beam CT scans and reconstruction, performed the effective dose estimation, analyzed all data, performed the statistical analysis, and wrote the manuscript text. Xunhua Yuan and Steven I. Pollmann advised on study design, interpretation of the data, and provided editorial input. Matthew Teeter and David Holdsworth, as the candidate’s supervisors, designed the study, reviewed the results, gave editorial assistance and provided mentorship.

Chapter 3 is an or original manuscript entitled, “Three-dimensional cone-beam CT reconstruction in a natural weight-bearing stance using ceiling-mounted x-ray fluoroscopy.” The manuscript is co-authored by Rudolphe J. Baronette, Steven I. Pollmann, Matthew G. Teeter, and David W. Holdsworth. In my role as a MSc candidate, I participated in designing the study, performed cone-beam CT scans and reconstruction, performed the effective dose estimation, characterized gantry motion, analyzed all data, performed the statistical analysis, and wrote the manuscript text. Steven I. Pollmann advised on study design, and interpretation of the data. Matthew Teeter and David Holdsworth, as the candidate’s supervisors, designed the study, reviewed the results, gave editorial assistance and provided mentorship.

Acknowledgments

I would like to begin by thanking my primary supervisor, Dr. David Holdsworth, for this opportunity and his mentorship throughout my graduate education. He has helped me to increase my understanding of x-ray imaging system, develop a thorough method for problem solving, improve my communication of my scientific research, and has provided valuable insight to each of my projects. I would also like to thank my co-supervisor Dr. Matthew Teeter, specifically for helping to improve my communication, and providing opportunities to apply clinical skills in the radiostereometric analysis lab. As a member of my advisory committee, Dr. Trevor Birmingham has provided invaluable clinical insights for applications and advantages of my work. The accomplishments within this thesis could not have happened without the support of individuals within the Holdsworth group at Robarts Research Institute. Specifically, Steve Pollmann, who created numerous programs for me and was always willing to provide advice on whatever challenge I was facing, and Jeremy Gill for his help in developing the orbital acquisition protocol, angular encoder, and geometric calibration in my 2nd project. I would also like to thank Dr. Xunhua Yuan, who helped with much of the geometric calibration work, gave me a comprehensive background in radiostereometric analysis, and was always willing to share his scientific wisdom. Finally, I would like to thank my family and friends for their support during this journey. This includes my parents Gary and Kathy, my sister Savannah, my brother Oliver, my aunt Simone, and especially my girlfriend Sarah who has supported me throughout my graduate education.

List of Abbreviations

2D	two-dimensional
3D	three-dimensional
ADU	analog-to-digital unit
AINO	adaptive imaging noise optimization
BMD	bone-mineral density
CBCT	Cone-beam computed tomography
CT	computed tomography
CTDI	computed tomography dose index
FOV	field-of-view
GRAIL	gait real-time analysis interactive lab
HU	Hounsfield unit
kVp	kilovoltage peak
LAC	linear attenuation coefficient
lp/mm	line pairs per millimetre
mA	milliamperes
mAs	milliampere seconds
MBRSA	model-based radiostereometric analysis
mm	millimetre
MRI	magnetic resonance imaging

MTF	modulation transfer function
NSAIDs	non-steroidal anti-inflammatory drugs
OA	osteoarthritis
PLA	polylactic acid
ROI	region of interest
RSA	radiostereometric analysis
RSPA	roentgen single-plane photogrammetry
TKA	total knee arthroplasty
µm	micrometre or micron

Table of Contents

Abstract.....	i
Co-Authorship Statement.....	ii
Acknowledgments.....	iii
List of Abbreviations	iv
Table of Contents	vi
List of Tables	ix
List of Figures	x
Chapter 1.....	1
1 Introduction.....	1
1.1 Knee Osteoarthritis	1
1.2 Review of Current Methods for Knee Motion Analysis.....	2
1.2.1 3D Motion Capture Gait Analysis	2
1.2.2 Radiography.....	4
1.2.3 Radiostereometric Analysis	4
1.2.4 Fluoroscopy.....	7
1.2.5 Computed Tomography	9
1.2.6 Cone-beam Computed Tomography.....	10
1.3 Thesis Objectives and Hypotheses.....	12
1.4 Thesis Organization	13
1.5 References.....	13
Chapter 2.....	22
2 Quantitative Performance Evaluation of a Peripheral Cone-Beam Computed Tomography Scanner with Weight-bearing Capabilities.....	22
2.1 Introduction.....	22
2.2 Methods.....	23

2.2.1	Extremity CT Scanner.....	23
2.2.2	Image quality phantoms and data acquisition.....	24
2.2.3	Spatial Resolution.....	26
2.2.4	Linearity.....	29
2.2.5	Uniformity.....	29
2.2.6	Noise.....	30
2.2.7	Geometric Accuracy.....	32
2.2.8	Effective Dose Estimation.....	32
2.2.9	Statistical Analysis.....	33
2.3	Results.....	33
2.3.1	Spatial Resolution.....	33
2.3.2	Linearity.....	35
2.3.3	Uniformity.....	39
2.3.4	Noise.....	42
2.3.5	Geometric Accuracy.....	43
2.3.6	Effective Dose Estimation.....	44
2.4	Discussion.....	44
2.5	Conclusion.....	48
2.6	References.....	48
Chapter 3	54
3	Three-dimensional cone-beam CT reconstruction in a natural weight-bearing stance using ceiling-mounted x-ray fluoroscopy.....	54
3.1	Introduction.....	54
3.2	Methods.....	56
3.2.1	Data Acquisition.....	56
3.2.2	Flat-panel detector linearity.....	58

3.2.3	Ceiling-mounted gantry motion characterization	58
3.2.4	Effective Dose Estimation	62
3.2.5	Image Quality Assessment.....	62
3.3	Results.....	69
3.3.1	Flat-panel detector linearity	69
3.3.2	Ceiling-mounted Gantry Rotation Reproducibility	70
3.3.3	Geometric Projection Matrices Reproducibility	73
3.3.4	Spatial Resolution	75
3.3.5	Linearity	76
3.3.6	Noise	76
3.3.7	Uniformity.....	77
3.3.8	Geometric Accuracy	78
3.3.9	3D Printed Calibration Cube.....	79
3.3.10	Cadaveric Specimen.....	80
3.3.11	Effective Dose Estimation	81
3.4	Discussion	81
3.5	Conclusion	85
3.6	References.....	85
Chapter 4	91
4	Conclusions and Future Directions	91
4.1	Summary of Results	91
4.1.1	Related Future Directions	94
4.2	References.....	95
Curriculum Vitae	97

List of Tables

Table 2.1: Manufacturer’s clinical imaging standards for spatial resolution, linearity, uniformity, noise, and geometric accuracy. 26

Table 2.2: CT numbers (HU) and standard deviation (HU), measured in one central and four peripheral ROIs for the 300-image projection protocol in the small phantom. Average difference and average measured standard deviation (\pm SD) were calculated. 38

Table 2.3: CT numbers (HU) and standard deviation (HU), measured in one central and four peripheral ROIs for 450-image projection protocol in the small phantom. Average difference and average measured standard deviation (\pm SD) were calculated..... 38

Table 2.4: CT numbers (HU) and standard deviation (HU), measured in one central and four peripheral ROIs for the 300-image projection protocol in the large phantom. Average difference and average measured standard deviation (\pm SD) were calculated. 38

Table 2.5: CT numbers (HU) and standard deviation (HU), measured in one central and four peripheral ROIs for the 450-image projection protocol in the large phantom. Average difference and average measured standard deviation (\pm SD) were calculated. 39

Table 2.6: Results of non-linear regression of standard deviations occurring in the small and large phantoms. The equations are shown in the form, $\sigma_{\text{total}}^2 = A * E^{-1} + \sigma_{\text{system}}^2$, where R^2 value for all equations = 0.99..... 42

Table 3.1: Geometric projection matrices calculated using the calibration algorithm within a day, summarizing magnitude and reproducibility of geometric imperfections. Geometric imperfections were reported as the maximum deviation from the average value during rotation. Geometric reproducibility was defined as the average standard deviation across multiple acquisitions within a day. 73

Table 3.2: CT numbers (HU) and standard deviation (HU), measured in one central and four peripheral ROIs for reconstructed image volumes at the central slice. Average difference and average measured standard deviation (\pm SD) were calculated. 77

List of Figures

Figure 1.1: Gait real-time interactive analysis lab (GRAIL) located at the Wolf Orthopaedic Biomechanics Laboratory.	3
Figure 1.2: Example of bi-planar setup in the radiostereometric analysis lab located at Robarts Research Institute.	6
Figure 1.3: Radiostereometric analysis calibration cage for a bi-planar examination.....	7
Figure 1.4: NRT Adora X-ray Fluoroscopy system pictured at the Wolf Orthopaedic Biomechanics Laboratory.	9
Figure 1.5: Planmed Verity extremity cone-beam computed tomography scanner located at the Wolf Orthopaedic Biomechanics Laboratory.	12
Figure 2.1: Peripheral cone-beam CT scanner pictured in conventional scan (a) mode and weight-bearing scan (b) mode.....	24
Figure 2.2: Large custom-built phantom (left) and small phantom (right) designed to evaluate the performance of cone-beam CT scanners.....	25
Figure 2.3: Images of small phantom a) resolution coils, created with alternating aluminum and Mylar sheets, b) the 5° axial slanted-edge image. In the large phantom, c) bar pattern plate, created with alternating aluminum and Mylar sheets, and d) the axial slanted-edge image, showing a 5° from the central axis.....	28
Figure 2.4: Image of linearity plates used in the small phantom (a) containing vials of air, water, and iodine (Omnipaque) in various concentrations, measured in mg ml ⁻¹ . Image of linearity plate in large phantom (b) containing plastics within various bone mineral densities, measured in mg hydroxyapatite cm ⁻³	29
Figure 2.5: Slices through an area of uniform density in the small (a) and large (b) phantoms, show the location of the line profile used to characterize system uniformity. ROIs located	

within the small (c) and large (d) phantoms used to assess uniformity (red & yellow) and noise (red only).	31
Figure 2.6: a) slice from small phantom with five steel beads in axial plane. b) Slices from large phantom containing: five steel beads in the axial plane, and c) in (x-z) direction with thirty tungsten-carbide beads spaced 15 mm in all directions.	32
Figure 2.7: Modulation transfer function of the cone-beam CT system measured from the slanted-edge plate (lines) and resolution coils (symbols) of the small phantom using the 6s (a) and 9s (b) exposure acquisitions.	34
Figure 2.8: Modulation transfer function of the cone-beam CT system measured from the slanted-edge (line) and bar patterns (symbols) in the large phantom, using (a) 6s and (b) 9s exposures. Additionally, modulation transfer function evaluated with the slanted-edge located within the x-y plane in the large phantom, using (c) 6 and (d) 9s exposures.	35
Figure 2.9: Plots of measured CT number versus known iodine concentrations, including results of linear regression, within the linearity plate of small phantom using the (a) 300- and (b) 450- image projection protocols. Plots of measured CT number versus known bone mineral densities, including results of linear regression, within the linearity plate of large phantom using the (c) 300- and (d) 450-image projection protocols. A beam-hardening correction was applied to images of the large phantom using the (e) 300- and (f) 450- image projection protocols.	37
Figure 2.10: Radial signal profiles taken through the centre of the small phantom using the: (a) current, (b) current with AINO, (c) beta, and (d) beta with AINO reconstruction algorithms. All line profiles were obtained on the central reconstructed slice.	40
Figure 2.11: Radial signal profiles taken through the centre of the large phantom using the: (a) current, (b) current with AINO, (c) beta, (d) beta with AINO, (e) beam-hardening correction, and (f) beam-hardening correction with AINO reconstruction algorithms. All line profiles were obtained on the central reconstructed slice.	41
Figure 2.12: Measured noise in the small phantom using the 300 frame (a) and 450 frame (b) protocols, expressed as average standard deviation of the signal intensity (HU), plotted as a	

function of increasing exposure. Tube voltage used for the small phantom was 90 kVp, with tube current varying from 1 to 12 mA, using 6s (a) or 9s (b) exposure time. Similarly, measured noise in the large phantom using the 300 frame (c) and 450 frame (d) protocols, expressed as average standard deviation of the signal intensity (HU), plotted as a function of increasing exposure. Tube voltage used for the large phantom was 96 kVp, with tube current varying from 1 to 12 mA, using 6s (c) or 9s (d) exposure time..... 43

Figure 3.1: Ceiling-mounted x-ray fluoroscopy system setup for an upright acquisition of an image quality phantom..... 58

Figure 3.2: Image of the 3D-printed calibration phantom (left) with a sample x-ray projection image (right) showing the locations of each marker bead at each vertex were used to characterize gantry motion..... 59

Figure 3.3: Schematic diagram of the acquisition geometry depicting a point projection of an object located in 3D (X, Y, Z) onto a 2D detector (U, V). 61

Figure 3.4: Reconstructed slice from the image quality phantom depicting (a) uncorrected and (b) corrected slanted-edge image, showing a 5° from the central axis, and an (c) uncorrected and (d) corrected bar pattern plate, created with alternating aluminum and Mylar sheets..... 64

Figure 3.5: Reconstructed (a) uncorrected and (b) corrected linearity slice containing various bone mineral densities representing materials encountered in musculoskeletal imaging, measured in mg hydroxyapatite cm⁻³ 65

Figure 3.6: (a) Uncorrected and (b) corrected reconstructed slice through an area of uniform density. (c) ROIs used to assess noise (red only) and uniformity (red & yellow). (d) The location of line profile used to analyze variation of CT numbers across the field-of-view (FOV)..... 66

Figure 3.7: Reconstructed (a) uncorrected and (b) corrected slices from image quality phantom with five steel beads in axial plane. (c) uncorrected and (d) corrected slices in X-Y direction with thirty tungsten-carbide beads spaced 15 mm in all directions..... 68

Figure 3.8: Various plots with non-linear best-fit lines illustrating the relationships between (a) x-ray photon fluence and total copper sheet thickness, (b) signal intensity and total copper sheet thickness, (c) signal intensity and x-ray photon fluence, and (d) bright-field corrected signal intensity and x-ray photon fluence. 70

Figure 3.9: (a) Comparison of centroid trajectory of a single high-contrast marker bead versus the averaged U coordinates of the eight diametrically opposed vertices of the 3D printed calibration cube, where the thick line indicates the best-fit sinusoid. (b) The resulting residual plot from a sinusoidal fit is plotted as a function of angle, calculated by subtracting the measured centroid location from the best-fit line. 71

Figure 3.10: (a) Comparison five acquisitions of centroid trajectory of the averaged U coordinates of the eight diametrically opposed vertices of the 3D printed calibration cube, where the thick line indicates the best-fit sinusoid. (b) The resulting residual plot. 71

Figure 3.11: (a) Comparison five acquisitions of centroid trajectory of the averaged V coordinates of the eight diametrically opposed vertices of the 3D printed calibration cube, where the thick line indicates the best-fit sinusoid. (b) The resulting residual plot from a sinusoidal fit are plotted as a function of angle, determined by subtracting the measured centroid location from the best-fit line..... 72

Figure 3.12: Average deviations in (a) τ and (b) ξ as a function of angle, acquired at intervals over a year. 73

Figure 3.13: Reproducibility of prospective geometric parameters that include: (a) the location of the piercing point (U_0 , V_0) and source-to-detector distance (SDD), (b) extrinsic translations (T_x , T_y , T_z), and (c) extrinsic rotations (R_x , R_y , R_z). Parameters are plotted as a difference from their average value during gantry rotation. 74

Figure 3.14: Evaluation of modulation transfer function of reconstructed image volumes using bar patterns in the axial direction, as well as slanted-edge images in the axial and X-Y planes. 75

Figure 3.15: Results of linear regression from analysis of bone mineral densities analyzed in the reconstructed linearity plate of the image quality phantom. 76

Figure 3.16: Measured noise from resulting image reconstructions, expressed as standard deviation within a uniform ROI, plotted as a function of increasing radiation exposure. 77

Figure 3.17: Radial signal profile plotted across the central slice of a reconstructed image volume. (120 kVp, 64 mAs) 78

Figure 3.18: Reconstructed axial slices taken from the top, middle, and bottom of uncorrected (a-c) and corrected (d-f) image volumes, respectively. 79

Figure 3.19: Projection views of the frozen cadaveric knee in the axial, coronal, and sagittal planes. The uncorrected (a-c), residual-corrected (d-f), and artefact-corrected (g-i) reconstructed image volumes..... 80

Chapter 1

1 Introduction

1.1 Knee Osteoarthritis

Osteoarthritis (OA) is the most common musculoskeletal disease, impacting approximately 10-15% of adults over the age of sixty.³⁴ Although this disease is most common in the hip and knee, the diagnosis of knee OA – whether by symptoms and radiographic changes, or by radiographic criteria alone – is more prevalent than hip OA.⁹⁷ Symptoms of OA may include pain, stiffness, and limited joint function.²¹ With respect to radiographic changes, OA is mainly characterized by joint space narrowing, subchondral sclerosis, and osteophyte formation.⁷² Non-operative treatment strategies aim to reduce pain and physical disability to limit structural deterioration in affected joints using non-pharmaceutical methods such as weight loss and aerobic exercise, as well as pharmaceutical methods including: non-steroidal anti-inflammatory drugs (NSAIDs), corticosteroid injections, hyaluronic acid injections, and glucosamine.^{39, 89, 91} The surgical option may be a partial- or total-knee arthroplasty (TKA), which are both intended to reduce pain and improve knee function in patients.¹⁹

The initiation and progression of knee OA has been related to the mechanics of ambulation.⁶ Changes resulting from OA are most frequently observed in the medial compartment, compared to the lateral or patellofemoral compartments of the knee.⁶⁹ Patients can functionally adapt to pathological joint changes such as a ligament injury or articular cartilage degeneration.⁶ For example, it has been observed from *in vivo* studies that some patients with knee OA develop new gait patterns to lower the load at the knee and reduce the rate at which OA progresses.^{7, 49, 69} Consequently, these changes in gait may increase the loads observed in other joints in the lower extremity (hip, knee, and ankle).^{5, 69}

Total knee arthroplasty has become the gold standard for management of severe OA of the knee, since it has been proven as a safe and cost-effective method.^{36, 58, 73, 96} Knee joint replacement is one of the most effective ways to reduce pain and improve function

for patients with end-stage OA.^{38, 56} In Canada, hip and knee arthroplasty rates have increased substantially from 2012-2017, with the respective volumes of these procedures growing by 17.8% (55 981 hip replacements) and 15.5% (67 169 knee replacements).³⁷ Indications for operative treatments are demonstration of radiographic OA and experience of persistent pain for six months after failure of non-operative treatments.⁹⁸ TKA is not without risk or complications; adverse outcomes can occur, which may include: mortality, surgical site infection, and cardiovascular complications (myocardial infarction, congestive heart failure, arrhythmia, or pulmonary embolus).^{11, 68} Main risk factors for these negative outcomes are associated with a patient's medical history and age.¹¹

Despite long-term pain relief and patient satisfaction, many TKA patients continue to have impairments and functional limitations when compared with age-matched controls.^{26, 70} After unilateral TKA, patients tend to walk slower, have less peak knee flexion during gait, and have altered sagittal knee moments compared to controls.^{63, 65} An increased sagittal knee moment is a biomechanical indication of increased loading in the medial knee compartment, which is related to the severity of OA, and is the best predictor of OA progression.⁴ Furthermore, the contralateral knee is more likely to suffer OA disease progression more than the ipsilateral or contralateral hip or ankle.⁷⁹ Within 10 years of the original TKA, 40% of patients will undergo a second TKA on the contralateral knee.^{64, 79} Although TKA has revolutionized end-stage OA treatment, it remains an inadequate technique for approximately 19% of patients since they are unsatisfied with the outcomes related to pain relief and restoring function.¹⁵ Therefore, accurate knowledge of joint motion and loading during weight-bearing activities, such as walking, is integral for developing strategies for alleviating joint pain and restoring functionality.

1.2 Review of Current Methods for Knee Motion Analysis

1.2.1 3D Motion Capture Gait Analysis

Gait analysis is a robust technique used to assess dynamic musculoskeletal movement during functional activities and has numerous applications in orthopaedic investigations,

which include the evaluation of joint function following corrective surgery, comparison of different treatment options and therapies, and understanding the pathology of musculoskeletal disorders and trauma. This technique uses reflective skin-mounted external markers attached to specific landmarks on the subject, and high-speed cameras to track rigid body motion (**Figure 1.1**); however, it cannot provide quantitative information about joint micro-motion and its accuracy is hindered by soft-tissue artefacts. This phenomenon occurs because optical markers on the skin may not reflect the motion of the underlying bony structures.⁸⁰ Studies using gait analysis have demonstrated distinct gait patterns between healthy and OA patients,^{6, 63, 69} as well as differences between the non-operated and operated knee in the same patient.^{4, 26} One of the best methods to evaluate knee OA progression may be to perform measurements under dynamic loading in order to evaluate biomechanical function of the knee.⁶⁶ Overall, this modality provides excellent overall kinematic measurements, and with the addition of force plates, kinetic measurements within the lower extremities.



Figure 1.1: Gait real-time interactive analysis lab (GRAIL) located at the Wolf Orthopaedic Biomechanics Laboratory.

1.2.2 Radiography

Radiography is a non-invasive medical imaging modality that creates a single, static, two-dimensional (2D) radiographic image using ionizing radiation. X-rays are emitted from the source, attenuated by the region of interest, then the attenuated x-rays are absorbed by the detector to form the resultant x-ray image. The attenuation properties of tissues such as bone, air, and soft tissue have different atomic numbers, which results in a heterogenous distribution of intensities on the image due to the attenuation of x-ray photons.¹⁷ The amount of x-ray photon attenuation within a tissue is dependent on the linear attenuation coefficient (LAC), which depends on the absorption and scatter occurring per unit thickness of a tissue for a specific x-ray energy.¹⁷ In the current clinical setting, the Kellgren-Lawrence classification system uses weight-bearing radiographic images to grade the severity of knee OA based on osteophyte formation, joint space narrowing, and subchondral osteosclerosis.^{16, 44} The success of TKA is evaluated using weight-bearing antero-posterior and lateral radiographs, however the image quality can be influenced by patient positioning and orientation of the x-ray detector.⁷⁶ Although radiography is effective at demonstrating the progression of OA, it has some limitations that include: the superimposition of tissue due to a 3D object being represented as a 2D image, and the inability to distinguish between two tissues with similar densities.⁷⁴

1.2.3 Radiostereometric Analysis

Radiostereometric analysis (RSA) is the gold standard for three-dimensional (3D) migration measurements of orthopaedic implants. RSA uses static radiographic images to estimate relative skeletal motion between successive clinical examinations to measure migration and wear of orthopaedic implants in the ankle,^{18, 29} knee,^{75, 83-86} hip,^{33, 61} wrist,⁵⁹ elbow,^{23, 24} and shoulder joints.^{2, 32, 88} This technique has been applied to assess cervical⁹⁹ and lumbar spine fracture healing.⁸ RSA utilizes simultaneous bi-planar x-rays (**Figure 1.2**) to obtain accurate 3D measurements of joint micro-motion using marker-based methods or model-based RSA (MBRSA) techniques.⁷⁷ The marked-based method requires surgical implantation of at least three tantalum marker beads into each bone comprising the joint of interest, while MBRSA matches contours of virtual shadows to

the shape and location of digital models to obtain measurements of joint micro-motion.⁴⁰ Both techniques create a spatial model of the rigid object using stereoscopic x-ray sources that generates two projections from simultaneous radiographic exposures, however precision is lower with MBRSA.⁴⁵ The calibration cage shown in **Figure 1.3** is present during the acquisition stereoscopic radiographs to determine photogrammetric projection parameters of the two x-ray sources. Images of the tantalum beads are analyzed with model-based non-linear image analysis algorithms that determine the centroid of the marker to subpixel accuracy.¹⁴ Marker-based RSA is extremely dependent upon the ability to identify the same marker bead in both radiographs.⁴⁸ Reported accuracy for marker-based RSA at 95% significance level ranges between 0.05 and 0.5 mm for translations and between 0.15° and 1.15° for rotations.⁴⁷ In a separate study, MBRSA pose-estimation algorithms were optimized to improve accuracy of the method which proved to be comparable to conventional marker-based RSA.⁴⁶ Although this technique has many advantages, it is limited by a small field-of-view (FOV) resulting from the intersection between the two x-ray beams and it can only evaluate implanted markers with static images in a single joint.



Figure 1.2: Example of bi-planar setup in the radiostereometric analysis lab located at Robarts Research Institute.

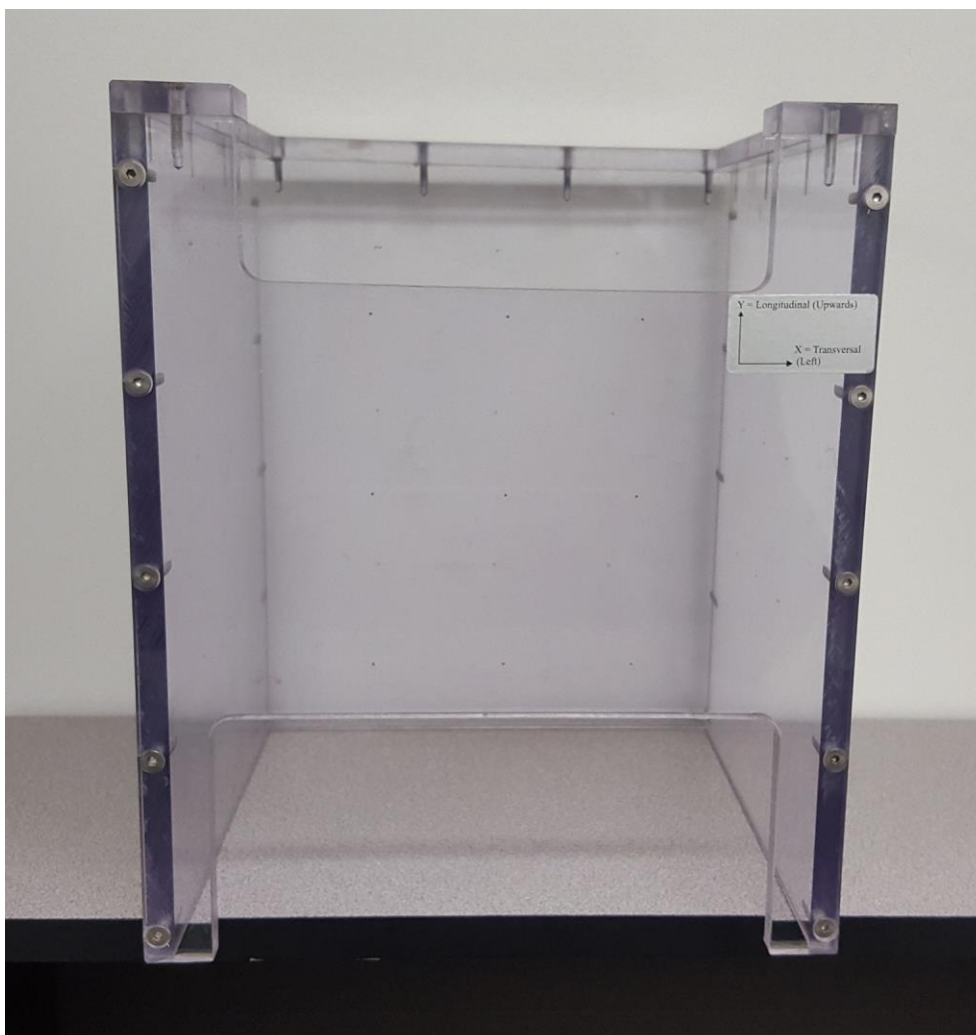


Figure 1.3: Radiostereometric analysis calibration cage for a bi-planar examination.

1.2.4 Fluoroscopy

Fluoroscopy is the continuous acquisition of multiple radiographic images to create a dynamic radiographic “movie” of a patient. Recently, fluoroscopic systems have been used as a gold standard method for the assessment of soft-tissue artefacts on motion analysis.^{3, 31, 52} Fluoroscopic images are critical for obtaining accurate knowledge of joint motion and loading during functional activities, facilitating the development of strategies for reducing joint pain and understanding the pathogenesis of OA.¹ The conventional RSA technique has been applied to high-speed dynamic acquisitions using a synchronized bi-planar fluoroscopy setup.⁸² Bi-planar fluoroscopic systems have reported

measurement errors of 0.094 mm for translations and 0.083° for rotations.⁴¹ A major constraint of implementation into routine clinical practice is caused by the need for highly specialized imaging equipment that may not be readily available in a hospital environment. Additionally, this technique has a small FOV that is restricted to the regions where the two x-ray beams intersect, therefore only one joint with implanted markers can be examined at a time. Single-plane x-ray fluoroscopy setups are more practical for clinical implementation since this approach requires less radiation, is less computationally intensive, utilizes equipment currently available in most hospitals, and allows for natural dynamic motion in a large FOV to evaluate dynamic 3D motions of the lower extremity.^{10, 22, 60, 92} Calibration of geometrical information pertaining to intrinsic and extrinsic camera parameters is required to determine the spatial position and orientation of the object. The position and orientation of the calibration object also defines the coordinate system where joint motion is reconstructed. Although in-plane translations (T_x and T_y) and rotation (R_z) can be accurately predicted from a single 2D view, precise measurement for out-of-plane rotations (R_x and R_y) and translation (T_z) are very difficult.^{30, 67, 92} Single-plane fluoroscopic setups using fluoroscopic shape matching have reported mean errors between 0.03-0.70 mm for translations and 0.03 - 0.12° for rotations.⁷⁸

Roentgen single-plane photogrammetric analysis (RSPA) was developed to aide in the analysis of real-time musculoskeletal movement using a single radiation source with an RSA approach.^{30, 43, 94} This technique requires *a priori* knowledge of the 3D geometry of the markers from conventional marker-based RSA in order to calculate joint motion. In knee movement simulations, the maximum difference between the original and simulated movement for rotations and translations were 0.27° and 0.9 mm.⁹⁴ An example of a single-plane fluoroscopy system for RSPA is shown in **Figure 1.4**.

Although single-plane fluoroscopic systems provide excellent evaluations of dynamic joint motion, it is significantly limited by the requirement to have a 3D model of the anatomy of interest in order to accurately characterize 3D joint motion. This highlights the need for rapid, low-dose peripheral computed tomography systems that provide

quantitative 3D image data to augment dynamic RSPA systems. This requirement for peripheral CT (including weight-bearing CT) provides the motivation for this thesis.



Figure 1.4: NRT Adora X-ray Fluoroscopy system pictured at the Wolf Orthopaedic Biomechanics Laboratory.

1.2.5 Computed Tomography

Computed tomography (CT) creates 3D cross-sectional images by scanning thin sections of the body with a narrow, fan-shaped x-ray beam that rotates around the body while it moves through the gantry. The averaged distributions of LACs within tissue are used to determine image contrast within each voxel.⁷⁴ Unlike radiography, CT is able to remove superimposition of tissue, and can differentiate between objects with small differences in LACs. CT numbers or Hounsfield units (HU) are used to quantify the differences in x-ray attenuation occurring in a voxel. Air and water were arbitrarily assigned the values of -1000 HU and 0 HU, respectively.⁷⁴ Clinical CT has been used previously to evaluate

knee-joint alignment, and patellar subluxation.^{42, 93} Recent studies with clinical CT scanners have simulated weight-bearing conditions by applying an axial load to a patient's legs during an image acquisition while in a supine position.^{12, 28, 71} Although CT provides high quality cross-sectional images with excellent contrast resolution, it is typically unable to acquire images in a natural weight-bearing stance, due to fundamental scanner design limitations.

1.2.6 Cone-beam Computed Tomography

Cone-beam computed tomography (CBCT) is based on the same principles as a conventional CT scanner, but designed for higher resolution imaging.⁹ CBCT uses a rotating flat-panel detector with a cone-shaped x-ray beam that does not require patient translation to acquire volumetric images. There are two possible scanner design configurations: 1) rotating object and 2) rotating gantry. The rotating gantry configuration is the most common configuration for commercial dedicated extremity CBCT scanners. This design mounts the tube and detector on a gantry that rotates around a central axis.⁹ Numerous 2D fluoroscopic projections are acquired over various angles around the area of interest to construct volumetric images. The differences in x-ray attenuation are determined by the object's electron density and physical density in each projection image. The reconstructed images are comprised of a 3D matrix of voxels with each voxel containing a CT number, which is proportional to the mean linear attenuation coefficient of the material within that voxel.⁹ Similar to conventional CT, the grey-level of each voxel in a CBCT image is measured with HU, which are directly scaled to the x-ray absorption characteristics of air and water (-1000 HU and 0 HU, respectively).⁹

Recent advances in CBCT have created scanner designs that utilize a motorized gantry to allow for weight-bearing imaging of the lower extremity in either a single or double leg stance.^{20, 57, 62, 95} These CBCT scanner designs allow for an increased distance from the torso, which lowers radiation dose because less scattered radiation can interact with radiosensitive organs within the torso.⁸⁷ Previous studies have demonstrated that extremity CBCT images produce an equal or smaller effective dose, while maintaining image quality comparable to conventional CT.^{13, 50, 51} The overall image quality in CBCT

is determined by the geometry and characteristics of the x-ray source and detector. The ideal detector has a large area with a consistent, linear, uniform response to all x-ray energies, and no geometric distortion.⁹ The image quality can be optimized by various scan parameters including: scan time, field of view, spatial resolution, temporal resolution, contrast resolution, and image dose.⁹ Image quality is typically evaluated using the spatial, contrast, and temporal resolution.⁷⁴ Spatial resolution is defined as the ability to differentiate between two small objects that are very close together.⁷⁴ Contrast resolution determines the ability to differentiate between objects with similar LACs.⁷⁴ Temporal resolution refers to the acquisition rate of the projections images that are used in image reconstruction.⁷⁴ An example of a commercially available CBCT scanner is shown in **Figure 1.5**.

In both CT and CBCT, imprecision of geometric calibration information may lead to loss of spatial resolution, double contours, or star artefacts.^{54, 81, 90} Most volumetric reconstruction algorithms assume the gantry rotation occurs in a perfect circular trajectory,²⁷ however there may be imperfections in the trajectory of the gantry's rotation. These imperfections may be either parallel to the axis of rotation or tangential to the circle of rotation and perpendicular to the line joining the x-ray source and detector.²⁵ Image-based geometric calibration can be incorporated into the reconstruction algorithm either concurrently or prospectively to characterize imperfections in gantry motion during rotation.²⁵ Geometric calibration of an imaging system determines various parameters, which can be divided into five intrinsic and six extrinsic geometric calibration parameters.⁵⁵ The intrinsic parameters describe the inherent properties of the x-ray system geometry that remain constant throughout operation; this includes pixel size, source-to-image distance, and detector offset.⁵³ The extrinsic parameters indicate the 3D rotational and translational matrices of the entire imaging system relative to the calibration object.⁵³ A minimum of six points of correspondence are required to calculate these eleven geometric calibration parameters.³⁵ CBCT is ideally suited for extremity musculoskeletal health applications since it can obtain true weight-bearing, 3D volumetric scans with optimal image quality at a low-dose when compared to conventional CT.



Figure 1.5: Planned Verity extremity cone-beam computed tomography scanner located at the Wolf Orthopaedic Biomechanics Laboratory.

1.3 Thesis Objectives and Hypotheses

The overall goal of this thesis is to develop a method to test various image quality parameters and to develop a multimodality CBCT system for investigations of musculoskeletal conditions. The specific objectives of the research were:

1. To test and optimize CT acquisitions for various image quality parameters that include: spatial resolution, geometric accuracy, signal linearity, image uniformity, and system noise;

2. To develop a method for producing accurate CBCT reconstructions from a ceiling-mounted single-plane x-ray fluoroscopy system using a custom 3D printed calibration object for geometric calibration and in-house software for image reconstruction.

1.4 Thesis Organization

Chapter two describes the methodology for the primary goal of testing and optimizing CT acquisitions for basic imaging parameters that were quantified using phantoms mimicking diameters of the upper and lower extremity. Chapter three describes the acquisition of CBCT image volumes using a ceiling-mounted single-plane x-ray fluoroscopy system. Finally, the thesis is concluded in Chapter four with a summary of the major results of these projects and a discussion of potential areas for future work.

1.5 References

1. Ackland, D. C., Keynejad, F., & Pandy, M. G. (2011). Future trends in the use of X-ray fluoroscopy for the measurement and modelling of joint motion. *Proc Inst Mech Eng H*, 225(12), 1136-1148.
2. Akbari-Shandiz, M., Mozingo, J. D., Holmes, D. R., & Zhao, K. D. (2017). Three-Dimensional Glenohumeral Joint Kinematic Analyses from Asynchronous Biplane Fluoroscopy Using an Interpolation Technique. In A. Wittek, G. Joldes, P. M. F. Nielsen, B. J. Doyle, & K. Miller (Eds.), *Computational Biomechanics for Medicine* (pp. 101-110). Cham: Springer International Publishing.
3. Akbarshahi, M., Schache, A. G., Fernandez, J. W., Baker, R., Banks, S., & Pandy, M. G. (2010). Non-invasive assessment of soft-tissue artifact and its effect on knee joint kinematics during functional activity. *Journal of biomechanics*, 43(7), 1292-1301.
4. Alnahdi, A. H., Zeni, J. A., & Snyder-Mackler, L. (2011). Gait after unilateral total knee arthroplasty: frontal plane analysis. *Journal of orthopaedic research : official publication of the Orthopaedic Research Society*, 29(5), 647-652.
5. Andriacchi, T. P., & Mundermann, A. (2006). The role of ambulatory mechanics in the initiation and progression of knee osteoarthritis. *Current opinion in rheumatology*, 18(5), 514-518.

6. Andriacchi, T. P., Mundermann, A., Smith, R. L., Alexander, E. J., Dyrby, C. O., & Koo, S. (2004). A framework for the in vivo pathomechanics of osteoarthritis at the knee. *Annals of Biomedical Engineering*, 32(3), 447-457.
7. Astephen, J. L., Deluzio, K. J., Caldwell, G. E., Dunbar, M. J., & Hubley-Kozey, C. L. (2008). Gait and neuromuscular pattern changes are associated with differences in knee osteoarthritis severity levels. *Journal of biomechanics*, 41(4), 868-876.
8. Axelsson, P., & Karlsson, B. S. (2005). Standardized provocation of lumbar spine mobility: three methods compared by radiostereometric analysis. *Spine*, 30(7), 792-797.
9. Badea, C. T., Drangova, M., Holdsworth, D. W., & Johnson, G. A. (2008). In vivo small-animal imaging using micro-CT and digital subtraction angiography. *Phys Med Biol*, 53(19), R319-350.
10. Banks, S. A., & Hodge, W. A. (1996). Accurate measurement of three-dimensional knee replacement kinematics using single-plane fluoroscopy. *IEEE Trans Biomed Eng*, 43(6), 638-649.
11. Basilico, F. C., Sweeney, G., Losina, E., Gaydos, J., Skoniecki, D., Wright, E. A., & Katz, J. N. (2008). Risk factors for cardiovascular complications following total joint replacement surgery. *Arthritis Rheum*, 58(7), 1915-1920.
12. Biedert, R. M., & Gruhl, C. (1997). Axial computed tomography of the patellofemoral joint with and without quadriceps contraction. *Archives of Orthopaedic and Trauma Surgery*, 116(1-2), 77-82.
13. Biswas, D., Bible, J. E., Bohan, M., Simpson, A. K., Whang, P. G., & Grauer, J. N. (2009). Radiation exposure from musculoskeletal computerized tomographic scans. *J Bone Joint Surg Am*, 91(8), 1882-1889.
14. Börlin, N. (2000). *Model-based measurements in digital radiographs*: Univ.
15. Bourne, R. B., Chesworth, B. M., Davis, A. M., Mahomed, N. N., & Charron, K. D. (2010). Patient satisfaction after total knee arthroplasty: who is satisfied and who is not? *Clin Orthop Relat Res*, 468(1), 57-63.
16. Brandt, K. D., Fife, R. S., Braunstein, E. M., & Katz, B. (2010). Radiographic grading of the severity of knee osteoarthritis: Relation of the Kellgren and Lawrence grade to a grade based on joint space narrowing, and correlation with arthroscopic evidence of articular cartilage degeneration. *Arthritis & Rheumatism*, 34(11), 1381-1386.
17. Bushberg, J. T., & Boone, J. M. (2002). *The essential physics of medical imaging*: Lippincott Williams & Wilkins.

18. Carlsson, A., Markusson, P., & Sundberg, M. (2005). Radiostereometric analysis of the double-coated STAR total ankle prosthesis: a 3-5 year follow-up of 5 cases with rheumatoid arthritis and 5 cases with osteoarthritis. *Acta orthopaedica*, 76(4), 573-579.
19. Carr, A. J., Robertsson, O., Graves, S., Price, A. J., Arden, N. K., Judge, A., & Beard, D. J. (2012). Knee replacement. *Lancet*, 379(9823), 1331-1340.
20. Carrino, J. A., Al Muhit, A., Zbijewski, W., Thawait, G. K., Stayman, J. W., Packard, N., . . . Siewerdsen, J. H. (2014). Dedicated cone-beam CT system for extremity imaging. *Radiology*, 270(3), 816-824.
21. Das, S. K., & Farooqi, A. (2008). Osteoarthritis. *Best Pract Res Clin Rheumatol*, 22(4), 657-675.
22. Dennis, D. A., Mahfouz, M. R., Komistek, R. D., & Hoff, W. (2005). In vivo determination of normal and anterior cruciate ligament-deficient knee kinematics. *Journal of biomechanics*, 38(2), 241-253.
23. Ericson, A., Arndt, A., Stark, A., Noz, M. E., Maguire, G. Q., Jr., Zeleznik, M. P., & Olivecrona, H. (2007). Fusion of radiostereometric analysis data into computed tomography space: application to the elbow joint. *Journal of biomechanics*, 40(2), 296-304.
24. Ericson, A., Olivecrona, H., Stark, A., Noz, M. E., Maguire, G. Q., Zeleznik, M. P., & Arndt, A. (2010). Computed tomography analysis of radiostereometric data to determine flexion axes after total joint replacement: application to the elbow joint. *Journal of biomechanics*, 43(10), 1947-1952.
25. Fahrig, R., & Holdsworth, D. W. (2000). Three-dimensional computed tomographic reconstruction using a C-arm mounted XRII: image-based correction of gantry motion nonidealities. *Med Phys*, 27(1), 30-38.
26. Farquhar, S., & Snyder-Mackler, L. (2010). The Chitranjan Ranawat Award: The nonoperated knee predicts function 3 years after unilateral total knee arthroplasty. *Clin Orthop Relat Res*, 468(1), 37-44.
27. Feldkamp, L. A., Davis, L. C., & Kress, J. W. (1984). Practical Cone-Beam Algorithm. *J Opt Soc Am A*, 1(6), 612-619.
28. Ferri, M., Scharfenberger, A. V., Goplen, G., Daniels, T. R., & Pearce, D. (2008). Weightbearing CT scan of severe flexible pes planus deformities. *Foot Ankle Int*, 29(2), 199-204.
29. Fong, J. W., Veljkovic, A., Dunbar, M. J., Wilson, D. A., Hennigar, A. W., & Glazebrook, M. A. (2011). Validation and precision of model-based radiostereometric analysis (MBRSA) for total ankle arthroplasty. *Foot Ankle Int*, 32(12), 1155-1163.

30. Garling, E. H., Kaptein, B. L., Geleijns, K., Nelissen, R. G., & Valstar, E. R. (2005). Marker Configuration Model-Based Roentgen Fluoroscopic Analysis. *Journal of biomechanics*, 38(4), 893-901.
31. Garling, E. H., Kaptein, B. L., Mertens, B., Barendregt, W., Veeger, H. E., Nelissen, R. G., & Valstar, E. R. (2007). Soft-tissue artefact assessment during step-up using fluoroscopy and skin-mounted markers. *Journal of biomechanics*, 40 Suppl 1, S18-24.
32. Gobezie, R., Lavery, K. P., Bragdon, C., Higgins, L. D., Malchau, H., & Warner, J. J. P. (2006). Radiostereometric analysis of the anatomical total shoulder arthroplasty and reverse total shoulder replacement: an analysis of component stability and polyethylene wear. *The Orthopaedic Journal at Harvard Medical School*, 110-112.
33. Goyal, P., Howard, J. L., Yuan, X., Teeter, M. G., & Lanting, B. A. (2017). Effect of Acetabular Position on Polyethylene Liner Wear Measured Using Simultaneous Biplanar Acquisition. *The Journal of arthroplasty*, 32(5), 1670-1674.
34. Haq, I., Murphy, E., & Dacre, J. (2003). Osteoarthritis. *Postgrad Med J*, 79(933), 377-383.
35. Hartley, R., & Zisserman, A. (2004). *Multiple view geometry in computer vision*. Cambridge: Cambridge University Press.
36. Hayes, D. A., Miller, L. E., & Block, J. E. (2012). Knee Osteoarthritis Treatment with the KineSpring Knee Implant System: A Report of Two Cases. *Case Rep Orthop*, 2012, 297326.
37. Hip and Knee Replacements in Canada, 2016–2017: Canadian Joint Replacement Registry Annual Report. 51.
38. Hip and Knee Replacements in Canada: Canadian Joint Replacement Registry 2015 Annual Report. 63.
39. Hunter, D. J. (2011). Osteoarthritis. *Best Pract Res Clin Rheumatol*, 25(6), 801-814.
40. Hurschler, C., Seehaus, F., Emmerich, J., Kaptein, B. L., & Windhagen, H. (2009). Comparison of the model-based and marker-based roentgen stereophotogrammetry methods in a typical clinical setting. *The Journal of arthroplasty*, 24(4), 594-606.
41. Iaquinto, J. M., Tsai, R., Haynor, D. R., Fassbind, M. J., Sangeorzan, B. J., & Ledoux, W. R. (2014). Marker-based validation of a biplane fluoroscopy system for quantifying foot kinematics. *Medical engineering & physics*, 36(3), 391-396.

42. Inoue, M., Shino, K., Hirose, H., Horibe, S., & Ono, K. (1988). Subluxation of the patella. Computed tomography analysis of patellofemoral congruence. *J Bone Joint Surg Am*, 70(9), 1331-1337.
43. Ioppolo, J., Borlin, N., Bragdon, C., Li, M., Price, R., Wood, D., . . . Nivbrant, B. (2007). Validation of a low-dose hybrid RSA and fluoroscopy technique: Determination of accuracy, bias and precision. *Journal of biomechanics*, 40(3), 686-692.
44. Kan, H., Arai, Y., Kobayashi, M., Nakagawa, S., Inoue, H., Hino, M., . . . Kubo, T. (2017). Fixed-flexion view X-ray of the knee superior in detection and follow-up of knee osteoarthritis. *Medicine (Baltimore)*, 96(49), e9126.
45. Kaptein, B. L., Valstar, E. R., Spoor, C. W., Stoel, B. C., & Rozing, P. M. (2006). Model-based RSA of a femoral hip stem using surface and geometrical shape models. *Clin Orthop Relat Res*, 448, 92-97.
46. Kaptein, B. L., Valstar, E. R., Stoel, B. C., Rozing, P. M., & Reiber, J. H. (2004). Evaluation of three pose estimation algorithms for model-based roentgen stereophotogrammetric analysis. *Proc Inst Mech Eng H*, 218(4), 231-238.
47. Karrholm, J. (1989). Roentgen stereophotogrammetry. Review of orthopedic applications. *Acta Orthop Scand*, 60(4), 491-503.
48. Karrholm, J., Herberts, P., Hultmark, P., Malchau, H., Nivbrant, B., & Thanner, J. (1997). Radiostereometry of hip prostheses. Review of methodology and clinical results. *Clin Orthop Relat Res*(344), 94-110.
49. Kaufman, K. R., Hughes, C., Morrey, B. F., Morrey, M., & An, K. N. (2001). Gait characteristics of patients with knee osteoarthritis. *Journal of biomechanics*, 34(7), 907-915.
50. Koivisto, J., Kiljunen, T., Kadesjo, N., Shi, X. Q., & Wolff, J. (2015). Effective radiation dose of a MSCT, two CBCT and one conventional radiography device in the ankle region. *J Foot Ankle Res*, 8(1), 8.
51. Koivisto, J., Kiljunen, T., Wolff, J., & Kortensniemi, M. (2013). Assessment of effective radiation dose of an extremity CBCT, MSCT and conventional X ray for knee area using MOSFET dosimeters. *Radiat Prot Dosimetry*, 157(4), 515-524.
52. Kuo, M. Y., Tsai, T. Y., Lin, C. C., Lu, T. W., Hsu, H. C., & Shen, W. C. (2011). Influence of soft tissue artifacts on the calculated kinematics and kinetics of total knee replacements during sit-to-stand. *Gait Posture*, 33(3), 379-384.
53. Kyriakopoulos, K. J., Yiannakos, P., Kallipolites, V., & Domales, K. (1999). A geometric calibration methodology for single-head cone-beam X-ray systems. *J Intell Robot Syst*, 24(2), 151-174.

54. Kyriakou, Y., Lapp, R. M., Hillebrand, L., Ertel, D., & Kalender, W. A. (2008). Simultaneous misalignment correction for approximate circular cone-beam computed tomography. *Phys Med Biol*, *53*(22), 6267-6289.
55. Li, X., Da, Z., & Liu, B. (2010). A generic geometric calibration method for tomographic imaging systems with flat-panel detectors--a detailed implementation guide. *Med Phys*, *37*(7), 3844-3854.
56. Loughhead, J. M., Malhan, K., Mitchell, S. Y., Pinder, I. M., McCaskie, A. W., Deehan, D. J., & Lingard, E. A. (2008). Outcome following knee arthroplasty beyond 15 years. *Knee*, *15*(2), 85-90.
57. Ludlow, J. B., & Ivanovic, M. (2014). Weightbearing CBCT, MDCT, and 2D imaging dosimetry of the foot and ankle. *International Journal of Diagnostic Imaging*, *1*(2), 1.
58. Lutzner, J., Kasten, P., Gunther, K. P., & Kirschner, S. (2009). Surgical options for patients with osteoarthritis of the knee. *Nat Rev Rheumatol*, *5*(6), 309-316.
59. Madanat, R., Moritz, N., & Aro, H. T. (2007). Three-dimensional computer simulation of radiostereometric analysis (RSA) in distal radius fractures. *Journal of biomechanics*, *40*(8), 1855-1861.
60. Mahfouz, M. R., Hoff, W. A., Komistek, R. D., & Dennis, D. A. (2003). A robust method for registration of three-dimensional knee implant models to two-dimensional fluoroscopy images. *IEEE Trans Med Imaging*, *22*(12), 1561-1574.
61. Malchau, H., Karrholm, J., Wang, Y. X., & Herberts, P. (1995). Accuracy of migration analysis in hip arthroplasty. Digitized and conventional radiography, compared to radiostereometry in 51 patients. *Acta Orthop Scand*, *66*(5), 418-424.
62. Marzo, J., Kluczynski, M., Notino, A., & Bisson, L. (2016). Comparison of a Novel Weightbearing Cone Beam Computed Tomography Scanner Versus a Conventional Computed Tomography Scanner for Measuring Patellar Instability. *Orthop J Sports Med*, *4*(12), 2325967116673560.
63. McClelland, J. A., Webster, K. E., & Feller, J. A. (2007). Gait analysis of patients following total knee replacement: a systematic review. *Knee*, *14*(4), 253-263.
64. McMahan, M., & Block, J. A. (2003). The risk of contralateral total knee arthroplasty after knee replacement for osteoarthritis. *J Rheumatol*, *30*(8), 1822-1824.
65. Milner, C. E. (2009). Is gait normal after total knee arthroplasty? Systematic review of the literature. *J Orthop Sci*, *14*(1), 114-120.
66. Miyazaki, T., Wada, M., Kawahara, H., Sato, M., Baba, H., & Shimada, S. (2002). Dynamic load at baseline can predict radiographic disease progression in

- medial compartment knee osteoarthritis. *Annals of the Rheumatic Diseases*, 61(7), 617-622.
67. Muhit, A. A., Pickering, M. R., Scarvell, J. M., Ward, T., & Smith, P. N. (2013). Image-assisted non-invasive and dynamic biomechanical analysis of human joints. *Phys Med Biol*, 58(13), 4679-4702.
 68. Mulcahy, H., & Chew, F. S. (2014). Current concepts in knee replacement: complications. *AJR Am J Roentgenol*, 202(1), W76-86.
 69. Mundermann, A., Dyrby, C. O., & Andriacchi, T. P. (2005). Secondary gait changes in patients with medial compartment knee osteoarthritis: increased load at the ankle, knee, and hip during walking. *Arthritis Rheum*, 52(9), 2835-2844.
 70. Noble, P. C., Gordon, M. J., Weiss, J. M., Reddix, R. N., Conditt, M. A., & Mathis, K. B. (2005). Does Total Knee Replacement Restore Normal Knee Function? *Clinical Orthopaedics and Related Research*, &NA;(431), 157-165.
 71. Oswald, M. H., Jakob, R. P., Schneider, E., & Hoogewoud, H. M. (1993). Radiological analysis of normal axial alignment of femur and tibia in view of total knee arthroplasty. *The Journal of arthroplasty*, 8(4), 419-426.
 72. Peat, G., McCarney, R., & Croft, P. (2001). Knee pain and osteoarthritis in older adults: a review of community burden and current use of primary health care. *Annals of the Rheumatic Diseases*, 60(2), 91-97.
 73. Rankin, E. A., Alarcon, G. S., Chang, R. W., Cooney, L. M., Costley, L. S., Delitto, A., . . . Marciel, C. (2004). NIH consensus statement on total knee replacement December 8-10, 2003. *Journal of Bone and Joint Surgery-American Volume*, 86a(6), 1328-1335.
 74. Romans, L. E. (2010). *Computed Tomography for Technologists: A Comprehensive Text*: Lippincott Williams & Wilkins.
 75. Saari, T., Carlsson, L., Karlsson, J., & Karrholm, J. (2005). Knee kinematics in medial arthrosis. Dynamic radiostereometry during active extension and weight-bearing. *Journal of biomechanics*, 38(2), 285-292.
 76. Sarmah, S. S., Patel, S., Hossain, F. S., & Haddad, F. S. (2012). The radiological assessment of total and unicompartmental knee replacements. *J Bone Joint Surg Br*, 94(10), 1321-1329.
 77. Selvik, G. (1990). Roentgen stereophotogrammetric analysis. *Acta Radiol*, 31(2), 113-126.
 78. Seslija, P., Teeter, M. G., Yuan, X., Naudie, D. D., Bourne, R. B., Macdonald, S. J., . . . Holdsworth, D. W. (2012). Measurement of joint kinematics using a

- conventional clinical single-perspective flat-panel radiography system. *Med Phys*, 39(10), 6090-6103.
79. Shakoor, N., Block, J. A., Shott, S., & Case, J. P. (2002). Nonrandom evolution of end-stage osteoarthritis of the lower limbs. *Arthritis Rheum*, 46(12), 3185-3189.
 80. Stagni, R., Fantozzi, S., Cappello, A., & Leardini, A. (2005). Quantification of soft tissue artefact in motion analysis by combining 3D fluoroscopy and stereophotogrammetry: a study on two subjects. *Clinical biomechanics*, 20(3), 320-329.
 81. Strobel, N. K., Heigl, B., Brunner, T. M., Schuetz, O., Mitschke, M. M., Wiesent, K., & Mertelmeier, T. (2003, 2003/06/09/). *Improving 3D image quality of x-ray C-arm imaging systems by using properly designed pose determination systems for calibrating the projection geometry*. Paper presented at the Medical Imaging 2003.
 82. Tashman, S., & Anderst, W. (2003). In-vivo measurement of dynamic joint motion using high speed biplane radiography and CT: Application to canine ACL deficiency. *J Biomech Eng-T Asme*, 125(2), 238-245.
 83. Teeter, M. G. (2012). Assessment of Wear in Total Knee Arthroplasty Using Advanced Radiographic Techniques. 202.
 84. Teeter, M. G., Leitch, K. M., Pape, D., Yuan, X., Birmingham, T. B., & Giffin, J. R. (2015). Radiostereometric analysis of early anatomical changes following medial opening wedge high tibial osteotomy. *Knee*, 22(1), 41-46.
 85. Teeter, M. G., Perry, K. I., Yuan, X., Howard, J. L., & Lanting, B. A. (2017). Contact Kinematic Differences Between Gap Balanced vs Measured Resection Techniques for Single Radius Posterior-Stabilized Total Knee Arthroplasty. *The Journal of arthroplasty*, 32(6), 1834-1838.
 86. Teeter, M. G., Perry, K. I., Yuan, X., Howard, J. L., & Lanting, B. A. (2018). Contact Kinematics Correlates to Tibial Component Migration Following Single Radius Posterior Stabilized Knee Replacement. *The Journal of arthroplasty*, 33(3), 740-745.
 87. Tuominen, E. K., Kankare, J., Koskinen, S. K., & Mattila, K. T. (2013). Weight-bearing CT imaging of the lower extremity. *AJR Am J Roentgenol*, 200(1), 146-148.
 88. Van de Kleut, M. L., Yuan, X., Athwal, G. S., & Teeter, M. G. (2018). Validation of radiostereometric analysis in six degrees of freedom for use with reverse total shoulder arthroplasty. *Journal of biomechanics*, 68, 126-131.

89. Van Manen, M. D., Nace, J., & Mont, M. A. (2012). Management of primary knee osteoarthritis and indications for total knee arthroplasty for general practitioners. *J Am Osteopath Assoc*, *112*(11), 709-715.
90. von Smekal, L., Kachelriess, M., Stepina, E., & Kalender, W. A. (2004). Geometric misalignment and calibration in cone-beam tomography. *Med Phys*, *31*(12), 3242-3266.
91. Walker-Bone, K., Javaid, K., Arden, N., & Cooper, C. (2000). Regular review: medical management of osteoarthritis. *BMJ*, *321*(7266), 936-940.
92. Yamazaki, T., Watanabe, T., Nakajima, Y., Sugamoto, K., Tomita, T., Yoshikawa, H., & Tamura, S. (2004). Improvement of depth position in 2-D/3-D registration of knee implants using single-plane fluoroscopy. *Ieee Transactions on Medical Imaging*, *23*(5), 602-612.
93. Yoshino, N., Takai, S., Ohtsuki, Y., & Hirasawa, Y. (2001). Computed tomography measurement of the surgical and clinical transepicondylar axis of the distal femur in osteoarthritic knees. *The Journal of arthroplasty*, *16*(4), 493-497.
94. Yuan, X., Ryd, L., Tanner, K. E., & Lidgren, L. (2002). Roentgen single-plane photogrammetric analysis (RSPA.) A new approach to the study of musculoskeletal movement. *J Bone Joint Surg Br*, *84*(6), 908-914.
95. Zbijewski, W., De Jean, P., Prakash, P., Ding, Y., Stayman, J. W., Packard, N., . . . Siewerdsen, J. H. (2011). A dedicated cone-beam CT system for musculoskeletal extremities imaging: design, optimization, and initial performance characterization. *Med Phys*, *38*(8), 4700-4713.
96. Zeni, J. A., Jr., Axe, M. J., & Snyder-Mackler, L. (2010). Clinical predictors of elective total joint replacement in persons with end-stage knee osteoarthritis. *BMC musculoskeletal disorders*, *11*(1), 86.
97. Zhang, W., Moskowitz, R. W., Nuki, G., Abramson, S., Altman, R. D., Arden, N., . . . Tugwell, P. (2007). OARSI recommendations for the management of hip and knee osteoarthritis, part I: critical appraisal of existing treatment guidelines and systematic review of current research evidence. *Osteoarthritis and cartilage*, *15*(9), 981-1000.
98. Zhang, W., Moskowitz, R. W., Nuki, G., Abramson, S., Altman, R. D., Arden, N., . . . Tugwell, P. (2008). OARSI recommendations for the management of hip and knee osteoarthritis, Part II: OARSI evidence-based, expert consensus guidelines. *Osteoarthritis and cartilage*, *16*(2), 137-162.
99. Zoëga, B., Kärrholm, J., & Lind, B. (1998). Plate fixation adds stability to two-level anterior fusion in the cervical spine: a randomized study using radiostereometry. *European Spine Journal*, *7*(4), 302-307.

Chapter 2

2 Quantitative Performance Evaluation of a Peripheral Cone-Beam Computed Tomography Scanner with Weight-bearing Capabilities

2.1 Introduction

Weight-bearing radiographs provide functional information about joint biomechanics of the foot, ankle, and knee.^{27-29, 48, 56} Due to their two-dimensional nature, the appearance of the joint is heavily dependent on positioning and the angle of joint flexion.²⁵ In cases where patients have severe deformities, two-dimensional images may not be conclusive and additional 3D views are required for a more sophisticated evaluation of osseous structures.¹² Routine volumetric imaging, such as computed tomography (CT) or magnetic resonance imaging (MRI), does not allow for weight-bearing imaging to be performed in a clinical healthcare setting. Recent studies, using these conventional modalities, have simulated weight-bearing conditions by applying an axial load to a subject's leg while in a supine position.^{20, 43, 52} However, these studies do not represent the physiological stresses of the joints in a normal weight-bearing stance, and the setup is impractical for routine clinical exams.

Recent advances in cone-beam computed tomography (CBCT) have resulted in scanners that utilize a motorized gantry, with a wide range of movements that includes horizontal tilting and lowering the gantry to the floor. These movements allow for weight-bearing images while a subject is in a single-leg stance inside the CBCT gantry, in addition to supine scans. Although there are numerous studies using peripheral CBCT scanners to compare image quality to conventional CT^{6, 26, 42, 49} and quantify effective dose,³³⁻³⁵ there are no studies to verify the basic imaging parameters required for accurate and precise measurements involving evaluations of weight-bearing joint alignment,^{27-29, 39} fracture detection,^{23, 40} arthrography,^{36, 37, 47} and arthritic disease progression in the upper and lower extremities.^{3, 38, 39}

While the Planmed Verity peripheral CBCT scanner has been available for a few years, its performance has not been validated using image quality phantoms that represent anatomy that would be encountered in future clinical studies. The manufacturer currently provides image quality phantoms with diameters resembling an average-sized elbow, however these results have not been validated using an image quality phantom simulating the diameter of an average-sized knee. The purpose of this study was to independently evaluate performance results of various reconstruction algorithms in a peripheral CBCT scanner using two image quality phantoms with diameters similar to the average-sized elbow and knee. Specific imaging parameters, such as spatial resolution, linearity, uniformity, noise, geometric accuracy, and effective dose, are measured and reported.

2.2 Methods

2.2.1 Extremity CT Scanner

The performance of a commercially available peripheral CBCT scanner (Verity CT scanner, Planmed Oy, Helsinki, Finland) was evaluated. The scanner uses an x-ray tube (D-067SB-P, Toshiba) with a 0.6 mm focal spot impinging on a tungsten target to produce pulsed x-ray radiation. The x-ray tube is capable of voltages ranging from 80-96 peak kilovolts (kVp) and output tube currents of 1-12 milliamperes (mA). The detector is a 20 x 25 cm amorphous silicon, flat-panel detector with 127 μm pixel spacing; it can be used in a 2 x 2 or 4 x 4 binning mode configuration, resulting in 254 μm or 508 μm effective pixel size, respectively. CBCT images have the option to be acquired with 300 to 600 projection images, resulting in scan times varying from 20 - 40 seconds over 210 degrees for three modes: low-dose, standard, and high resolution. The use of pulsed x-rays (i.e. exposures durations of 20 ms per view) limits the total radiation exposure time from 6 to 12 seconds, depending on the number of image projection frames acquired. 3D image volumes (13 cm length, 16 cm diameter) are reconstructed from x-ray projections using Verity Manager software (Planmed Oy, Helsinki, Finland), resulting in isotropic voxel spacing of 0.4 mm for the low-dose and standard modes, and 0.2 mm for the high-resolution scan mode. High-resolution and standard scans only differ with respect to the resolution. The low-dose mode differs mainly in a reduction of 6-24 mAs in comparison to the equivalent standard modes, depending on the body part selected. The CBCT

scanner can acquire images in conventional scan mode (**Figure 2.1a**) and a weight-bearing mode (**Figure 2.1b**). Additionally, the CT scanner is portable and can be powered from a standard electrical outlet.

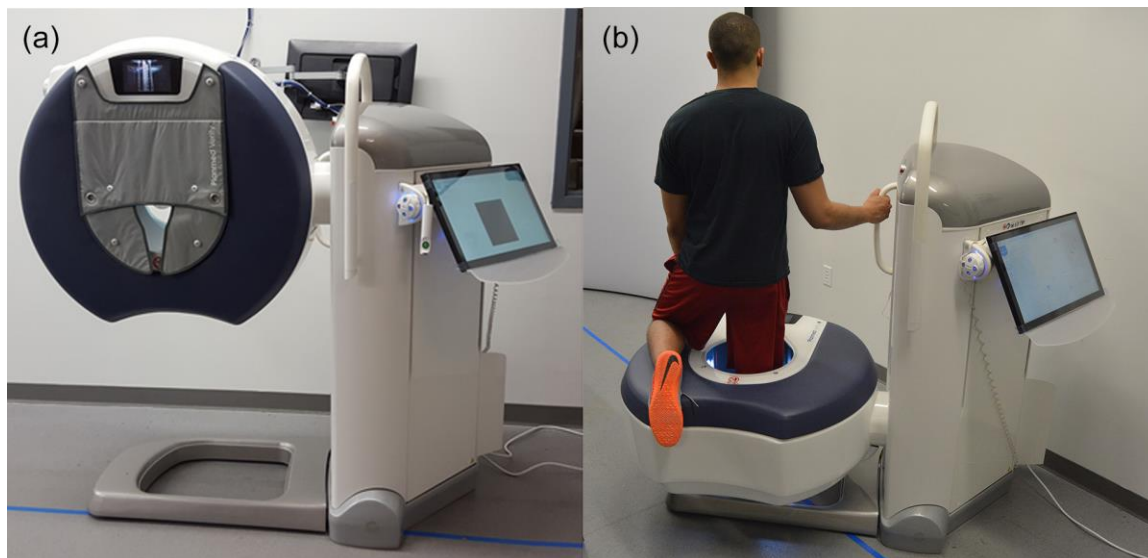


Figure 2.1: Peripheral cone-beam CT scanner pictured in conventional scan (a) mode and weight-bearing scan (b) mode.

2.2.2 Image quality phantoms and data acquisition

Performance of the Planned Verity CBCT scanner was evaluated using two image quality assessment phantoms. A large, custom-designed phantom and small phantom (MCTP 610, Simutec, London, ON) were used, each consisting of modular acrylic plates designed to test individual imaging parameters (**Figure 2.2**).^{15, 46} The diameter of the large (150 mm) and small (80 mm) phantoms used in this study were representative of the average diameter of a knee and elbow, respectively. The phantoms allow aspects of image quality to be analyzed, including: spatial resolution linearity, uniformity, noise, and geometric accuracy. These parameters were evaluated with the installed clinical reconstruction engine, a beta-reconstruction engine, and an Adaptive Image Noise Optimization (AINO) algorithm. The beta reconstruction engine allows for retrospective beam-hardening and patient-motion corrections for reconstructed image volumes. The AINO algorithm can be used retroactively to reduce noise throughout a reconstructed image volume. All image volumes were acquired using both 300 and 450 projection

protocols, which have 6 and 9 second exposures, respectively. Afterwards, image volumes are reconstructed at 0.2 mm isotropic resolution using both current and beta reconstruction algorithms, then processed using the AINO algorithm. For the large image quality phantom, six image volumes were produced per image dataset using the current reconstruction algorithm, beta reconstruction algorithm, and a beam-hardening correction (from beta reconstruction algorithm).

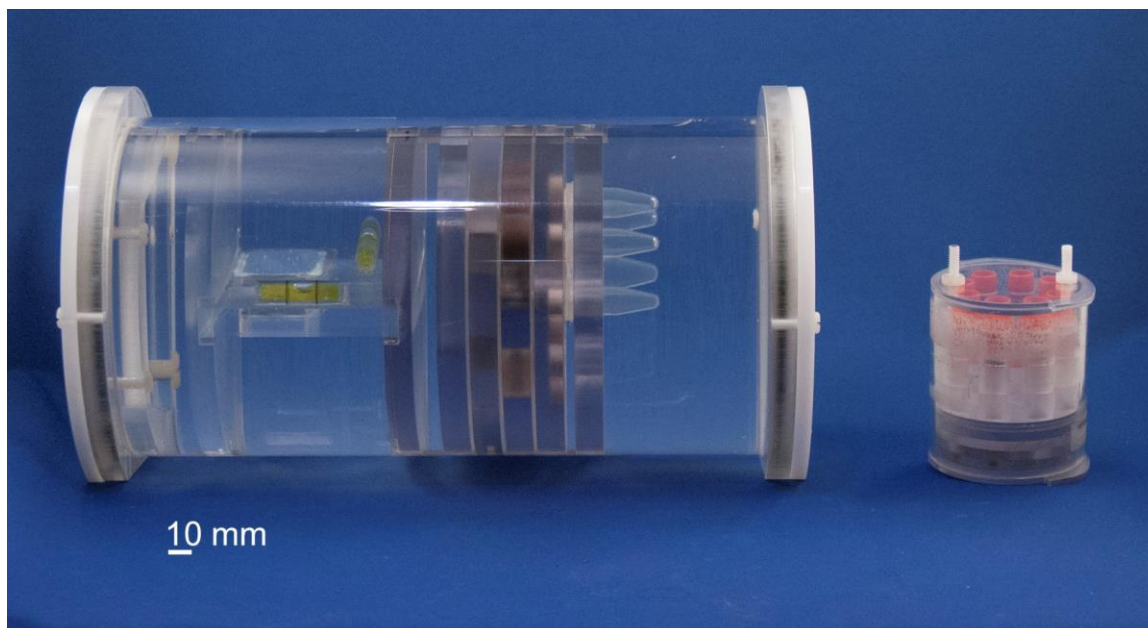


Figure 2.2: Large custom-built phantom (left) and small phantom (right) designed to evaluate the performance of cone-beam CT scanners.

Phantoms were placed within the CBCT scanner gantry and precisely levelled using internal or external bubble levels, for the large and small phantoms, respectively. For image quality scans using the large phantom, repeat acquisitions were acquired ($n = 10$) using the knee protocol (96 kVp). Repeat acquisitions ($n = 10$) of the small phantom were acquired using the scanner's elbow protocol (90 kVp). Excluding the linearity test, tube current settings (mA) were set to the manufacturer's prescribed protocol for the following image quality tests: spatial resolution, uniformity, noise, and geometric accuracy (**Table 2.1**). The systemic image noise was analyzed with tube current varying from 1 to 12 mA, which corresponds to exposures ranging from 6 mAs to 108 mAs ($n = 12$). Due to axial field-of-view limitations, the large phantom was scanned in two

sections and aligned orthogonal to the axis of rotation. The resultant reconstructed 3D volumes were scaled in Hounsfield units (HU). Image analysis was performed using MicroView image analysis software (Version 2.5.0-3851, Parallax Innovations, London ON), and custom processing software to calculate spatial resolution with a slanted-edge image.¹⁵

Table 2.1: Manufacturer’s clinical imaging standards for spatial resolution, linearity, uniformity, noise, and geometric accuracy.

Test Name	Spatial Resolution	Uniformity	Noise	Geometric Accuracy
Performance Criteria	MTF10> 1.25 lp/mm	Deviation< 50 HU	Standard Deviation <100 HU	±5% of indicated distance
Tube Current (mA)	4 mA	9 mA	1-12 mA	9 mA

2.2.3 Spatial Resolution

Both image quality phantoms utilized 5° slanted-edge images to evaluate the resolution of the CBCT scanner with custom software based on previously described methods.^{15, 46} Ten reconstructed axial slices of the slanted-edge image were averaged to reduce noise in the analyzed image. The averaged slanted-edge image was used to obtain an oversampled edge response function, which was subsequently differentiated into the line-spread function, and then Fourier transformed to generate the system’s modulation transfer function (MTF). Limiting spatial resolution was defined as the point where spatial frequency reaches 10% (referred to as MTF10). The small phantom can evaluate spatial resolution only in the slice (z) direction using a slanted-edge image. Additionally, the small phantom evaluated spatial resolution using four resolution coils (created from alternating sheets of aluminum and Mylar sheets corresponding to 1.0, 1.67, 2.5, and 3.3 lp/mm); however, two of these resolution coils were below the resolution limit of the CBCT system. The large phantom contains two orthogonal plates where the slanted-edge images can be acquired to evaluate the transverse (x-y) and axial (z) direction MTFs. Similarly, the large phantom evaluated spatial resolution using bar patterns (created from alternating sheets of aluminum and Mylar sheets with spacing varying from 0.4 to 2.0 lp/mm). Resolution coils and bar patterns provided a qualitative analysis and a

quantitative estimate of the MTF. As previously demonstrated by Droege,¹⁴ the MTF was calculated from the standard deviation in four regions of interest (ROIs) of 1.5 x 1.5 x 1.5 mm³, followed by a correction based on the standard deviation from an area with uniform intensity. This step requires calculation of the maximum modulation between the materials in the ROI, which is referred to as M_0 . According to the formula,¹³ $M_0 = \frac{|CT_{Al} - CT_{Mylar}|}{2}$, the value was determined from the CT numbers for aluminum and Mylar in each scan. **Figure 2.3** contains reconstructed images used to assess spatial resolution.

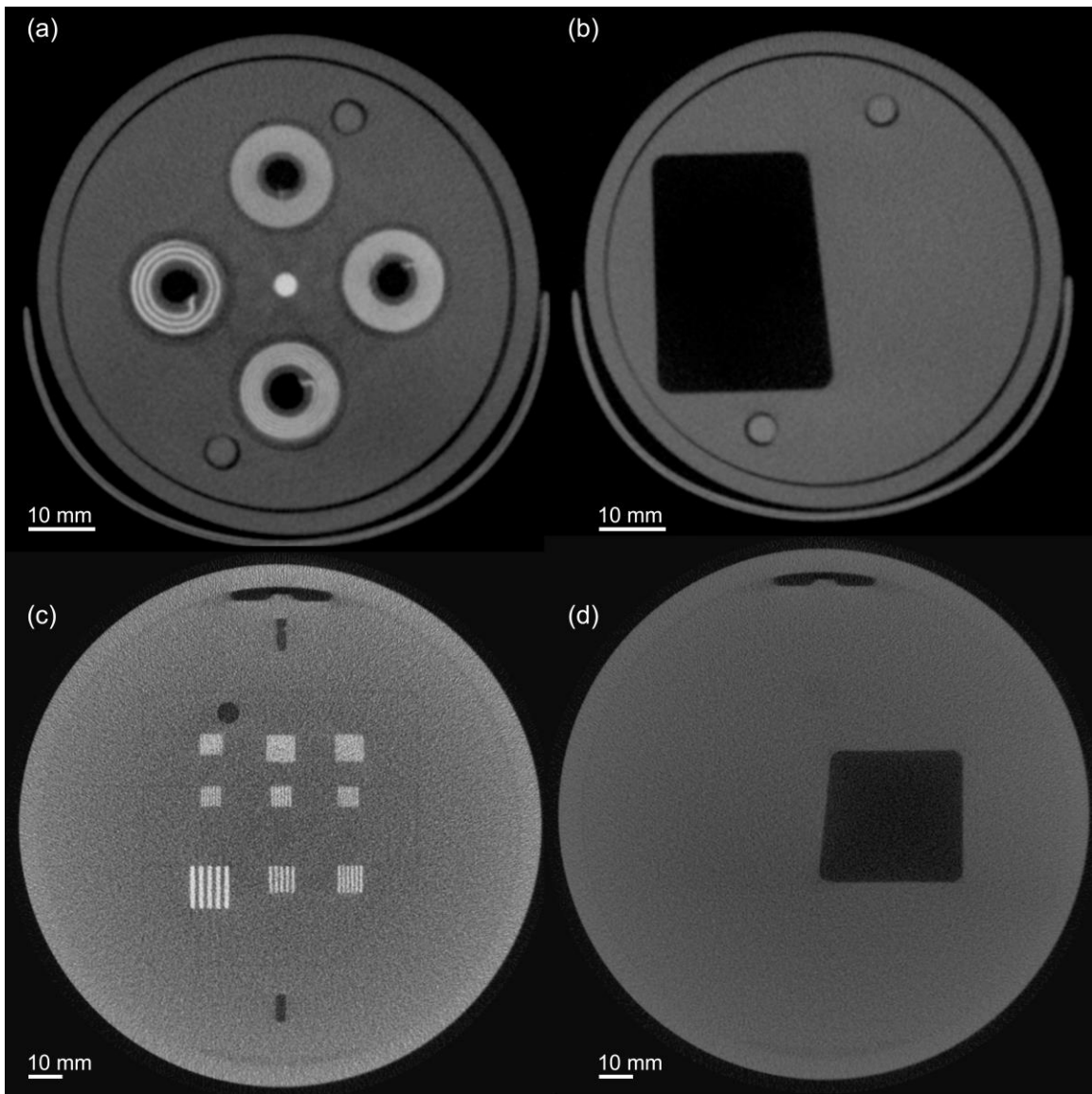


Figure 2.3: Images of small phantom a) resolution coils, created with alternating aluminum and Mylar sheets, b) the 5° axial slanted-edge image. In the large phantom, c) bar pattern plate, created with alternating aluminum and Mylar sheets, and d) the axial slanted-edge image, showing a 5° from the central axis.

2.2.4 Linearity

Both image quality phantoms contain a plate for evaluation of a CBCT system's linearity (**Figure 2.4**), based on measurements within regions containing known concentrations of iodinated contrast agent or bone mineral.^{15, 46} Images within these plates were used to calculate the average CT number within a $2 \times 2 \times 2 \text{ mm}^3$ region at the centre of each cylinder or vial. The relationship between signal intensity and material density was determined by linear regression analysis using GraphPad Prism 6.0 (GraphPad Software, San Diego, CA).

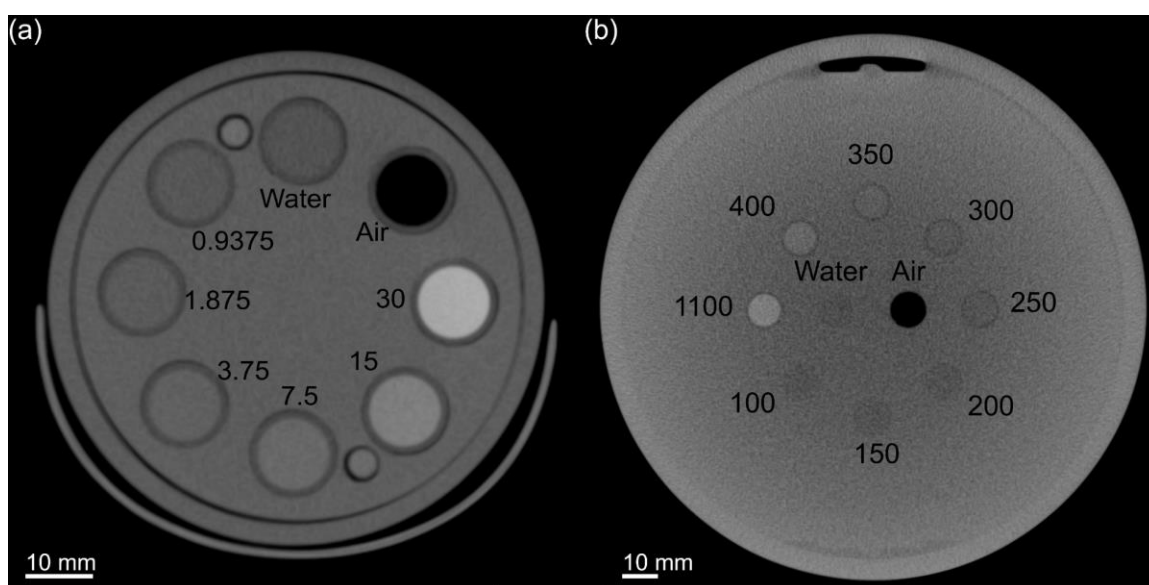


Figure 2.4: Image of linearity plates used in the small phantom (a) containing vials of air, water, and iodine (Omnipaque) in various concentrations, measured in mg ml^{-1} . Image of linearity plate in large phantom (b) containing plastics within various bone mineral densities, measured in $\text{mg hydroxyapatite cm}^{-3}$.

2.2.5 Uniformity

In both phantoms, uniformity was measured in uniform areas of acrylic plastic or water within the phantom. **Figure 2.5a and 2.5b** show slices reconstructed from the volume image from both phantoms in an area of uniform density surrounded by an acrylic wall. Using MicroView, uniformity was calculated using the average CT number from ROIs ($10 \times 10 \times 0.2 \text{ mm}^3$) placed at the centre and around the periphery of the phantom in the

image. The average CT number in peripheral ROIs was subtracted from central ROIs to quantify the system's uniformity. A line profile was also plotted across the central slice to analyze variation of CT numbers across the field-of-view (FOV).

2.2.6 Noise

Image noise was reported as the standard deviation at the centre of the image inside a uniform ROI (10 x 10 x 0.2 mm³). Large (96 kVp) and small (90 kVp) phantoms were analyzed over 15 mm with ROIs spaced 1 mm between each measurement (n = 15), shown as the red ROI in **Figures 2.5c and 2.5d**. The relationship between image noise and exposure was determined by obtaining images of each phantom, as described in Section B. The total measured noise (σ_{total}) can be considered as a quadrature summation of photon noise (σ_{photon}) and system noise (σ_{system}).^{19, 30} Consequently, the average noise measured as a function of photon flux can be fitted with non-linear regression to the equation, $\sigma^2_{total} = A \times E^{-1} + \sigma^2_{system}$, where σ_{total} is measured noise in HU, E is exposure in mAs, and A and σ^2_{system} are constant terms. The constant term A is a scaling factor between variance and photon flux, which is unique to each CT scanner. Non-linear fitting was performed using the Levenberg-Marquardt algorithm (GraphPad Prism 6.0).

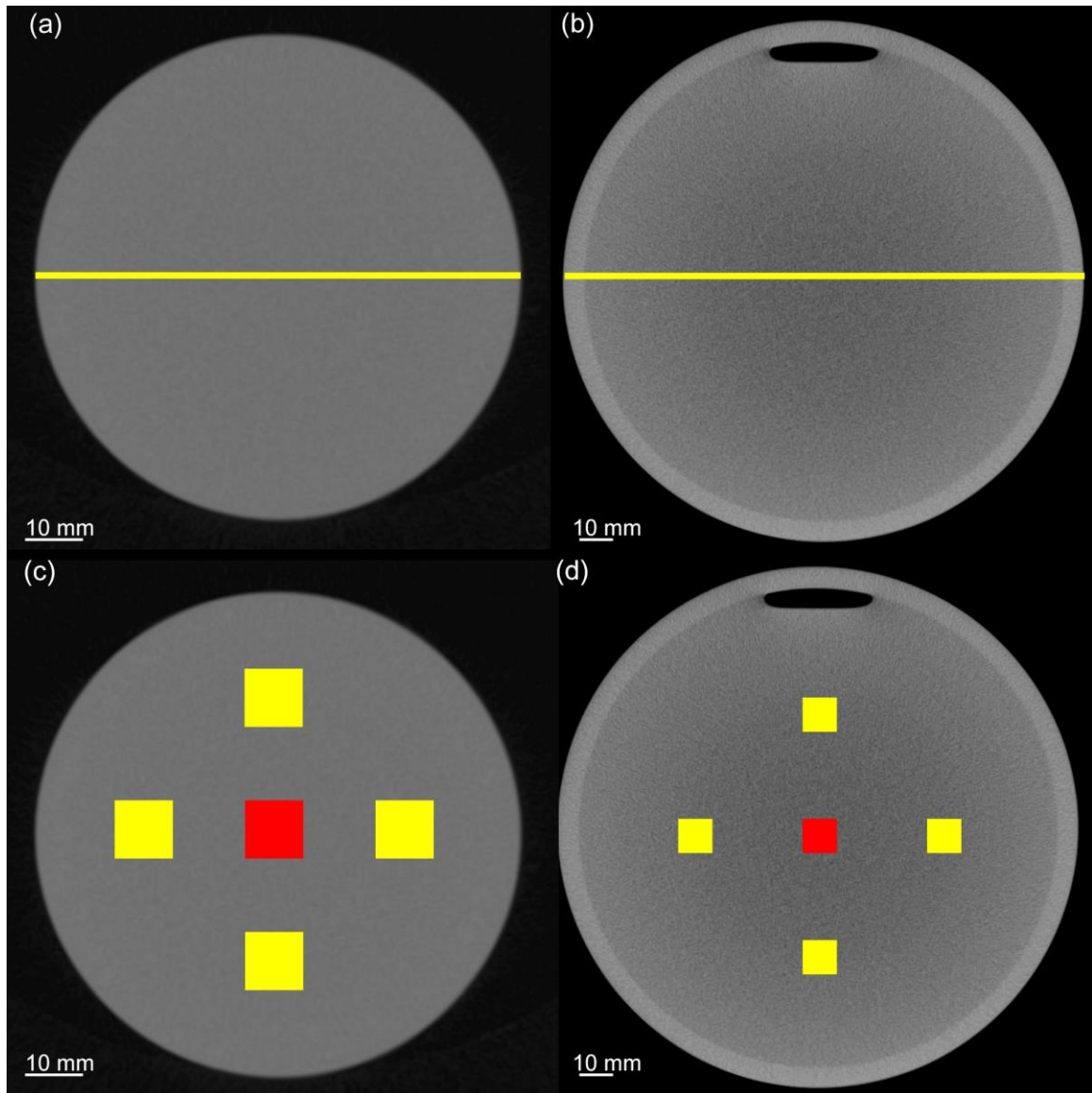


Figure 2.5: Slices through an area of uniform density in the small (a) and large (b) phantoms, show the location of the line profile used to characterize system uniformity. ROIs located within the small (c) and large (d) phantoms used to assess uniformity (red & yellow) and noise (red only).

2.2.7 Geometric Accuracy

Geometric accuracy was analyzed in both phantoms using test plates containing metal beads spaced at a known distance. In the large phantom, the evaluation of the axial (z-slice) plane was conducted using a Lexan plate with five steel beads (0.8 mm diameter). The spacing between the four outer beads was 40 ± 0.025 mm with an additional bead in the centre. An additional plate with thirty $280 \mu\text{m}$ diameter tungsten-carbide beads (spaced 15 mm apart) was used to evaluate the accuracy in both the x-y direction and z-direction. In the small phantom, four beads were spaced in four corners 35 mm apart, and one bead was placed in the centre, 24.75 mm apart from the other four beads. The distance between the beads was calculated by determining the centroids of each bead (using seeded region growing to automatically extract the beads),⁴⁴ which were used to calculate the distance between neighbouring beads. Image slices used to determine geometric accuracy from both phantoms are demonstrated in **Figure 2.6**.

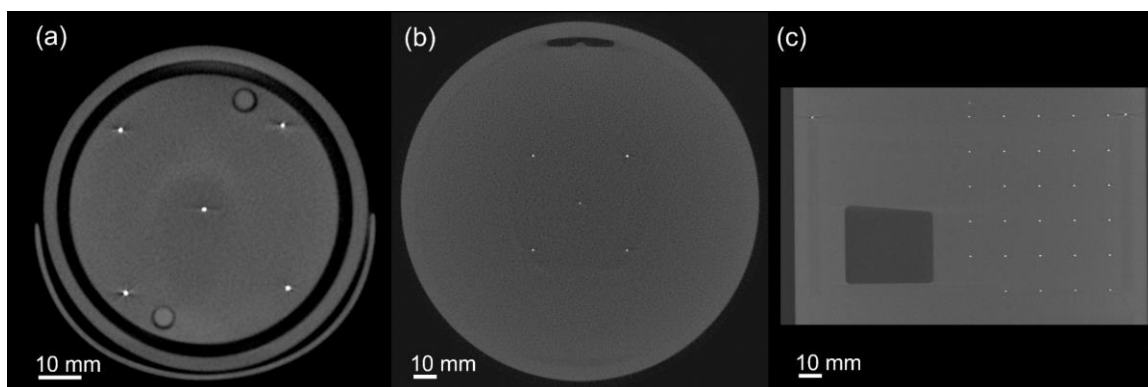


Figure 2.6: a) slice from small phantom with five steel beads in axial plane. b) Slices from large phantom containing: five steel beads in the axial plane, and c) in (x-z) direction with thirty tungsten-carbide beads spaced 15 mm in all directions.

2.2.8 Effective Dose Estimation

Radiation doses from CBCT image acquisitions were simulated using a PC-based Monte Carlo method (PCXMC 2.0) developed by Finnish Radiation and Nuclear Safety Authority.⁵⁴ This software has been used in previous studies to estimate effective dose to patients.⁸ The maximum possible tube voltage and current (96kV, 0.24 mAs per

projection) for each 300 and 450 image projection protocols were used as inputs to PCXMC. The x-ray spectrum in PCXMC was set to match the 12° anode angle, as well as the 3.5 mm aluminum and 0.5 mm copper filtration of the CBCT system. The effective dose was calculated based on the system geometry of the CBCT scanner and ICRP 103 weighting coefficients. The effective dose for each image projection protocol was also estimated using a previously described method that utilizes CT dose index (CTDI) absorbed doses (6.9 mGy & 10.4 mGy) for the respective 300- and 450-image projection protocols, FOV (13 cm), and an organ specific weighting coefficient for distal extremities (0.0005 mSv mGy⁻¹).^{34, 60}

2.2.9 Statistical Analysis

Significant differences were determined between mean signal intensities observed in all tests, and mean values in HU were compared with a one-way analysis of variance (ANOVA), with significance accepted for $p < .05$. For linearity tests, linear regression was performed to establish a linear relationship between parameters if the slope was found to be significantly different from zero, with significance at $p < .05$. Statistical analyses were performed using GraphPad Prism 6.0.

2.3 Results

2.3.1 Spatial Resolution

Analysis of spatial resolution with the installed reconstruction algorithm and beta-reconstruction algorithm yielded MTF10 results of 1.41 ± 0.07 lp/mm and 1.70 ± 0.11 lp/mm, respectively. Statistical significance was observed between installed and beta reconstruction algorithms, regardless of AINO application in the small phantom ($p < .01$). The CBCT system resolved up to the 1.0 lp/mm, 1.67 lp/mm, and 1.67 lp/mm coils using the current algorithm, beta algorithm, and beam-hardening correction, respectively. **Figure 2.7** demonstrates MTF profiles obtained from slanted-edge image analysis for high-resolution scans using the small phantom.

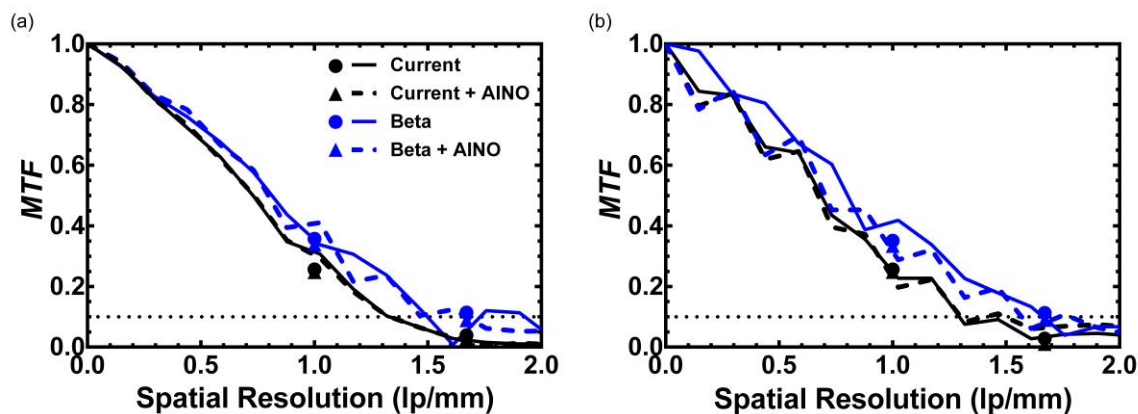


Figure 2.7: Modulation transfer function of the cone-beam CT system measured from the slanted-edge plate (lines) and resolution coils (symbols) of the small phantom using the 6s (a) and 9s (b) exposure acquisitions.

In the axial direction of the large phantom, analysis of spatial resolution using installed reconstruction algorithm, beta-reconstruction algorithm, and beam-hardening correction produced results of 1.41 ± 0.14 lp/mm, 1.69 ± 0.47 lp/mm, and 1.55 ± 0.21 lp/mm, respectively. No significant differences were observed between reconstructed image volumes in the axial plane of the large phantom ($p=0.07$). Analysis of bar patterns to obtain the MTF was able to resolve all bar patterns up to 1.4 lp/mm, 1.6 lp/mm, and 1.6 lp/mm for the current algorithm, beta algorithm, and beam-hardening correction, respectively. In the transverse plane, limiting spatial resolutions of 2.08 ± 0.08 lp/mm, 2.01 ± 0.13 lp/mm, and 2.06 ± 0.13 lp/mm were observed for the installed reconstruction algorithm, beta-reconstruction algorithm, and beam-hardening correction, respectively. Statistical significance was observed between image volumes reconstructed using the beta and AINO algorithms with image volumes reconstructed using either the installed algorithm, or beam-hardening correction ($p<.01$). **Figure 2.8** demonstrates MTF profiles obtained from analysis of slanted-edge images within the large phantom for high-resolution scans, along with results from the bar pattern. All spatial resolution tests demonstrated excellent agreement between resolution coils, bar patterns, and slanted-edge image results. The CBCT scanner exceeds manufacturer specifications for limiting spatial resolution (i.e. greater than 1.25 lp/mm) for each reconstruction and acquisition protocol.

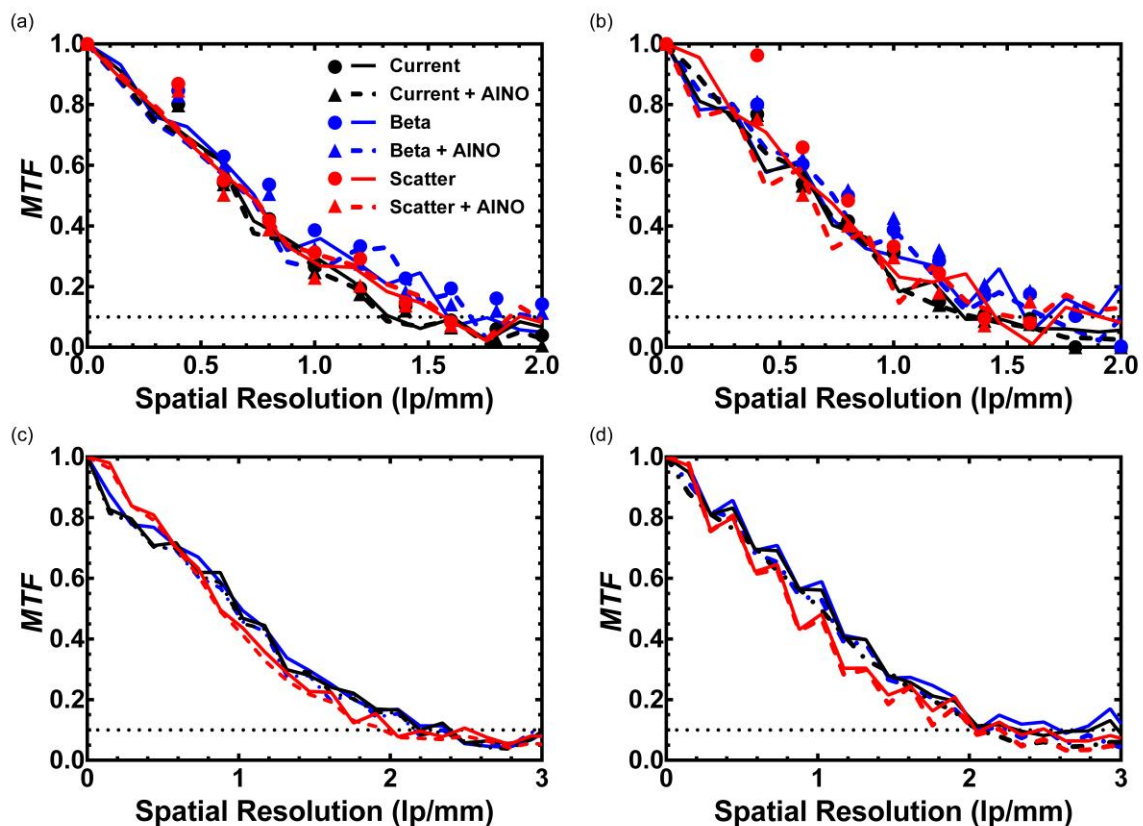


Figure 2.8: Modulation transfer function of the cone-beam CT system measured from the slanted-edge (line) and bar patterns (symbols) in the large phantom, using (a) 6s and (b) 9s exposures. Additionally, modulation transfer function evaluated with the slanted-edge located within the x-y plane in the large phantom, using (c) 6 and (d) 9s exposures.

2.3.2 Linearity

Figures 2.9a and 2.9b contain plots of the calculated CT numbers (HU) as a function of iodine concentration in the small phantom. Linear regression of the small phantom revealed no significant differences between both acquisition modes ($p=0.87$), therefore a pooled regression equation could represent all results. The pooled linear regression equations for the small phantom is $S = 46.3 \text{ (HU ml mg}^{-1}) \cdot C + 8.24 \text{ (HU)}$, where the signal intensity (S) is a function of increasing iodine concentration (C) in ml mg^{-1} ($R^2=0.998$). **Figures 2.9c and 2.9d** contain plots of the calculated HU as a function of the bone-mineral density (BMD) in the large phantom. Linear regression of the large phantom revealed no significant differences between acquisition modes ($p=0.99$),

therefore a pooled regression equation ($\text{Intensity} = \text{BMD} \cdot 1.26 \text{ HU} / \text{mg cm}^{-3} + 74.86 \text{ HU}$) could determine the expected CT number from the regression line ($R^2=0.998$).

Figures 2.9e and 2.9f show the impact of the beam-hardening correction on the system's linearity in the large phantom. Linear regression of the beam-hardening corrected image revealed no significant differences between length of scan ($p=0.85$), therefore the pooled regression equation ($\text{Intensity} = \text{BMD} \cdot 1.11 \text{ HU} / \text{mg cm}^{-3} + 53.42 \text{ HU}$) could calculate the expected CT number from the regression line ($R^2=0.992$). The system demonstrates a high degree of linearity ($p < .01$) with all algorithms tested in response to signal intensities that will be encountered in clinical musculoskeletal imaging.

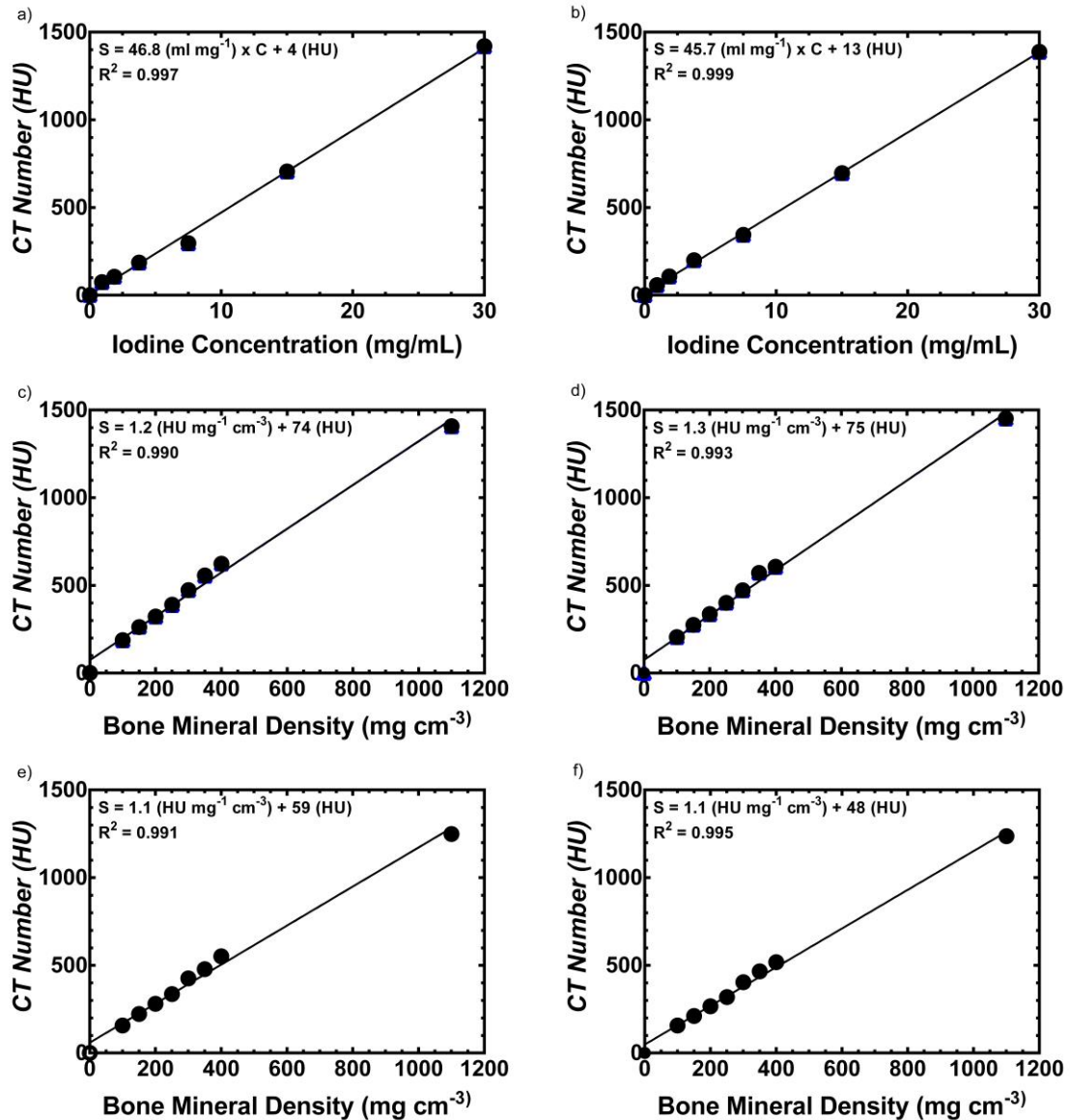


Figure 2.9: Plots of measured CT number versus known iodine concentrations, including results of linear regression, within the linearity plate of small phantom using the (a) 300- and (b) 450- image projection protocols. Plots of measured CT number versus known bone mineral densities, including results of linear regression, within the linearity plate of large phantom using the (c) 300- and (d) 450-image projection protocols. A beam-hardening correction was applied to images of the large phantom using the (e) 300- and (f) 450- image projection protocols.

Table 2.2: CT numbers (HU) and standard deviation (HU), measured in one central and four peripheral ROIs for the 300-image projection protocol in the small phantom.

Average difference and average measured standard deviation (\pm SD) were calculated.

	Current		Current +AINO		Beta		Beta +AINO	
	CT #	SD						
Centre	138	40	138	27	138	74	138	51
Left	149	39	148	26	149	70	149	48
Top	142	37	142	25	142	67	141	46
Right	148	39	148	27	148	71	148	48
Bottom	146	41	146	27	46	74	146	51
Average difference from the centre	7.9 \pm 2.8		8.0 \pm 2.9		8.0 \pm 2.9		8.2 \pm 2.8	
Average SD	39 \pm 2		27 \pm 1		71 \pm 3		49 \pm 2	

Table 2.3: CT numbers (HU) and standard deviation (HU), measured in one central and four peripheral ROIs for 450-image projection protocol in the small phantom. Average difference and average measured standard deviation (\pm SD) were calculated.

	Current		Current +AINO		Beta		Beta +AINO	
	CT #	SD						
Centre	142	32	142	22	142	60	142	41
Left	158	32	158	22	158	57	158	39
Top	152	30	152	21	151	55	152	37
Right	158	32	158	22	157	57	157	39
Bottom	154	33	154	22	153	60	153	41
Average difference from the centre	13.4 \pm 2.9		13.5 \pm 2.9		13.2 \pm 2.9		13.3 \pm 2.9	
Average SD	32 \pm 1		22 \pm 1		58 \pm 2		39 \pm 2	

Table 2.4: CT numbers (HU) and standard deviation (HU), measured in one central and four peripheral ROIs for the 300-image projection protocol in the large phantom.

Average difference and average measured standard deviation (\pm SD) were calculated.

	Current		Current +AINO		Beta		Beta +AINO		Scatter		Scatter +AINO	
	CT #	SD	CT #	SD	CT #	SD	CT #	SD	CT #	SD	CT #	SD
Centre	-1	73	-1	49	-1	134	-1	93	1	104	1	73
Left	113	73	113	50	113	131	113	92	72	102	72	71
Top	115	67	114	47	115	119	114	82	77	93	76	64
Right	103	75	103	52	104	134	104	94	65	104	65	73
Bottom	122	81	121	56	122	145	122	108	70	111	70	79
Average difference from the centre	113.9 \pm 7.7		113.7 \pm 7.4		114.1 \pm 7.5		113.9 \pm 7.3		70.2 \pm 5.1		70.1 \pm 5.0	
Average SD	74 \pm 5		51 \pm 3		133 \pm 9		93 \pm 6		102 \pm 7		72 \pm 5	

Table 2.5: CT numbers (HU) and standard deviation (HU), measured in one central and four peripheral ROIs for the 450-image projection protocol in the large phantom.

Average difference and average measured standard deviation (\pm SD) were calculated.

	Current		Current +AINO		Beta		Beta +AINO		Scatter		Scatter +AINO	
	CT #	SD	CT #	SD	CT #	SD	CT #	SD	CT #	SD	CT #	SD
Centre	0	61	0	41	-0	112	0	77	1	85	1	59
Left	110	61	110	42	110	109	110	76	69	83	69	58
Top	112	55	112	40	112	98	113	68	70	74	70	52
Right	103	62	103	43	103	110	103	77	61	83	61	58
Bottom	119	67	119	47	120	119	120	84	69	90	69	64
Average difference from the centre	110.8 \pm 6.9		110.8 \pm 7.0		111.4 \pm 6.9		111.2 \pm 6.9		66.4 \pm 3.9		66.6 \pm 3.8	
Average SD	61 \pm 4		42 \pm 3		109 \pm 7		76 \pm 5		83 \pm 5		58 \pm 4	

2.3.3 Uniformity

Figures 2.10 shows multiple line profiles taken from each of the four reconstructions in the small phantom. **Table 2.2** and **Table 2.3** demonstrate the measured signal intensity and noise in each of the five ROIs used to calculate image uniformity. Across all algorithms, the average differences in signal intensity values between the central and peripheral regions were 8.0 and 13.4 HU for the respective 6 second and 9 second exposures. All line profiles for the small phantom were uniform and within manufacturer guidelines, regardless of reconstruction algorithm.

Figures 2.11 shows multiple line profiles taken from the six reconstructions of the large phantom. **Table 2.4** and **Table 2.5** demonstrate the measured signal intensity and noise in each of the five ROIs used to calculate image uniformity. Across all algorithms, the average differences in signal intensity values between the central and peripheral regions were 113.9 and 111.1 HU for the respective 300 and 450 frame acquisitions. Using the beta reconstruction algorithm, a beam-hardening correction was applied to image volumes of the large phantom, which reduced average signal intensities differences to 70.2 and 66.5 HU for the corresponding 300 and 450 frame acquisitions. **Table 2.4** and **Table 2.5** also demonstrate the impact of the beam-hardening correction on the average differences in signal intensity. **Figure 2.11e** and **2.11f** demonstrate the effect of the beam-hardening correction on line profiles taken on the central reconstructed slice.

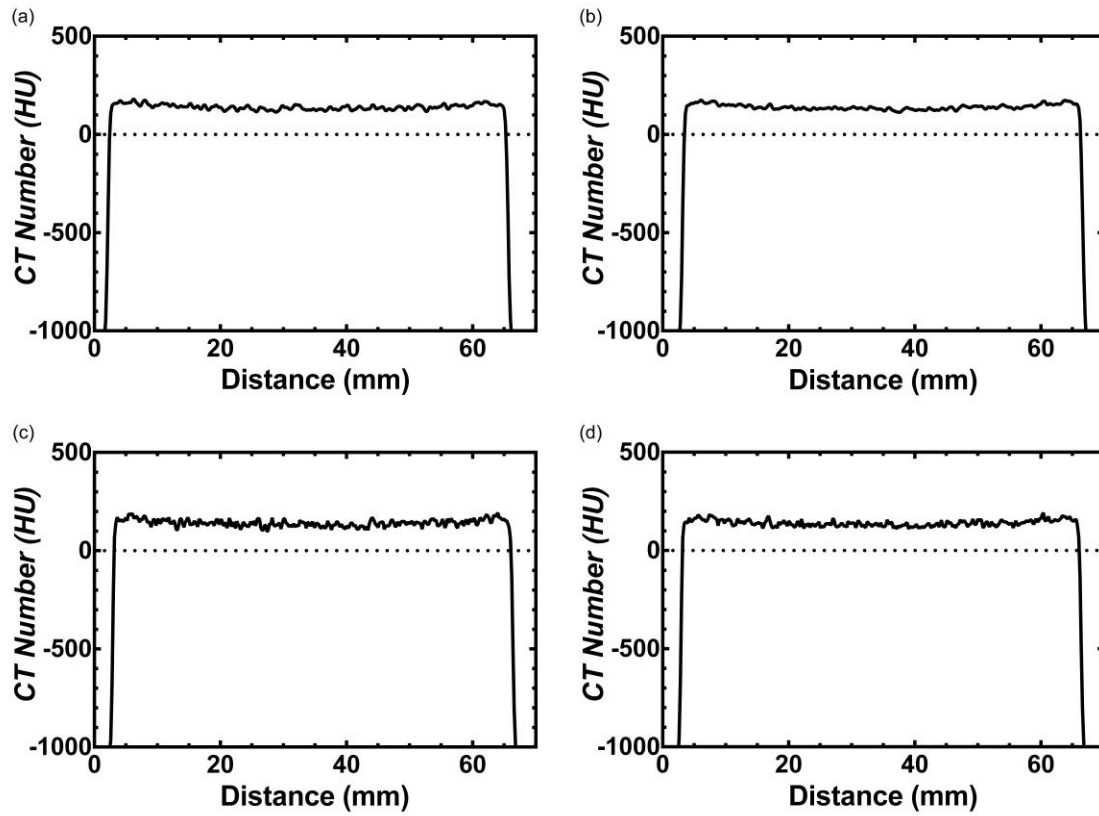


Figure 2.10: Radial signal profiles taken through the centre of the small phantom using the: (a) current, (b) current with AINO, (c) beta, and (d) beta with AINO reconstruction algorithms. All line profiles were obtained on the central reconstructed slice.

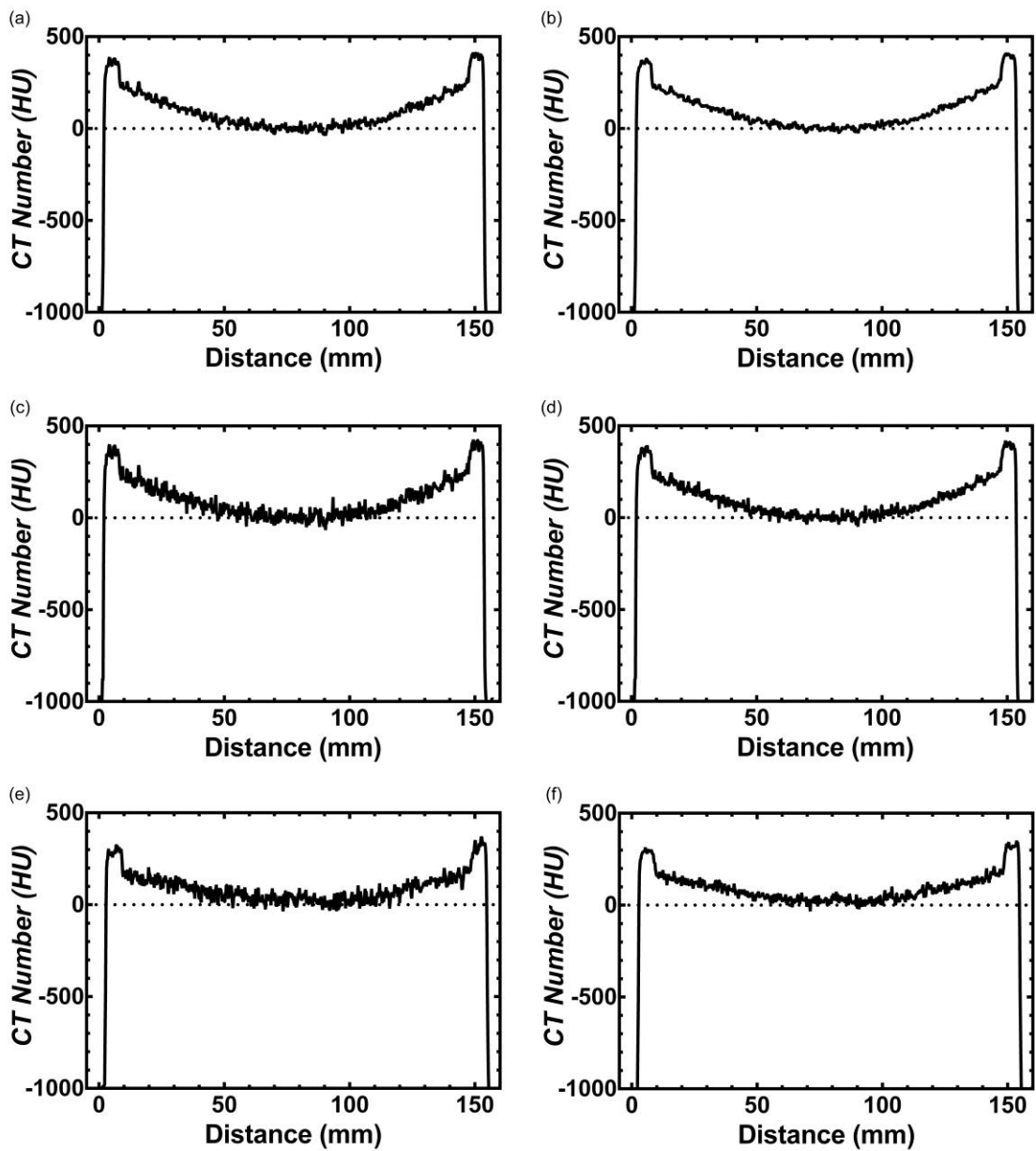


Figure 2.11: Radial signal profiles taken through the centre of the large phantom using the: (a) current, (b) current with AINO, (c) beta, (d) beta with AINO, (e) beam-hardening correction, and (f) beam-hardening correction with AINO reconstruction algorithms. All line profiles were obtained on the central reconstructed slice.

Table 2.6: Results of non-linear regression of standard deviations occurring in the small and large phantoms. The equations are shown in the form, $\sigma^2_{\text{total}} = A * E^{-1} + \sigma^2_{\text{system}}$, where R^2 value for all equations = 0.99.

	Small phantom		Large Phantom	
	300 Frames	450 Frames	300 Frames	450 Frames
Current	$774 * E^{-1} + 29$	$903 * E^{-1} + 27$	$3044 * E^{-1} + 56$	$3864 * E^{-1} + 46$
Current+AINO	$512 * E^{-1} + 22$	$593 * E^{-1} + 22$	$2067 * E^{-1} + 38$	$2634 * E^{-1} + 31$
Beta	$1594 * E^{-1} + 44$	$2001 * E^{-1} + 38$	$5941 * E^{-1} + 100$	$7761 * E^{-1} + 77$
Beta+AINO	$774 * E^{-1} + 29$	$903 * E^{-1} + 27$	$3044 * E^{-1} + 56$	$3864 * E^{-1} + 46$
Scatter	N/A	N/A	$3044 * E^{-1} + 56$	$5415 * E^{-1} + 50$
Scatter+AINO	N/A	N/A	$3044 * E^{-1} + 56$	$4950 * E^{-1} + 37$

2.3.4 Noise

Figure 2.12 demonstrates the relationship between image noise as a function of exposure, with a best-fit line connecting the points. The beta algorithm generated image volumes with an 88% increase in image noise, when compared to the current clinical reconstruction algorithm. A beam-hardening correction implemented using the beta reconstruction algorithm diminished this discrepancy in image noise from 88% to 30% when compared to the current clinical algorithm. In comparison to the beta reconstruction algorithm, image noise was reduced by 30% versus an uncorrected image volume. Overall, the AINO algorithm was able to reduce noise in each image set by approximately 30%, regardless of phantom diameter or reconstruction algorithm. All image volumes reconstructed with the current clinical algorithm and beam-hardening correction meet the manufacturer's guidelines of less than 100 HU standard deviation when using a large-sized phantom. **Table 2.6** shows results of the non-linear regression describing the relationship between exposure and noise, using the equation previously described in **Section 2.2.6**.

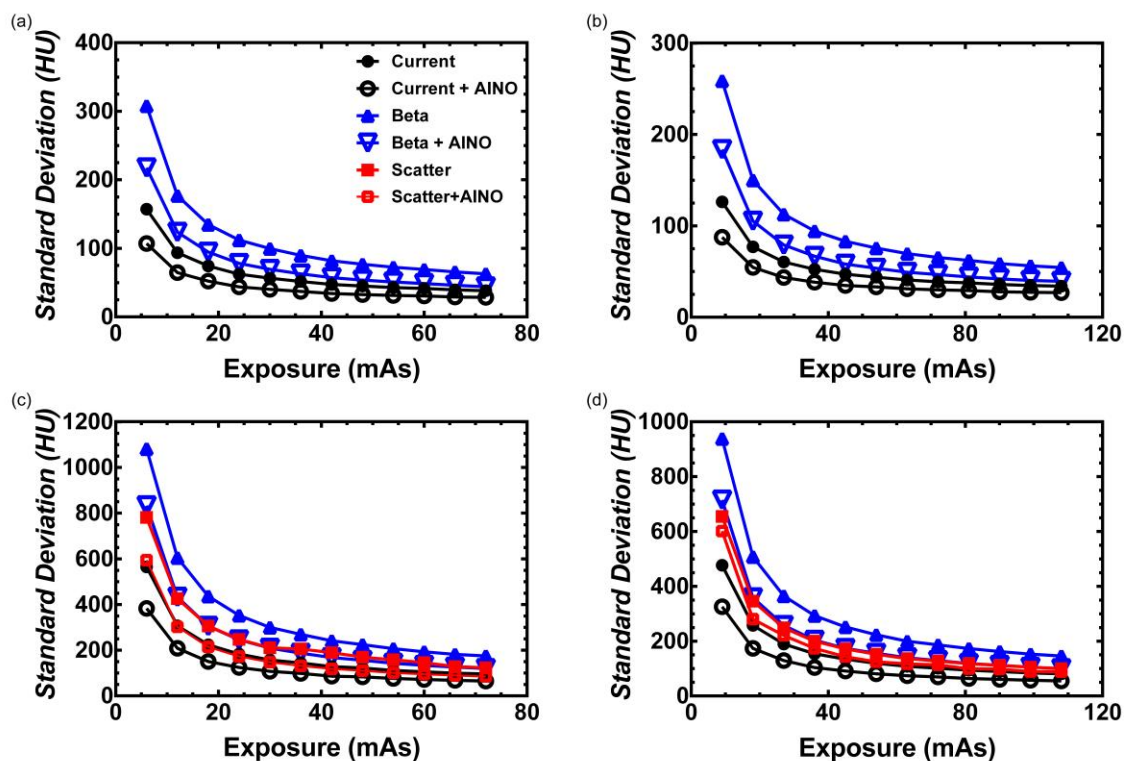


Figure 2.12: Measured noise in the small phantom using the 300 frame (a) and 450 frame (b) protocols, expressed as average standard deviation of the signal intensity (HU), plotted as a function of increasing exposure. Tube voltage used for the small phantom was 90 kVp, with tube current varying from 1 to 12 mA, using 6s (a) or 9s (b) exposure time. Similarly, measured noise in the large phantom using the 300 frame (c) and 450 frame (d) protocols, expressed as average standard deviation of the signal intensity (HU), plotted as a function of increasing exposure. Tube voltage used for the large phantom was 96 kVp, with tube current varying from 1 to 12 mA, using 6s (c) or 9s (d) exposure time.

2.3.5 Geometric Accuracy

Average distance between centroids of the four steel beads, in the small phantom, was calculated to be 35.01 ± 0.07 mm compared to the nominal 35 mm spacing ($p=0.28$). In the large phantom, the average distance between centroids of the four steel beads, spaced 40 mm apart, was calculated to be 39.98 ± 0.16 mm for the axial geometry ($p=0.55$). In the transverse plane, the average distance between the centroids of the tungsten-carbide beads was found to be 15.01 ± 0.06 mm in the (x-y) plane and 15.07 ± 0.16 mm in the z-

direction (slice direction), compared to the nominal 15 mm spacing. No statistical significance was observed between all algorithms in the transverse plane ($p=0.07$). All results pass the manufacturer specifications and demonstrate excellent in-plane and out-of-plane geometric accuracy, regardless of exposure time, reconstruction algorithm, or diameter of the image quality phantom.

2.3.6 Effective Dose Estimation

Using PCXMC, the effective dose was calculated to be 14 μSv , and 21 μSv , for the respective 300, and 450 image projection acquisitions. Alternatively, the effective dose was calculated to be 45 μSv , and 68 μSv , for the respective 300-, and 450- image projection acquisitions when using the CTDI absorbed dose, FOV, and an organ specific weighting coefficient for distal extremities. The latter method was expected to produce a higher effective dose estimate, since the organ-specific weighting coefficients were derived from conventional CT.

2.4 Discussion

The Planmed Verity cone-beam CT scanner demonstrates excellent performance, consistent with manufacturer guidelines, while acquiring image volumes at a low-dose. Image quality phantoms in this study resembled the average-sized elbow and an average-sized knee. Therefore, the system's performance was evaluated with objects that mimic the anatomy encountered in future clinical musculoskeletal imaging studies, in terms of spatial resolution, noise, uniformity, linearity, geometric accuracy, and effective dose. Overall, the scanner passed all image quality tests according to the manufacturer's guidelines, apart from the uniformity test using the large-sized phantom. This demonstrates the need for additional beam-hardening correction when scanning structures with larger diameters.

Over the range of densities analyzed, the scanner demonstrated a highly linear response, regardless of phantom size or reconstruction algorithm used. The signal-level calibration of the CBCT system was excellent, with water and peripheral air returning values of 0.48 and -1120 HU in the small phantom, and 0.49 and -975 HU in the large phantom. Upon further investigation with the large phantom, air inside the linearity plate returned a value

of -642 HU. Previous researchers observed similar effects with earlier CT scanners; they attributed increases or decreases in CT number to scanner-dependent beam-hardening corrections, which are crucial to the magnitude and direction of environmental density artefacts.^{24, 55} A similar decrease in signal intensity was observed in the analysis of a uniform water phantom with CBCT imaging.⁵¹ The beam-hardening correction was applied to large-phantom image volumes that resulted in CT numbers for water, peripheral air, and internal air, returning intensity values of 0.46 HU, -1000 HU, and -815 HU, respectively. The observed value of -815 was approximately 20% greater than expected; however, these results are comparable to previous studies demonstrating inaccuracies in HU signal intensity values for internal air cavities.²² Although there was a discrepancy between internal and peripheral air intensity values, the scanner maintains a linear response to materials of increasing linear attenuation coefficients, regardless of reconstruction algorithm.

Uniformity and noise measurements are dependent on the size of the object; therefore, the use of small- and large-sized phantoms was necessary to cover possible anatomies that may be encountered in future studies. Signal uniformity was preserved within 50 HU with the small-sized phantom; however, image volumes of the large-sized phantom did not sustain signal uniformity within 50 HU, which was attributed to beam-hardening and scatter. The average difference in signal uniformity was not impacted by the AINO algorithm for either phantom used in this study. A cupping effect was detected on the line profile intensity plot for the large phantom, which significantly contributes to lower homogeneity of the image.⁴² Similar results were observed with the analysis of a uniform water phantom with flat-panel CBCT images.⁵¹ Typically, CBCT images have larger occurrence and magnitude of physics-based artefacts, when compared to conventional CT.^{5, 58, 59} Within the beta algorithm, a beam-hardening correction can be applied to reduce signal intensity differences from 114 HU to 70 HU in the 6s exposure, and from 111 HU to 66 HU in the 9s exposure. Although these measurements do not meet manufacturer requirements, the beam-hardening correction was able to improve image uniformity by approximately 40%. The currently installed reconstruction algorithm produced image noise measurements within manufacturer guidelines, regardless of AINO algorithm implementation, diameter of phantom, or number of frames obtained. The beta

reconstruction algorithm passed manufacturer guidelines with the small-sized phantom; however, the scanner required the AINO algorithm or a beam-hardening correction to pass manufacturer standards with respect to the large-sized phantom. We have demonstrated the effects of photon flux on noise at 96 kVp and 90 kVp with clinical scan exposure settings. **Figure 2.12** shows that exposures between 30-50 mAs would optimize image quality and dose; exposures above 9 mAs may not significantly improve the image quality, in terms of noise. Conventional CT demonstrates less noise and better soft tissue contrast when compared to CBCT.^{11, 37} The decrease of soft-tissue contrast resolution in CBCT is caused in part by scattered radiation, which increases noise and decreases the contrast-to-noise ratio.^{1, 2, 50} Overall, previous studies have demonstrated CBCT images provide diagnostic information not apparent on radiographs and this information is obtained at a lower radiation dose than conventional CT.^{17, 31} The AINO algorithm allows for lower tube current during exposure, reducing image noise by approximately 30% in all cases, allowing for lower effective doses while maintaining optimal image quality.

Spatial resolution was evaluated quantitatively and qualitatively in both phantoms through slanted-edge images, or a bar pattern. Using slanted-edge images in the axial plane, overall limiting spatial resolution (MTF10) with the installed and beta reconstruction algorithms was 1.42 lp/mm and 1.68 lp/mm, respectively. This result is consistent with bar pattern analysis, which indicated objects at 1.4 and 1.6 lp/mm could be resolved for the respective current and beta algorithms. The calculation of the MTF using the bar pattern is immune to noise and is not influenced by the orientation of the image.¹³ In addition, analysis with bar patterns uses simpler tools to obtain the MTF, when compared to the conventional slanted-edge image analysis. In the transverse plane, the overall limiting spatial resolution using the current and beta reconstruction algorithms was 2.00 lp/mm and 1.97 lp/mm, respectively. Discrepancies between axial and transverse planes were due to excessive noise in the edge response function, which influences the derivation of the edge response function to the line spread function when calculating MTF.^{45, 53} Furthermore, spatial resolution has a directional dependency in the transverse plane, which may impact measurements when an object is located in the periphery, such as the slanted-edge in the transverse plane.⁴⁵ Throughout the study, no statistical significance was observed between AINO reconstructed images and the

original reconstruction, which suggests the AINO algorithm does not degrade spatial resolution. Significant differences were shown between the current and beta reconstruction algorithms, regardless of the image phantom diameter or application of AINO algorithm ($p < .01$). Regardless, the spatial resolution passed manufacturer standards using qualitative and quantitative analyses. Regarding geometric accuracy, there were no statistically significant discrepancies, indicating excellent geometric accuracy in all imaging planes with the peripheral CBCT scanner. Geometric accuracy is essential for accurate patient-to-image registration using either anatomical landmarks or fiducial markers.²¹ These results were comparable to studies analyzing spatial resolution and geometric accuracy of various CBCT scanners.^{4, 16, 32} We have demonstrated the beta reconstruction improves spatial resolution and uniformity, while maintaining linearity and geometric accuracy, at the cost of increased image noise. The beam-hardening correction was able to retrospectively enhance image uniformity and reduce image noise, without affecting linearity, geometric accuracy, and spatial resolution.

The effective dose for the Planned Verity was calculated to be 14 μSv , and 21 μSv for the respective 300-, and 450-image projection acquisitions using PCXMC. These results were comparable to measurements obtained in previous studies that reported an effective dose of 13 μSv .^{34, 36} The effective dose estimation based on CTDI absorbed dose, FOV, and organ specific weighting coefficient for distal extremities, resulted in calculations of 45 μSv , and 68 μSv for the 300 and 450 image projections, respectively. For a CBCT system, it may not be appropriate to characterize dose with the conventional CTDI approach, since reconstructed image volumes are reconstructed using multiple independent 2D projections, rather than contiguous thin slices.¹⁸ Previous studies have demonstrated effective dose calculations that use dose-length product with an organ-specific weighting coefficient are inaccurate.^{7, 9} Although there is a discrepancy between the two effective dose estimation methods, the results are comparable to approximately two chest x-rays, where the effective dose may vary from 7 – 50 μSv per view.⁴¹ Overall, the effective dose associated with this scanner for all imaging acquisitions was minimal compared to 2.2 mSv, the average annual effective dose resulting from background radiation in Canada.¹⁰ The stochastic effects of ionizing radiation arising from diagnostic imaging has been associated with a cancer risk coefficient of $5.5 \times 10^{-2} \text{ Sv}^{-1}$, thereby a

scan with an effective dose of 68 μSv has a 3.74×10^{-6} % increase to the stochastic effects of radiation.⁵⁷

2.5 Conclusion

To the best of our knowledge, we have performed the first quantitative performance evaluation with multiple reconstruction algorithms for the Planmed Verity cone-beam extremity CT scanner, using phantoms that mimic the size of an average knee or elbow. The system exceeds the manufacturer's guidelines in terms of resolution, noise, uniformity, geometric accuracy, and linearity at a smaller diameter, representative of the upper extremity anatomy. Except for the uniformity test, the system surpassed manufacturer specifications for resolution, noise, and geometric accuracy with the larger phantom, which simulated the lower extremity. This result was expected since objects with larger diameters create longer ray paths for the x-ray photons. This results in an increased attenuation of the x-ray beam, as well as a decreased photon flux at the detector. The peripheral CBCT imaging system demonstrates potential for studies of musculoskeletal treatments and their effects on joint biomechanics since it provides volumetric upper extremity data as well as weight-bearing 3D volumetric data about the lower extremity, while providing optimal image quality at a low dose.

2.6 References

1. Akbarzadeh, A., Ay, M. R., Ghadiri, H., Sarkar, S., & Zaidi, H. (2010). Measurement of scattered radiation in a volumetric 64-slice CT scanner using three experimental techniques. *Phys Med Biol*, 55(8), 2269-2280.
2. Alsufyani, N. A., Noga, M. L., Finlay, W. H., & Major, P. W. (2013). Topical contrast agents to improve soft-tissue contrast in the upper airway using cone beam CT: a pilot study. *Dentomaxillofac Radiol*, 42(7), 20130022.
3. Aurell, Y., Andersson, M., & Forslind, K. (2018). Cone-beam computed tomography, a new low-dose three-dimensional imaging technique for assessment of bone erosions in rheumatoid arthritis: reliability assessment and comparison with conventional radiography - a BARFOT study. *Scand J Rheumatol*, 47(3), 173-177.
4. Ballrick, J. W., Palomo, J. M., Ruch, E., Amberman, B. D., & Hans, M. G. (2008). Image distortion and spatial resolution of a commercially available cone-

- beam computed tomography machine. *Am J Orthod Dentofacial Orthop*, 134(4), 573-582.
5. Barrett, J. F., & Keat, N. (2004). Artifacts in CT: recognition and avoidance. *Radiographics*, 24(6), 1679-1691.
 6. Biswas, D., Bible, J. E., Bohan, M., Simpson, A. K., Whang, P. G., & Grauer, J. N. (2009). Radiation exposure from musculoskeletal computerized tomographic scans. *J Bone Joint Surg Am*, 91(8), 1882-1889.
 7. Brady, S. L., Mirro, A. E., Moore, B. M., & Kaufman, R. A. (2015). How to Appropriately Calculate Effective Dose for CT Using Either Size-Specific Dose Estimates or Dose-Length Product. *AJR Am J Roentgenol*, 204(5), 953-958.
 8. Choi, J. H., Maier, A., Keil, A., Pal, S., McWalter, E. J., Beaupre, G. S., . . . Fahrig, R. (2014). Fiducial marker-based correction for involuntary motion in weight-bearing C-arm CT scanning of knees. II. Experiment. *Med Phys*, 41(6), 061902.
 9. Christner, J. A., Kofler, J. M., & McCollough, C. H. (2010). Estimating effective dose for CT using dose-length product compared with using organ doses: consequences of adopting International Commission on Radiological Protection publication 103 or dual-energy scanning. *AJR Am J Roentgenol*, 194(4), 881-889.
 10. Commission, C. N. S. (2014). Natural Background Radiation in Canada.
 11. De Cock, J., Mermuys, K., Goubau, J., Van Petegem, S., Houthoofd, B., & Casselman, J. W. (2012). Cone-beam computed tomography: a new low dose, high resolution imaging technique of the wrist, presentation of three cases with technique. *Skeletal Radiol*, 41(1), 93-96.
 12. Dirschl, D. R., & Dawson, P. A. (2004). Injury severity assessment in tibial plateau fractures. *Clin Orthop Relat Res*, 423(423), 85-92.
 13. Droege, R. T., & Morin, R. L. (1982). A practical method to measure the MTF of CT scanners. *Med Phys*, 9(5), 758-760.
 14. Droege, R. T., & Rzeszotarski, M. S. (1985). An MTF method immune to aliasing. *Med Phys*, 12(6), 721-725.
 15. Du, L. Y., Umoh, J., Nikolov, H. N., Pollmann, S. I., Lee, T. Y., & Holdsworth, D. W. (2007). A quality assurance phantom for the performance evaluation of volumetric micro-CT systems. *Phys Med Biol*, 52(23), 7087-7108.
 16. Eggers, G., Klein, J., Welzel, T., & Muhling, J. (2008). Geometric accuracy of digital volume tomography and conventional computed tomography. *Br J Oral Maxillofac Surg*, 46(8), 639-644.

17. Faccioli, N., Foti, G., Barillari, M., Atzei, A., & Mucelli, R. P. (2010). Finger fractures imaging: accuracy of cone-beam computed tomography and multislice computed tomography. *Skeletal Radiol*, 39(11), 1087-1095.
18. Fahrig, R., Dixon, R., Payne, T., Morin, R. L., Ganguly, A., & Strobel, N. (2006). Dose and image quality for a cone-beam C-arm CT system. *Med Phys*, 33(12), 4541-4550.
19. Faulkner, K., & Moores, B. M. (1984). Noise and contrast detection in computed tomography images. *Phys Med Biol*, 29(4), 329-339.
20. Ferri, M., Scharfenberger, A. V., Goplen, G., Daniels, T. R., & Pearce, D. (2008). Weightbearing CT scan of severe flexible pes planus deformities. *Foot Ankle Int*, 29(2), 199-204.
21. Fitzpatrick, J. M., West, J. B., & Maurer, C. R., Jr. (1998). Predicting error in rigid-body point-based registration. *IEEE Trans Med Imaging*, 17(5), 694-702.
22. Ford, N. L., Martin, E. L., Lewis, J. F., Veldhuizen, R. A., Drangova, M., & Holdsworth, D. W. (2007). In vivo characterization of lung morphology and function in anesthetized free-breathing mice using micro-computed tomography. *J Appl Physiol* (1985), 102(5), 2046-2055.
23. Geijer, M., Borjesson, A. M., & Gothlin, J. H. (2011). Clinical utility of tomosynthesis in suspected scaphoid fracture. A pilot study. *Skeletal Radiol*, 40(7), 863-867.
24. Goodsitt, M. M., Chan, H. P., Way, T. W., Larson, S. C., Christodoulou, E. G., & Kim, J. (2006). Accuracy of the CT numbers of simulated lung nodules imaged with multi-detector CT scanners. *Med Phys*, 33(8), 3006-3017.
25. Guermazi, A., Roemer, F. W., Felson, D. T., & Brandt, K. D. (2013). Motion for debate: osteoarthritis clinical trials have not identified efficacious therapies because traditional imaging outcome measures are inadequate. *Arthritis Rheum*, 65(11), 2748-2758.
26. Gupta, R., Cheung, A. C., Bartling, S. H., Lisauskas, J., Grasruck, M., Leidecker, C., . . . Brady, T. J. (2008). Flat-panel volume CT: fundamental principles, technology, and applications. *Radiographics*, 28(7), 2009-2022.
27. Hirschmann, A., Buck, F. M., Fucntese, S. F., & Pfirrmann, C. W. (2015). Upright CT of the knee: the effect of weight-bearing on joint alignment. *Eur Radiol*, 25(11), 3398-3404.
28. Hirschmann, A., Buck, F. M., Herschel, R., Pfirrmann, C. W. A., & Fucntese, S. F. (2017). Upright weight-bearing CT of the knee during flexion: changes of the patellofemoral and tibiofemoral articulations between 0 degrees and 120 degrees. *Knee Surg Sports Traumatol Arthrosc*, 25(3), 853-862.

29. Hirschmann, A., Pfirrmann, C. W., Klammer, G., Espinosa, N., & Buck, F. M. (2014). Upright cone CT of the hindfoot: comparison of the non-weight-bearing with the upright weight-bearing position. *Eur Radiol*, *24*(3), 553-558.
30. Holdsworth, D. W., Drangova, M., & Fenster, A. (1993). A high-resolution XRII-based quantitative volume CT scanner. *Med Phys*, *20*(2 Pt 1), 449-462.
31. Huang, A. J., Chang, C. Y., Thomas, B. J., MacMahon, P. J., & Palmer, W. E. (2015). Using cone-beam CT as a low-dose 3D imaging technique for the extremities: initial experience in 50 subjects. *Skeletal Radiol*, *44*(6), 797-809.
32. Kobayashi, K., Shimoda, S., Nakagawa, Y., & Yamamoto, A. (2004). Accuracy in measurement of distance using limited cone-beam computerized tomography. *Int J Oral Max Impl*, *19*(2), 228-231.
33. Koivisto, J., Kiljunen, T., Kadesjo, N., Shi, X. Q., & Wolff, J. (2015). Effective radiation dose of a MSCT, two CBCT and one conventional radiography device in the ankle region. *J Foot Ankle Res*, *8*(1), 8.
34. Koivisto, J., Kiljunen, T., Wolff, J., & Kortensniemi, M. (2013). Assessment of effective radiation dose of an extremity CBCT, MSCT and conventional X ray for knee area using MOSFET dosimeters. *Radiat Prot Dosimetry*, *157*(4), 515-524.
35. Koivisto, J., Wolff, J., Jarnstedt, J., Dastidar, P., & Kortensniemi, M. (2014). Assessment of the effective dose in supine, prone, and oblique positions in the maxillofacial region using a novel combined extremity and maxillofacial cone beam computed tomography scanner. *Oral Surg Oral Med Oral Pathol Oral Radiol*, *118*(3), 355-362.
36. Kokkonen, H. T., Suomalainen, J. S., Joukainen, A., Kroger, H., Sirola, J., Jurvelin, J. S., . . . Toyras, J. (2014). In vivo diagnostics of human knee cartilage lesions using delayed CBCT arthrography. *Journal of orthopaedic research : official publication of the Orthopaedic Research Society*, *32*(3), 403-412.
37. Koskinen, S. K., Haapamaki, V. V., Salo, J., Lindfors, N. C., Kortensniemi, M., Seppala, L., & Mattila, K. T. (2013). CT arthrography of the wrist using a novel, mobile, dedicated extremity cone-beam CT (CBCT). *Skeletal Radiol*, *42*(5), 649-657.
38. Makarova, D. V., & Kushnyr, K. V. (2015). A Standardized Protocol for Cone-Beam Computed Tomography of the Hand and Wrist in Rheumatoid Arthritis. *Sovremennye Tehnologii V Medicine*, *7*(4), 135-139.
39. Marzo, J., Kluczynski, M., Notino, A., & Bisson, L. (2016). Comparison of a Novel Weightbearing Cone Beam Computed Tomography Scanner Versus a Conventional Computed Tomography Scanner for Measuring Patellar Instability. *Orthop J Sports Med*, *4*(12), 2325967116673560.

40. Mermuys, K., Vanslambrouck, K., Goubau, J., Steyaert, L., & Casselman, J. W. (2008). Use of digital tomosynthesis: case report of a suspected scaphoid fracture and technique. *Skeletal Radiol*, 37(6), 569-572.
41. Mettler, F. A., Jr., Huda, W., Yoshizumi, T. T., & Mahesh, M. (2008). Effective doses in radiology and diagnostic nuclear medicine: a catalog. *Radiology*, 248(1), 254-263.
42. Neubauer, J., Voigt, J. M., Lang, H., Scheuer, C., Goerke, S. M., Langer, M., . . . Kotter, E. (2014). Comparing the image quality of a mobile flat-panel computed tomography and a multidetector computed tomography: a phantom study. *Invest Radiol*, 49(7), 491-497.
43. Nicholson, J. A., Sutherland, A. G., & Smith, F. W. (2011). Single bundle anterior cruciate reconstruction does not restore normal knee kinematics at six months: an upright MRI study. *J Bone Joint Surg Br*, 93(10), 1334-1340.
44. Otsu, N. (1979). A Threshold Selection Method from Gray-Level Histograms. 5.
45. Ozaki, Y., Watanabe, H., Nomura, Y., Honda, E., Sumi, Y., & Kurabayashi, T. (2013). Location dependency of the spatial resolution of cone beam computed tomography for dental use. *Oral Surg Oral Med Oral Pathol Oral Radiol*, 116(5), 648-655.
46. Petrov, I. E., Nikolov, H. N., Holdsworth, D. W., & Drangova, M. (2011, 2011/03/03/). *Image performance evaluation of a 3D surgical imaging platform*. Paper presented at the SPIE Medical Imaging.
47. Ramdhian-Wihlm, R., Le Minor, J. M., Schmittbuhl, M., Jeantroux, J., Mahon, P. M., Veillon, F., . . . Bierry, G. (2012). Cone-beam computed tomography arthrography: an innovative modality for the evaluation of wrist ligament and cartilage injuries. *Skeletal Radiol*, 41(8), 963-969.
48. Richter, M., Seidl, B., Zech, S., & Hahn, S. (2014). PedCAT for 3D-imaging in standing position allows for more accurate bone position (angle) measurement than radiographs or CT. *Foot Ankle Surg*, 20(3), 201-207.
49. Schulze, D., Heiland, M., Thurmann, H., & Adam, G. (2004). Radiation exposure during midfacial imaging using 4- and 16-slice computed tomography, cone beam computed tomography systems and conventional radiography. *Dentomaxillofac Radiol*, 33(2), 83-86.
50. Schulze, R., Heil, U., Gross, D., Bruellmann, D. D., Dranischnikow, E., Schwanecke, U., & Schoemer, E. (2011). Artefacts in CBCT: a review. *Dentomaxillofac Radiol*, 40(5), 265-273.

51. Siewerdsen, J. H., & Jaffray, D. A. (2001). Cone-beam computed tomography with a flat-panel imager: magnitude and effects of x-ray scatter. *Med Phys*, 28(2), 220-231.
52. Stehling, C., Souza, R. B., Hellio Le Graverand, M. P., Wyman, B. T., Li, X., Majumdar, S., & Link, T. M. (2012). Loading of the knee during 3.0T MRI is associated with significantly increased medial meniscus extrusion in mild and moderate osteoarthritis. *Eur J Radiol*, 81(8), 1839-1845.
53. Takenaga, T., Katsuragawa, S., Goto, M., Hatemura, M., Uchiyama, Y., & Shiraishi, J. (2015). Modulation transfer function measurement of CT images by use of a circular edge method with a logistic curve-fitting technique. *Radiol Phys Technol*, 8(1), 53-59.
54. Tapiovaara, M., & Siiskonen, T. (2008). A PC-based Monte Carlo program for calculating patient doses in medical x-ray examinations (2nd Ed.). 31.
55. Tarver, R. D., Holden, R. W., & Ellis, J. H. (1983). Experimental lung nodule model: CT numbers, nodule size, and actual calcium content. *J Comput Assist Tomogr*, 7(3), 402-406.
56. Tuominen, E. K., Kankare, J., Koskinen, S. K., & Mattila, K. T. (2013). Weight-bearing CT imaging of the lower extremity. *AJR Am J Roentgenol*, 200(1), 146-148.
57. Valentin, J. (2007). The 2007 Recommendations of the International Commission on Radiological Protection. ICRP publication 103. *Ann ICRP*, 37(2-4), 1-332.
58. Yu, L., Vrieze, T. J., Bruesewitz, M. R., Kofler, J. M., DeLone, D. R., Pallanch, J. F., . . . McCollough, C. H. (2010). Dose and image quality evaluation of a dedicated cone-beam CT system for high-contrast neurologic applications. *AJR Am J Roentgenol*, 194(2), W193-201.
59. Zain-Alabdeen, E. H., & Alsadhan, R. I. (2012). A comparative study of accuracy of detection of surface osseous changes in the temporomandibular joint using multidetector CT and cone beam CT. *Dentomaxillofac Radiol*, 41(3), 185-191.
60. Zbijewski, W., De Jean, P., Prakash, P., Ding, Y., Stayman, J. W., Packard, N., . . . Siewerdsen, J. H. (2011). A dedicated cone-beam CT system for musculoskeletal extremities imaging: design, optimization, and initial performance characterization. *Med Phys*, 38(8), 4700-4713.

Chapter 3

3 Three-dimensional cone-beam CT reconstruction in a natural weight-bearing stance using ceiling-mounted x-ray fluoroscopy

3.1 Introduction

Weight-bearing three-dimensional (3D) images (or cross-sectional slices) for investigation of various musculoskeletal diseases have become a recent focus in the medical imaging community. Previous research has demonstrated significant differences between non-weight-bearing and weight-bearing conditions.^{9, 38} In the current clinical setting, weight-bearing radiographs are used to evaluate joint biomechanics of the knee, ankle, and foot.^{2, 23} Although radiographs are used extensively in clinical practice, they are two-dimensional (2D) representations of a three-dimensional (3D) object, which limits their accuracy when detecting complex fractures, patellofemoral abnormalities, or post-operative measurements of total knee arthroplasty (TKA) component positioning.^{8, 20, 50} Recent studies have used clinical computed tomography (CT) or magnetic resonance imaging (MRI) scanners to simulate weight-bearing conditions, but do not allow for standing weight-bearing imaging in a clinical setting, or may overestimate patellofemoral anomalies for surgical realignment surgery.^{15, 32, 44} Furthermore, these studies do not represent the physiological stresses of the joints in a normal weight-bearing situation, and the setup is impractical for routine clinical exams.

Recent advances in cone-beam computed tomography (CBCT) technology have developed dedicated flat-panel cone-beam CT scanners for musculoskeletal imaging that enable weight-bearing imaging of a single-leg in an upright position.^{3, 31, 32, 53} Despite the commercial availability of dedicated diagnostic CBCT scanners (such as the Planmed Verity, described in Chapter 2), many hospitals have difficulty accommodating additional medical imaging equipment due to cost, space, and workflow constraints. A cone-beam computed tomography (CBCT) system created from an existing ceiling-mounted x-ray fluoroscopy system with a digital flat-panel detector has excellent potential to be used for evaluations of static 3D joint positions and orientations of both lower extremities under

natural weight-bearing conditions. A ceiling-mounted CBCT system with adjustable trajectories during image acquisition has the potential to provide excellent initial evaluation of bony anatomical relationships and 3D visualization of bone and joint morphology within the hip, knee, ankle, foot, and spine. The ceiling-mounted system can rotate parallel to the floor, enabling multiple weight-bearing positions for bilateral evaluations of joints in the lower extremity, while producing higher resolution images – at a lower patient dose – when compared to conventional CT.^{25, 26, 34, 42} The lower radiation dose is a result of the CBCT scanner design, which allows for an increased distance of the x-ray source from the torso, since less scattered radiation can interact with radiosensitive organs within the torso.⁴⁸

Gantry rotation for ceiling-mounted systems are subject to geometric imperfections, where the motion of the x-ray source and detector may deviate significantly from a perfect circular trajectory. The geometric imperfections include gravity-induced mechanical flex, bearing irregularities, or vibration that may impact the motion in the centre of rotation during radiographic image acquisition.^{7, 13} Failure to adequately correct for imperfections will result in mis-registration, loss of detail, and image artefacts.²² Previous authors have utilized image-based calibration objects to characterize gantry motion, either concurrently or prospectively.^{4, 13, 52} In these studies, image data was analyzed to generate a full 3D transformation matrix, which includes intrinsic, rotation, and translation matrices. Image-based corrections were established using previously described methods that applied angle-dependent shift corrections that resolve imperfections in two directions.¹³ For the image-based correction, there are three underlying assumptions to be made: (1) deviations from a perfect trajectory are small, (2) long-term reproducibility of gantry motion during rotation is acceptable, and (3) imperfections during gantry rotation are either parallel to the axis of rotation, or tangential to the circle of rotation and perpendicular to the line joining the x-ray source and the detector.¹³ The latter described motion (3) will only produce insignificant changes to magnification; therefore, it will be ignored, as have other investigators in the past.^{6, 13} These assumptions allow perspective geometric calibration to generate a set of angle-dependent image shifts, which can be applied either prior to image reconstruction, or during backprojection using cone-beam backprojection reconstruction algorithms.¹³

In this paper, we characterize and correct for imperfections in gantry motion for resultant CBCT reconstructions generated from a clinical ceiling-mounted x-ray fluoroscopy imaging system with the capability for integrated radiography, dynamic radiographic imaging, and weight-bearing volumetric images. The proposed approach will permit CBCT reconstructions of the hip, knee, ankle, foot, and spine in a natural weight-bearing stance. In addition to CBCT image reconstructions, it will facilitate 2D to 3D image co-registration for dynamic radiographic kinematic analysis. The performance of the flat-panel x-ray detector was also characterized and reported. We presented a quantitative and qualitative assessment of image quality with CBCT reconstructed image volumes with image-based corrections applied. The image quality phantom described in Chapter 2 was used to assess basic imaging parameters such as spatial resolution, linearity, geometric accuracy, uniformity, and image noise. In addition, we generated volumetric reconstructions of a frozen cadaveric knee specimen and a calibration object to demonstrate the clinical significance of this system. Overall, we have presented detailed methodology for characterization of gantry motion, projection image acquisition, and optimization of CBCT reconstructions from a commercially available ceiling-mounted x-ray fluoroscopy system.

3.2 Methods

3.2.1 Data Acquisition

Image acquisitions were performed using a ceiling-mounted single-plane x-ray fluoroscopy system, shown in **Figure 3.1** (Adora RF, Nordisk Røntgen Teknik A/S, Denmark), equipped with a flat-panel detector (CXDI-50RF, Canon) that has a 2688 x 2208 image matrix over a nominal 43 x 35 cm field of view. The flat-panel detector produces a rectilinear detector matrix with pixel sizes of 160 μm and 320 μm for the 1 x 1 and 2 x 2 binning modes, respectively. The nominal x-ray source-to-detector distance, d , was set to 120 cm, with a resulting half-fan angle of at most 9.6° .¹³ A commercial laser measuring device (Bosch GLM 10, USA) was attached to the x-ray tube housing on the focal spot marker to verify the SDD stability of the ceiling-mounted gantry during rotation. For data acquisition, the initial position of the x-ray fluoroscopy system was set with an automated positioning feature that saves any source-detector orientation into

memory. Reproducibility of the automated positioning feature was determined with geometric projection matrices to have a 400 μm standard deviation. Therefore, image-based geometric calibrations were acquired prior to image projection data acquisitions.

Images were acquired using the cine-radiographic mode at 15 frames/s during gantry rotation, with speeds up to 14° per second. Consequently, images can be obtained in $\sim 1^\circ$ intervals around the object over the full angular range of 540° . During rotation of the ceiling-mounted gantry, a total of 576 projections can be acquired in approximately 40s. Each x-ray exposure triggers a custom-designed x-ray detector that encodes the angular position of the gantry based on values from a potentiometer located in the gantry's rotation motor. All images were corrected for pixel-to-pixel sensitivity variation before reconstruction, through the application of a bright-field image. Projection images of the image quality phantom were acquired at approximately 0.681° per projection using 120 kVp tube voltage, 100-200 mA tube current, and 1 ms exposure time, resulting in 0.1-0.2 mAs per exposure (31 mAs- 62 mAs, $n = 300$). The frozen cadaveric specimen, containing fifty-four, 0.8mm diameter zirconium dioxide beads ($n = 54$) implanted into the cruciate and collateral ligaments, was scanned in an upright position at approximately 0.933° per projection using 85 kVp tube voltage, 250 mA tube current, and 1 ms exposure time, resulting in 0.25 mAs per exposure (100 mAs, $n = 400$). All projection images were acquired using the 2 x 2 binning mode, resulting in a 1344 x 1104 matrix with 320 μm pixel size.

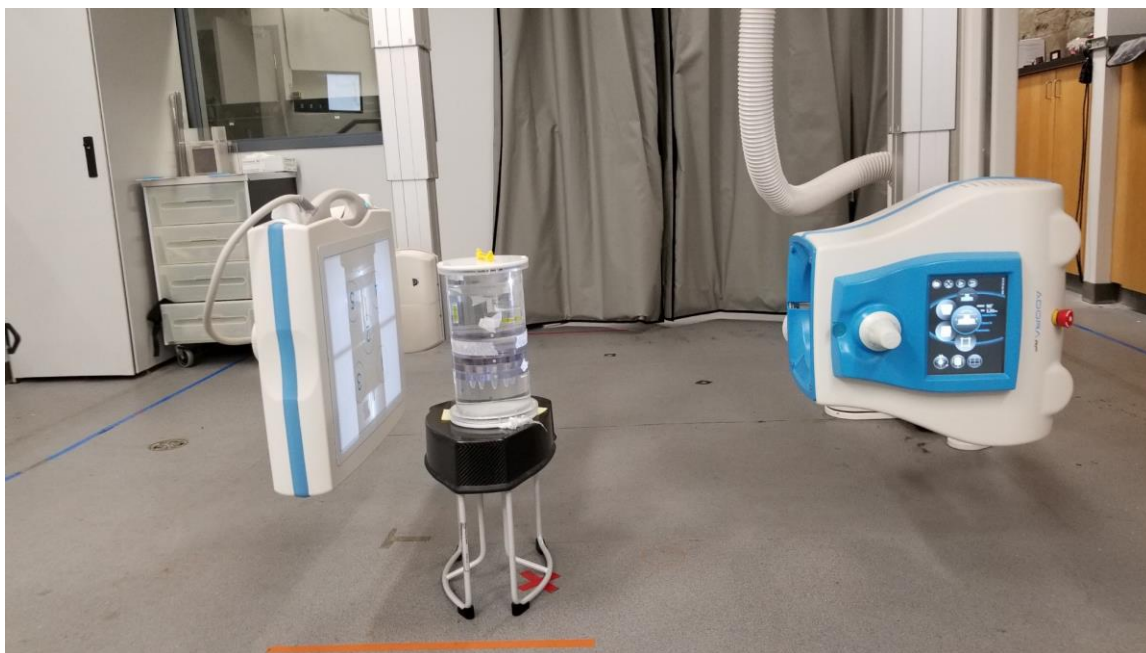


Figure 3.1: Ceiling-mounted x-ray fluoroscopy system setup for an upright acquisition of an image quality phantom.

3.2.2 Flat-panel detector linearity

The flat-panel x-ray detector linearity was evaluated with subsequent exposures of copper sheets with increasing thickness. A total of twenty images ($n=20$) were obtained, where copper sheets between 0.16 mm and 0.26 mm added in succession between each exposure. Using SPEKTR,³⁹ an x-ray spectrum was generated using the kVp, inherent filtration, and added filtration to define the x-ray spectrum characteristics for each copper sheet added. A one-phase decay non-linear regression was used to evaluate the relationship between the measured analog-to-digital units (ADUs), measured bright-field corrected ADUs, copper thickness, and estimated x-ray photon fluence using GraphPad Prism 6.0 (GraphPad Software, San Diego, CA).

3.2.3 Ceiling-mounted gantry motion characterization

A commercially available 3D printer (Dremel® Idea Builder, USA) was used to print a custom-designed calibration object, shown in **Figure 3.2**, using fused deposition printing in polylactic acid (PLA) plastic. The 3D printed calibration cube was designed to be mechanically stable, well-conditioned, and radiolucent to easily identify beads

throughout all projection images. The 3D printed calibration cube contains nine 0.8 mm diameter tantalum marker beads that were placed with a nominal bead spacing of 130 mm to minimize possible overlap of beads in projection images. Marker bead spacing was verified to be 129.56 ± 0.34 mm in a dedicated radiostereometric analysis (RSA) lab. Due to the high number of projections and marker beads, radio-opaque marker beads were tracked using open-source software (XMA Lab 1.5.0, Brown University, USA) to obtain their 2D coordinates from each projection image.²⁴ Initial marker bead detection is performed by clicking near each bead to generate a region of interest (ROI). The software analyzes, optimizes the ROI, and determines the marker position as the centre of the circle closest to the clicked position. For automatic marker bead tracking over time, XMA Lab uses template matching combined with a penalty score based on the distance to the predicted position of the marker.²⁴ Afterwards, optimization of marker detection was required to improve sub-pixel accuracy of marker positions by fitting a polynomial with Gaussian weight to the image intensity.^{24, 40}

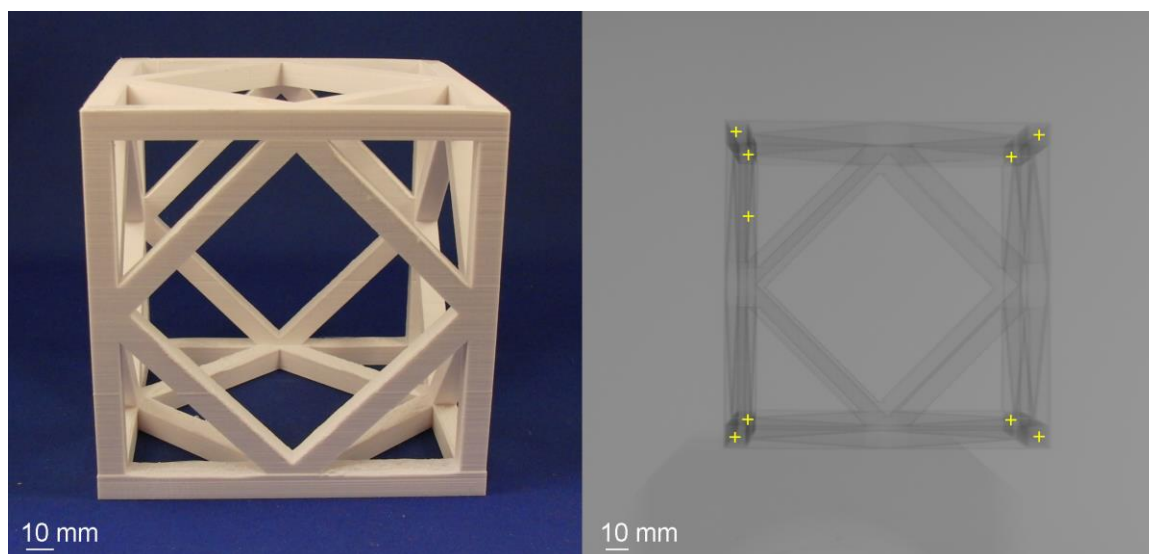


Figure 3.2: Image of the 3D-printed calibration phantom (left) with a sample x-ray projection image (right) showing the locations of each marker bead at each vertex were used to characterize gantry motion.

The 3D printed calibration cube was used to define the 2D-3D relationship between 2D pixels (U, V) on a radiographic image and the 3D voxel (X, Y, Z) in the reconstructed image, as shown in **Figure 3.3**. The ceiling-mounted gantry rotates in the direction of β about an effective isocentre. The intrinsic system parameters can be described by (U, V, W), where U and V indicate pixels within the rectilinear matrix, and w describes the location piercing point (U_0, V_0, W_0) on the detector. These intrinsic parameters are assumed to be constant throughout an image acquisition since this coordinate system travels within the detector during rotation. Extrinsic parameters are described by (X, Y, Z), where (X_0, Y_0) define the mean centre of rotation, and Z_0 is the mean axis of rotation for the system.¹³ Three types of deviations from the perfect orbital trajectory that may occur during rotation include: (1) $\tau(\beta)$ are displacements of the Z -axis perpendicular from the W -axis on the detector, resulting in deviations of u on the detector, (2) $\xi(\beta)$ are deviations of the Z -axis parallel to axis of rotation, resulting in deviations of v on the detector, and (3) $\rho(\beta)$ characterizes motion of the piercing point (U_0, V_0, W_0) parallel to the Y -axis. The third type of motion only results in small changes in magnification, so it was neglected as have other researchers in the past.^{6, 13} The geometry of the ceiling-mounted x-ray fluoroscopy system was characterized using a single marker bead, as well as geometric projection matrices. Image quality phantom projection data was reconstructed using a cone-beam convolution-backprojection algorithm similar to that proposed by Feldkamp,¹⁴ but implementing a correction for the minimum scan trajectory (projections were acquired over Π +fan angle ($\sim 220^\circ$) degrees, rather than over 360°). The frozen cadaveric knee specimen was reconstructed using a full orbital trajectory with the same cone-beam convolution-backprojection algorithm. The appearance of zirconium dioxide beads and their resultant artefacts were reduced using a custom forward projection program that creates a mask of the bead locations in the projection images prior to backprojection. Reconstructed image volumes (27 cm length, 32 cm diameter) have isotropic voxels with dimensions of 0.25 mm per side, and a total volume of 0.016 mm³ per voxel.

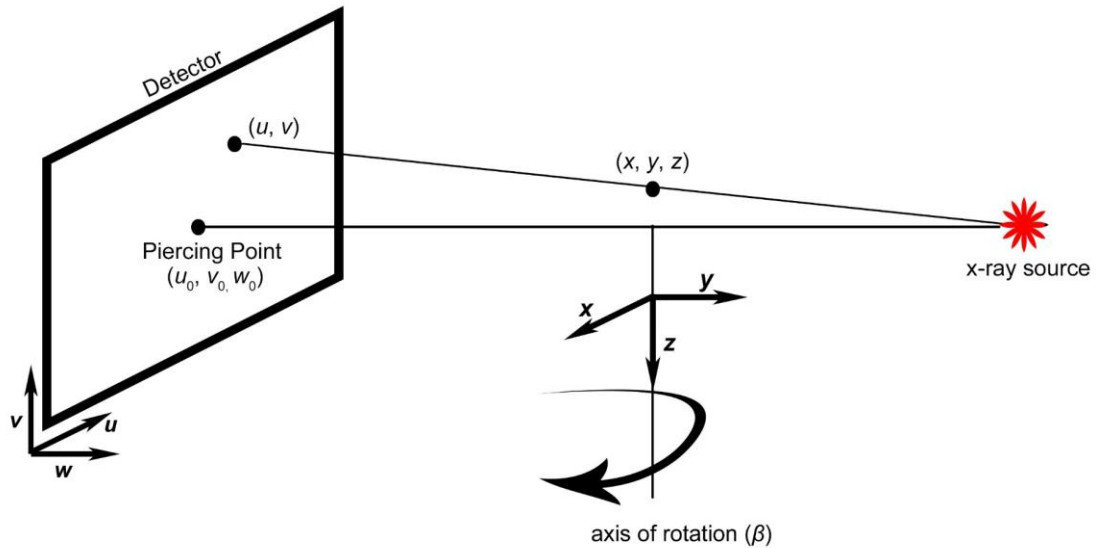


Figure 3.3: Schematic diagram of the acquisition geometry depicting a point projection of an object located in 3D (X, Y, Z) onto a 2D detector (U, V) .

Reproducibility of imperfections during ceiling-mounted gantry motion, over a year, was characterized with five projection-image acquisitions of the 3D printed calibration cube placed near the centre of rotation to minimize motion in the x -direction and was not moved between image acquisitions. In each projection image, the origin of the world coordinate system can be inferred from averaged U, V coordinates of the eight diametrically opposed vertices in the 3D printed calibration cube.⁷ The averaged U, V coordinates represent a sinusoidal curve near the centre of rotation; therefore, we fit this data as a function of image projection number to the equation: $U = a + b \sin(\beta + c)$.¹³ One set of images was acquired with a single high-contrast bead placed within the 3D printed calibration cube to determine if any discrepancies exist between the results of the sinusoidal fit of a single marker bead versus an averaged synthetic marker. The following assumptions were made for the prospective calibration: (1) rotation only occurs in the Z -axis, (2) motion on the Y -axis can be neglected, and (3) intrinsic parameters are consistent throughout a rotation. The residuals resulting from the best-fit sinusoid provide direct estimates of deviations from the perfect circular orbit, and were used to apply

corrections to images before backprojection. In addition, the prospective geometric matrices were generated using the 3D coordinates of the 9 beads and their respective 2D coordinates to characterize gantry motion during rotation within a day.³⁰ Extrinsic projection matrices were computed after fixing the intrinsic parameters to the average for that day.

3.2.4 Effective Dose Estimation

Dose simulations were performed using a commercial Monte Carlo simulation program for calculating patient dose in medical x-ray examinations (PCXMC2.0, STUK, Finland).⁴⁷ This software has been used in previous studies to estimate effective dose to patients.^{5,47} Tube voltage and current remained constant for each projection image; these values were used as inputs to PCXMC. Therefore, the tube voltage and current inputs for the image quality phantom and cadaveric knee specimen were 120 kVp at 0.2 mAs, and 85 kVp at 0.25 mAs, respectively. The x-ray spectrum in PCXMC was set to match the 12° anode angle, as well as the inherent and added filtration (3.05 mm Al, 2.0 mm Al).

3.2.5 Image Quality Assessment

Quality of image volumes was evaluated using a large custom-designed phantom containing modular acrylic plates designed to test individual imaging parameters, as described in Chapter 2.³⁶ The diameter (154 mm) and length (305 mm) of the large phantom was representative of the average diameter and length of a single knee within the field-of-view (FOV). The image quality phantom was placed in an upright position and levelled using an external bubble level. The phantom was used to analyze parameters of image quality, including: spatial resolution, linearity, uniformity, noise, and geometric accuracy. Image volumes were reconstructed from 320 projection images at 0.32 mm isotropic resolution using a cone-beam convolution-backprojection algorithm. The resulting reconstructed 3D images volumes (32 cm width, 27 cm height) were rescaled in Hounsfield units (HU). Image analysis was performed using MicroView image analysis software (Version 2.5.0-3943, Parallax Innovations, London ON), and custom processing software to calculate spatial resolution with slanted-edge images.¹²

3.2.5.1 Spatial Resolution

The image quality phantom evaluated spatial resolution of reconstructed image volumes using 5° slanted-edge images to evaluate the resolution of the image volumes with custom software based on previously described methods.^{12, 36} The image quality phantom contains two orthogonal plates with slanted-edge images to evaluate the slice (Z) (**Figure 3.4b**) and transverse (X-Y) (**Figure 3.7d**) modulation transfer functions (MTF). Ten axial slices from the reconstructed image volume (n = 10 slices) were averaged to reduce noise. Limiting spatial resolution was determined at the point where spatial frequency reaches 10% (referred to as MTF10). Spatial resolution was also assessed with bar patterns (made with alternating sheets of aluminum and Mylar sheets with spacing varying from 0.4 to 2.0 lp/mm). The bar pattern, shown in **Figure 3.4d**, quantitatively and qualitatively estimated the MTF by analyzing the standard deviation in four ROIs (1.5 x 1.5 x 1.5 mm³), followed by a correction with the standard deviation from an area with uniform intensity placed over the bar patterns.¹¹ Calculation of the maximum modulation between materials in the ROI, defined as $M_0 = \frac{|CT_{Al} - CT_{Mylar}|}{2}$, where the averaged CT numbers, from the FOV, for aluminum and Mylar were used.¹⁰

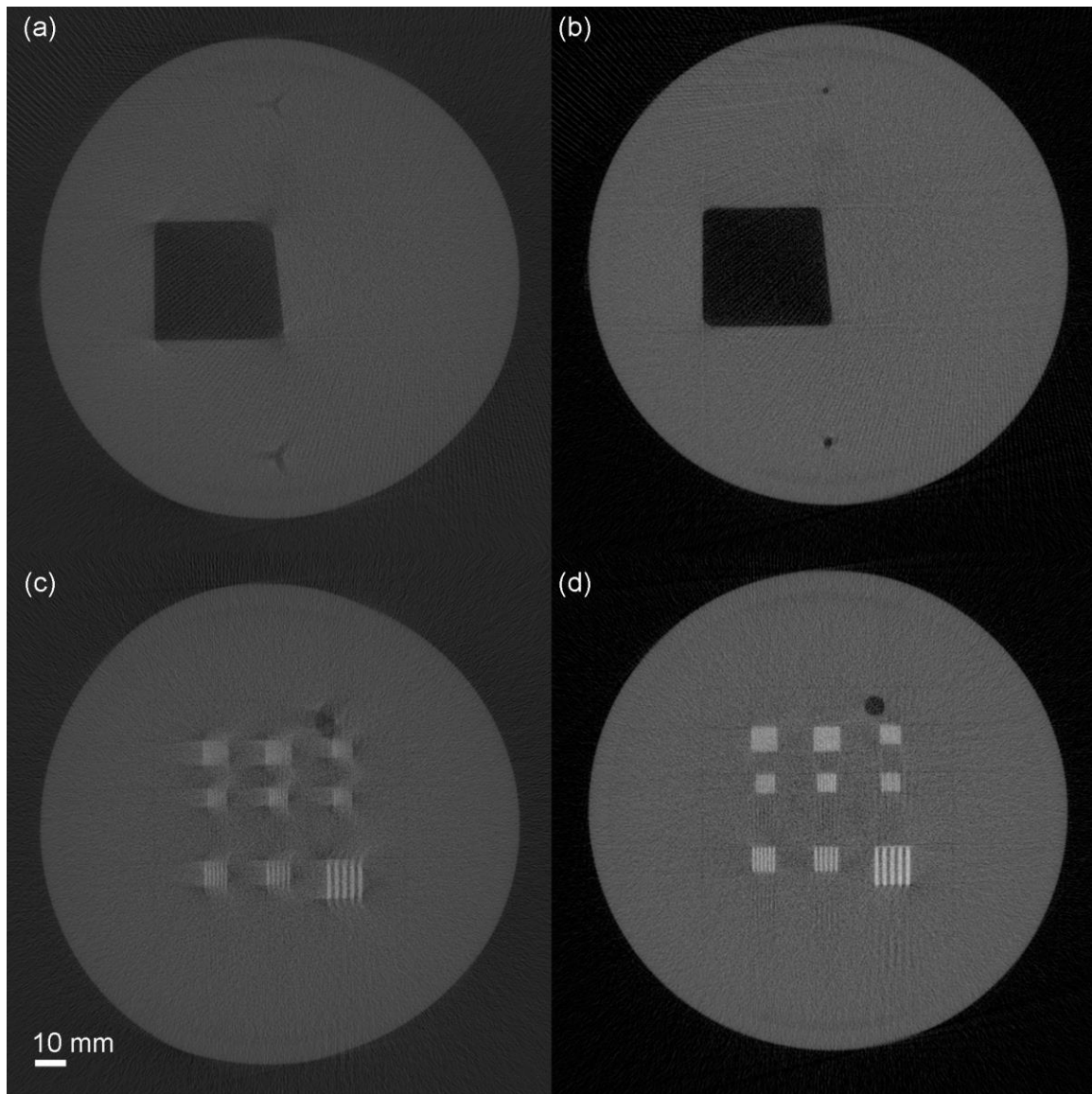


Figure 3.4: Reconstructed slice from the image quality phantom depicting (a) uncorrected and (b) corrected slanted-edge image, showing a 5° from the central axis, and an (c) uncorrected and (d) corrected bar pattern plate, created with alternating aluminum and Mylar sheets.

3.2.5.2 Linearity

The system's linearity was quantified using a modular plate containing known concentrations of bone-mineral densities (ranging from $110 - 1100 \text{ mg cm}^{-3}$) and iodine concentrations (ranging from $0 - 15 \text{ mg ml}^{-1}$).³⁶ In **Figure 3.5b**, reconstructed image

slices within these plates were used to calculate the average CT number within a $2 \times 2 \times 2 \text{ mm}^3$ ROI in the centre of each vial. The relationship between linear attenuation coefficients and signal intensity was determined with linear regression analysis using GraphPad Prism 6.0.

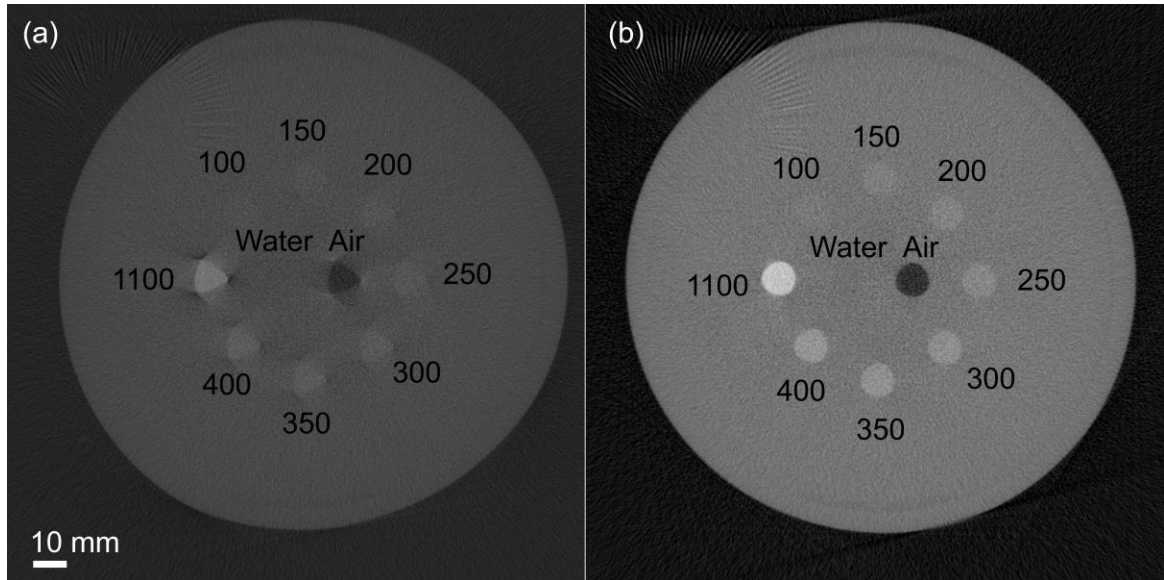


Figure 3.5: Reconstructed (a) uncorrected and (b) corrected linearity slice containing various bone mineral densities representing materials encountered in musculoskeletal imaging, measured in $\text{mg hydroxyapatite cm}^{-3}$.

3.2.5.3 Noise

Image noise was assessed as the standard deviation in the central slice of the reconstructed volume inside a uniform ROI ($10 \times 10 \times 0.32 \text{ mm}^3$), using ROIs shown in **Figure 3.6c**. The relationship between image noise and exposure was measured as a function of photon flux and x-ray exposure that can be fitted with non-linear regression to the equation, $\sigma_{total}^2 = A \times E^{-1} + \sigma_{system}^2$, where σ_{total} is measured noise in HU, E is exposure in mAs, and A and σ_{system}^2 are constant terms, where σ_{system}^2 is the inherent system noise.³⁶ Non-linear fitting was performed using the Levenberg-Marquardt technique (GraphPad Prism 6.0).

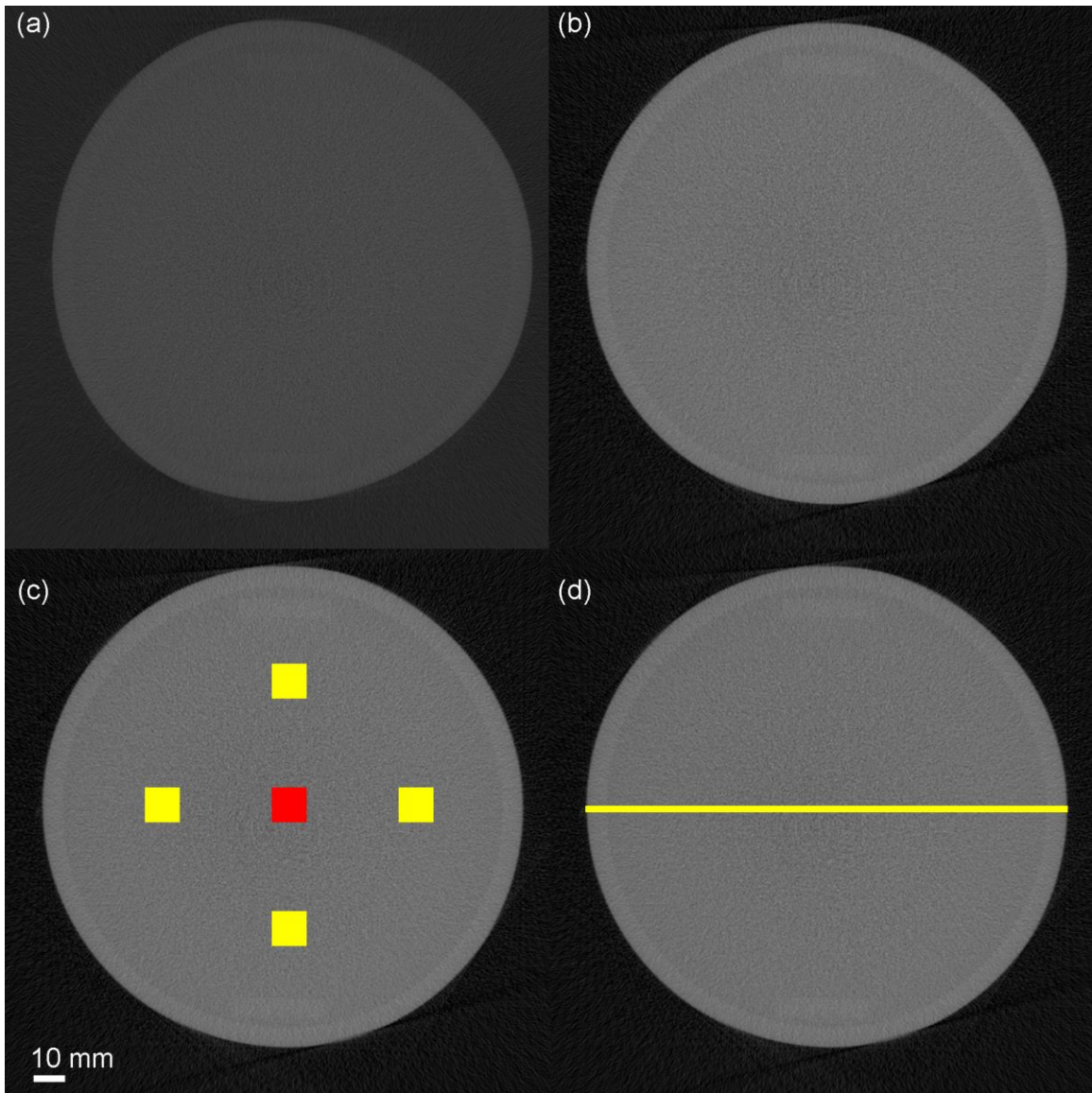


Figure 3.6: (a) Uncorrected and (b) corrected reconstructed slice through an area of uniform density. (c) ROIs used to assess noise (red only) and uniformity (red & yellow). (d) The location of line profile used to analyze variation of CT numbers across the field-of-view (FOV).

3.2.5.4 Uniformity

Uniformity was measured within uniform areas of the reconstructed volume using averaged CT number in four ROIs around the periphery and one ROI in the centre of the reconstructed image quality phantom, shown **Figure 3.6c**. The peripheral ROIs were each

subtracted from the central ROI to determine the system's uniformity. In addition, a line profile was plotted across the central slice to qualitatively assess uniformity, shown in **Figure 3.6d**.

3.2.5.5 Geometric Accuracy

Geometric accuracy was assessed using test plates containing metal beads spaced at a known distance. The image quality phantom can assess geometric accuracy in the axial and transverse directions. Axial geometric accuracy was assessed with four outer beads spaced 40 ± 0.025 mm with an additional bead in the centre. In the transverse direction, a modular plate containing thirty $280 \mu\text{m}$ diameter tungsten-carbide beads (spaced 15 mm apart) were used to evaluate the geometric accuracy. The centroids of each bead (using seeded region growing to automatically extract the beads),³⁵ were used to estimate the distance between neighbouring beads. Image slices used to determine geometric accuracy from both phantoms are demonstrated in **Figure 3.7**.

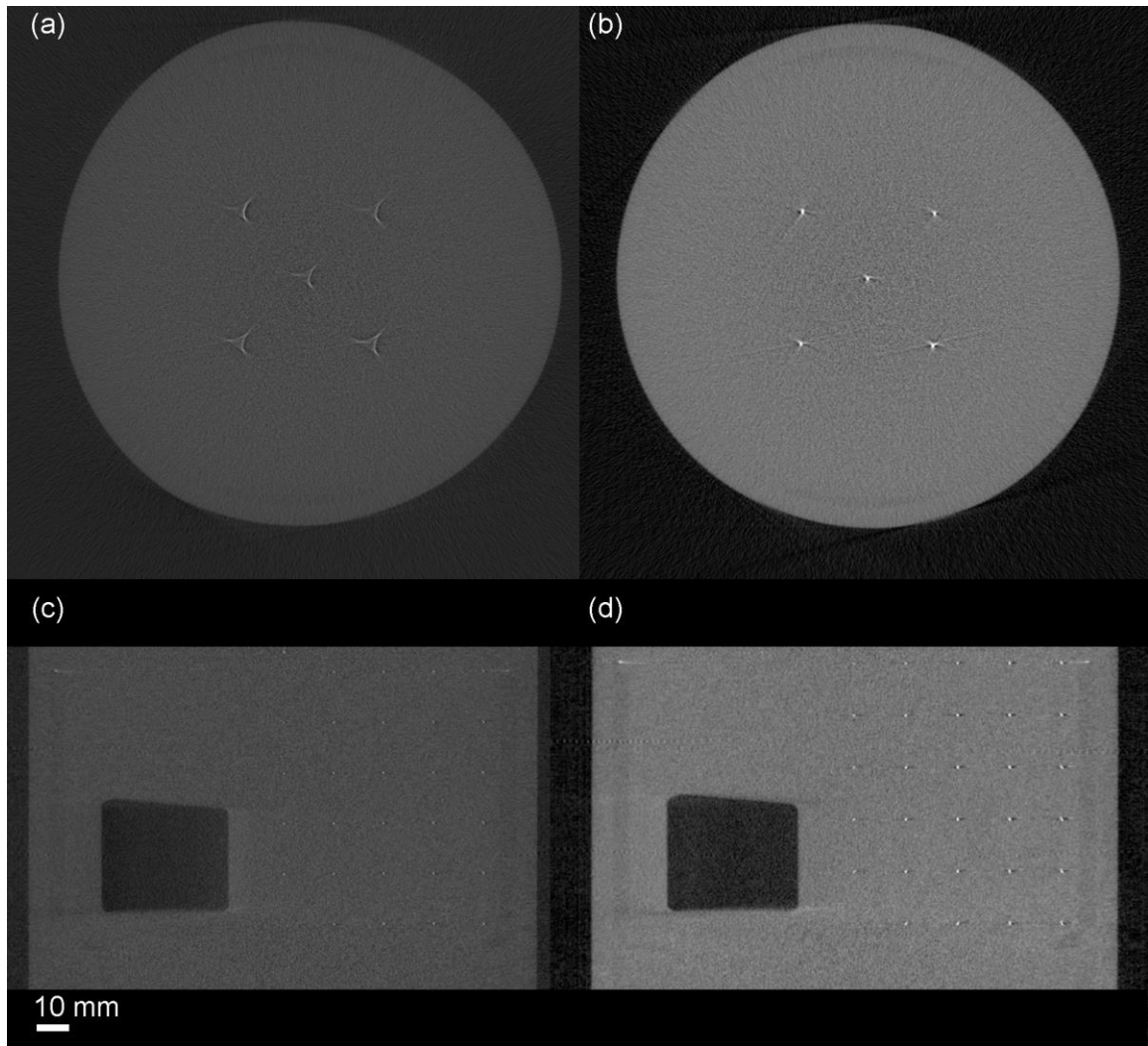


Figure 3.7: Reconstructed (a) uncorrected and (b) corrected slices from image quality phantom with five steel beads in axial plane. (c) uncorrected and (d) corrected slices in X-Y direction with thirty tungsten-carbide beads spaced 15 mm in all directions.

3.3 Results

3.3.1 Flat-panel detector linearity

Figures 3.8a and 3.8b shows the relationship between estimated x-ray photon fluence and increasing copper thickness, as well as the relationship between measured signal intensity and copper thickness, respectively. **Figure 3.8c** illustrates the relationship between estimated x-ray photon fluence and measured signal intensity. Although an unexpected result, this graph demonstrates an exponential response to subsequently increasing x-ray photon fluence. The equation ($Y = -34335 * e^{-1.824*10^{-6}X} + 31185$) was inversed, then applied to all projection images to linearize the detector response to x-ray photon fluence before application of a bright-field image. **Figure 3.8d** shows the detector's linearity response with log-corrected images after application of the previously described equation.

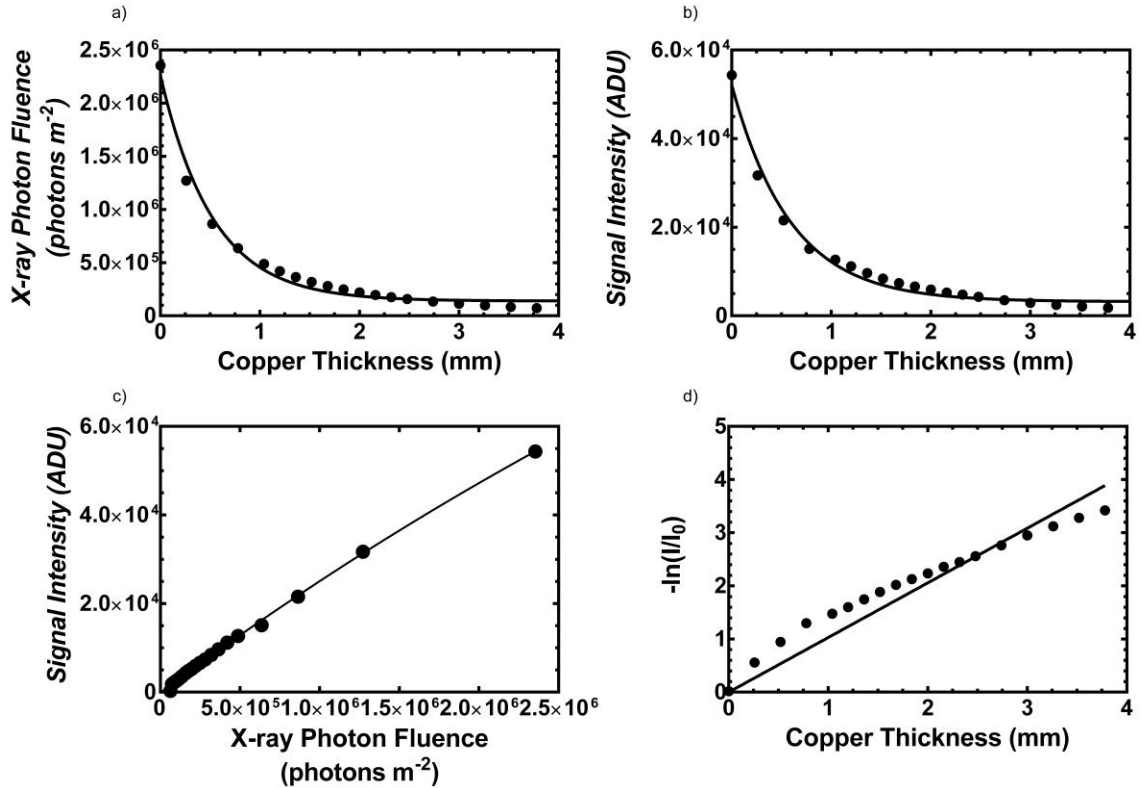


Figure 3.8: Various plots with non-linear best-fit lines illustrating the relationships between (a) x-ray photon fluence and total copper sheet thickness, (b) signal intensity and total copper sheet thickness, (c) signal intensity and x-ray photon fluence, and (d) bright-field corrected signal intensity and x-ray photon fluence.

3.3.2 Ceiling-mounted Gantry Rotation Reproducibility

Figure 3.9a demonstrates the position of the averaged centroid from the 3D-printed calibration cube, in terms of u , along with the best-fit sinusoid determined using linear-least-squares algorithm. Any deviations from a perfect trajectory remain after subtraction of the best-fit sinusoid are shown in **Figure 3.9b**. A paired t-test determined no significant differences between the residuals derived from the line of best-fit using either a single high-contrast marker or averaged U -coordinates from the vertices of the 3D-printed calibrations object ($p=0.27$).

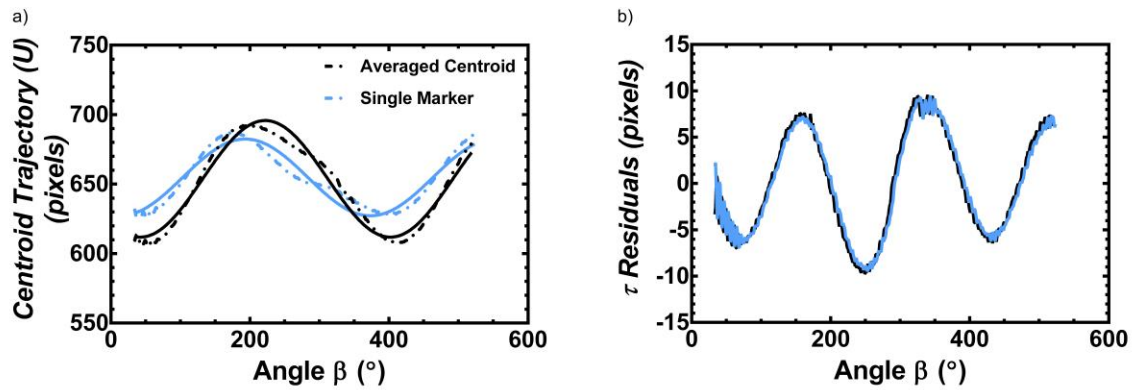


Figure 3.9: (a) Comparison of centroid trajectory of a single high-contrast marker bead versus the averaged U coordinates of the eight diametrically opposed vertices of the 3D printed calibration cube, where the thick line indicates the best-fit sinusoid. (b) The resulting residual plot from a sinusoidal fit is plotted as a function of angle, calculated by subtracting the measured centroid location from the best-fit line.

Figure 3.10a demonstrates the position of the averaged centroid from the 3D-printed calibration object, in terms of u , along with the best-fit sinusoid determined using linear-least-squares algorithm. Any deviations from a perfect trajectory remain after subtraction of the best-fit sinusoid are shown in **Figure 3.10b**. Over five data acquisitions, the gantry motion was highly reproducible, generating a standard deviation of 0.58 pixels (0.19 mm) and a maximum deviation of 10.3 pixels (3.3 mm) from the best-fit line.

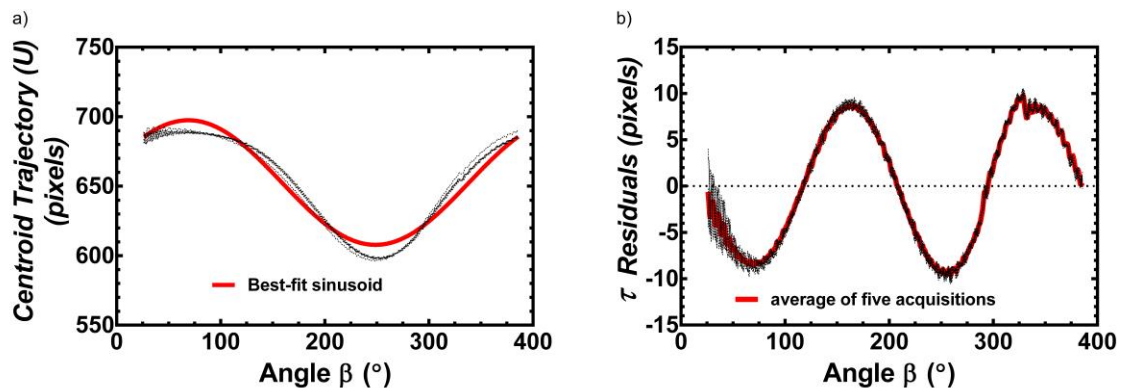


Figure 3.10: (a) Comparison five acquisitions of centroid trajectory of the averaged U coordinates of the eight diametrically opposed vertices of the 3D printed calibration cube, where the thick line indicates the best-fit sinusoid. (b) The resulting residual plot.

Figure 3.11a demonstrates the position of the centroid, in terms of v (representative of vertical motion of the gantry), along with the best-fit sinusoid determined using linear-least-squares algorithm. The gantry motion was highly reproducible, with a standard deviation of 0.29 pixels (0.09 mm) and a maximum deviation of 0.56 pixels (0.18 mm) from the line of best-fit. Residuals from the best-fit line for U and V are shown in **Figure 3.11b**.

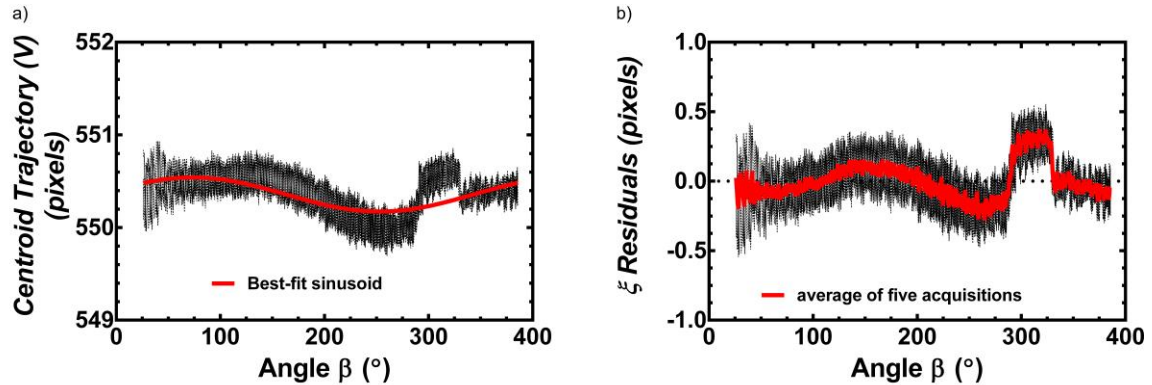


Figure 3.11: (a) Comparison five acquisitions of centroid trajectory of the averaged V coordinates of the eight diametrically opposed vertices of the 3D printed calibration cube, where the thick line indicates the best-fit sinusoid. (b) The resulting residual plot from a sinusoidal fit are plotted as a function of angle, determined by subtracting the measured centroid location from the best-fit line.

Figure 3.12a and 3.12b demonstrate the reproducibility of the centroid residuals throughout a year, in terms of τ and ξ . The gantry motion was highly reproducible, with a standard deviation of 2.47 pixels (0.79 mm), and 0.2 pixels (0.06 mm), respectively. Overall, the ceiling-mounted gantry displays significant, but exceptionally reproducible imperfections for trajectory of gantry motion during image acquisitions within a day, as well as over a year. Reproducibility was characterized by the standard deviation across five scans within a day, where parameters with larger imperfections also displayed larger standard deviations (e.g. ~ 10 pixels for u , and < 0.56 pixels for v). The largest deviations from a perfect circular trajectory appear in the first 100 images, due to vibrations from sudden acceleration of the gantry from 0° to 10° per second. In **Figure 3.12b**, the sudden

shift in v indicates a reproducible mechanical instability, which manifests as a change in vertical position of the gantry as it rotates.

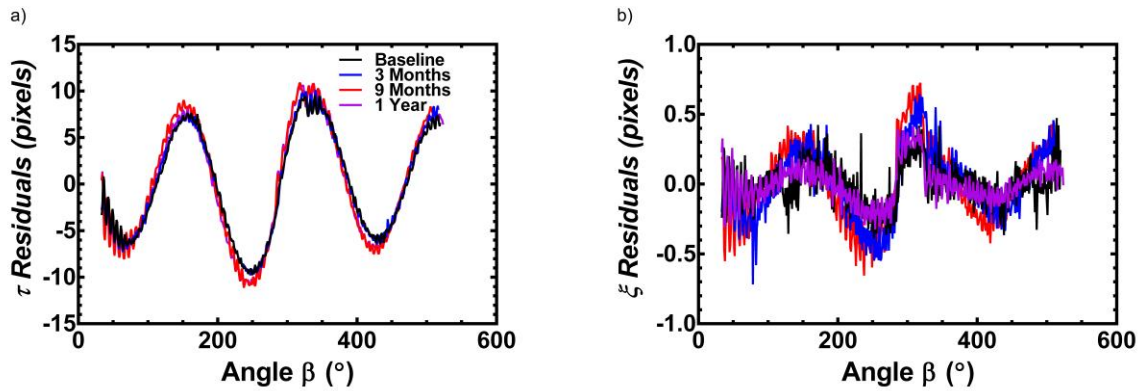


Figure 3.12: Average deviations in (a) τ and (b) ξ as a function of angle, acquired at intervals over a year.

3.3.3 Geometric Projection Matrices Reproducibility

Table 3.1: Geometric projection matrices calculated using the calibration algorithm within a day, summarizing magnitude and reproducibility of geometric imperfections. Geometric imperfections were reported as the maximum deviation from the average value during rotation. Geometric reproducibility was defined as the average standard deviation across multiple acquisitions within a day.

Description	Symbol	Geometric imperfection (maximum deviation from mean value)	Geometric reproducibility (standard deviation across multiple acquisitions)
Piercing Point	u_o	30.18 mm	0.86 mm
	v_o	6.28 mm	0.64 mm
Source-to-Detector Distance	SDD	23.06 mm	0.70 mm
Extrinsic Translation Matrix	T_x	8.76 mm	0.13 mm
	T_y	0.08 mm	0.05 mm
	T_z	9.18 mm	0.13 mm
Extrinsic Rotation Matrix	R_x	154.9°	8.1°
	R_y	2.7°	0.12°
	R_z	154.9°	8.1°

Figure 3.13 demonstrates the reproducibility of extrinsic geometric projection parameters, plotted as the difference from the mean value during the ceiling-mounted gantry orbit. The ceiling-mounted gantry displays significant, but exceptionally reproducible imperfections for geometric calibration parameters during data acquisitions within a day. Maximum deviations and reproducibility of a perfect orbital trajectory during gantry rotation are summarized in **Table 3.1**. Intrinsic geometric calibration parameters, describing location of the piercing point (u_0 , v_0) and SDD, indicate maximum deviations from means were 30.18 mm, 6.28 mm, and 23.06 mm, respectively. Extrinsic geometric translations relative to the geometric calibration object, demonstrated deviations up to 8.76 mm, 0.08 mm, and 9.18 mm for the X-, Y-, and Z-planes, respectively. Extrinsic rotational geometric parameters demonstrated deviations up to 154.9° , 2.7° , and 154.9° for the X-, Y-, and Z-planes, respectively. Due to the large variations within the intrinsic parameters, all computed prospective geometric matrices were deemed unreliable and not used for image-based corrections in this paper. Furthermore, the laser measuring device, described in **Section 3.2.1**, showed SDD deviations up to 1 mm throughout gantry rotation during a data acquisition. Overall, geometric calibration of the ceiling-mounted gantry exceptionally reproducible within a single day, as characterized by the standard deviation across five scans.

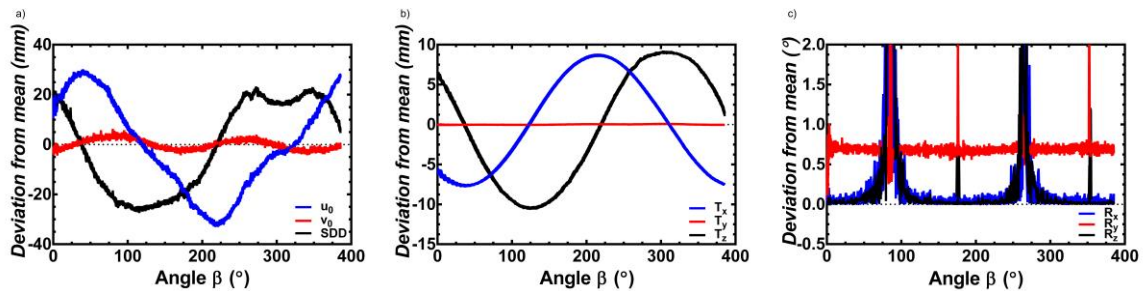


Figure 3.13: Reproducibility of prospective geometric parameters that include: (a) the location of the piercing point (U_0 , V_0) and source-to-detector distance (SDD), (b) extrinsic translations (T_x , T_y , T_z), and (c) extrinsic rotations (R_x , R_y , R_z). Parameters are plotted as a difference from their average value during gantry rotation.

3.3.4 Spatial Resolution

Analysis of slanted-edge images determined the limiting spatial resolution of 1.88 lp/mm and 1.99 lp/mm in the axial and transverse planes, respectively. The system was able to resolve bar patterns up to 2.0 lp/mm. **Figure 3.14** displays MTF profiles obtained from analysis of slanted-edge images and bar patterns.

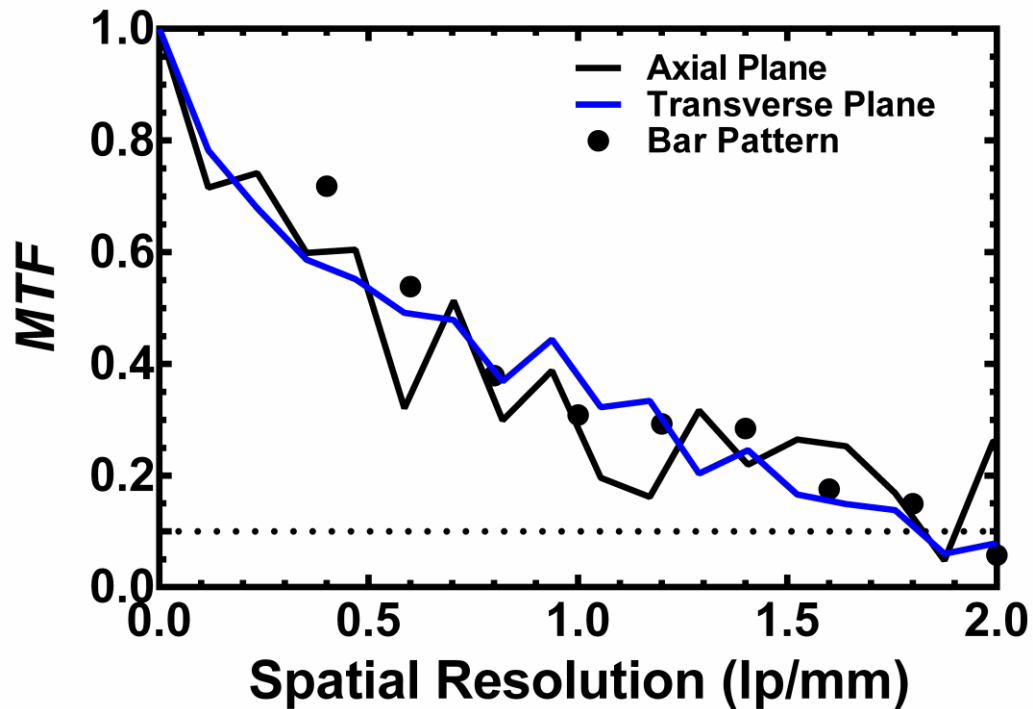


Figure 3.14: Evaluation of modulation transfer function of reconstructed image volumes using bar patterns in the axial direction, as well as slanted-edge images in the axial and X-Y planes.

3.3.5 Linearity

Figure 3.15 contains a plot of the measured CT number (HU) as a function of bone-mineral density. The equation, $S = 1.157 \text{ (HU ml mg}^{-1}) \cdot C + 84.2 \text{ (HU)}$, produced by linear regression revealed a highly linear response from the system, where the signal intensity (S) is a function of increasing iodine concentration (C) in ml mg^{-1} ($R^2=0.9859$). Over the tested range of linear attenuation coefficients, the system demonstrates a high degree of linearity ($p < .01$) in response to signal intensities that will be encountered in clinical musculoskeletal imaging.

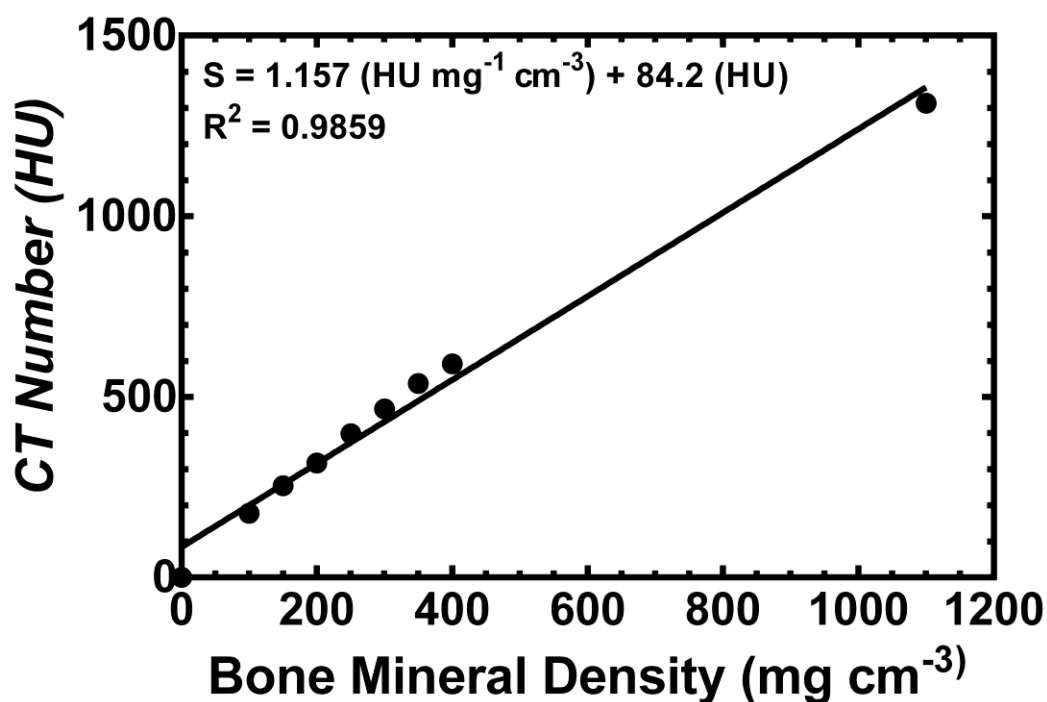


Figure 3.15: Results of linear regression from analysis of bone mineral densities analyzed in the reconstructed linearity plate of the image quality phantom.

3.3.6 Noise

Figure 3.16 demonstrates the relationship between exposure and image noise in reconstructed image volumes, plotted with a best-fit line derived from the equation described in **Section 3.2.5.3**.

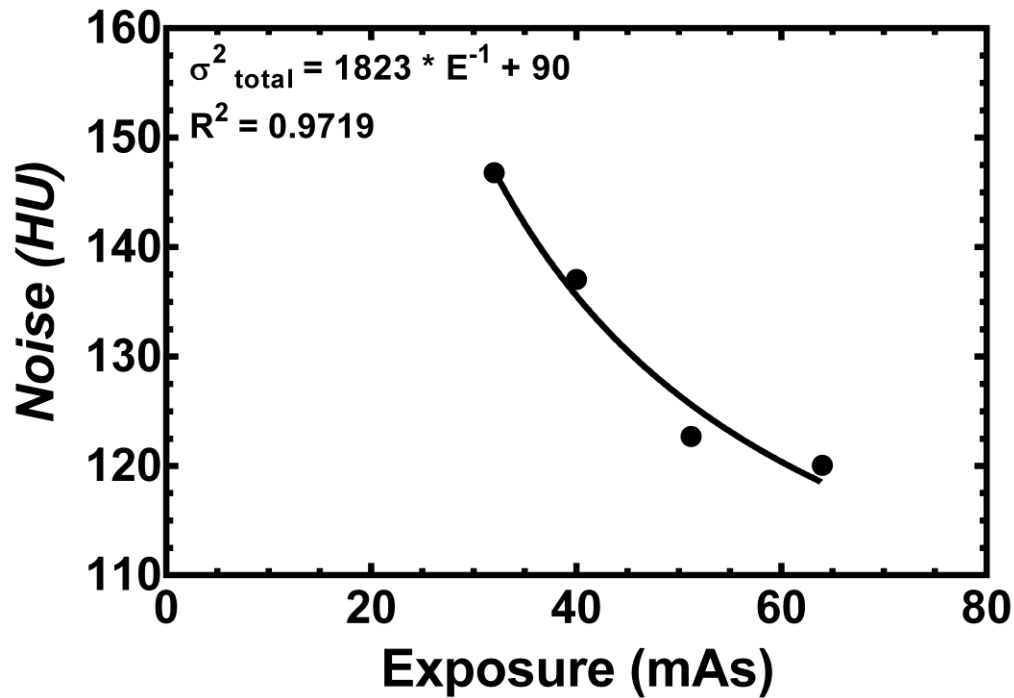


Figure 3.16: Measured noise from resulting image reconstructions, expressed as standard deviation within a uniform ROI, plotted as a function of increasing radiation exposure.

3.3.7 Uniformity

Table 3.2: CT numbers (HU) and standard deviation (HU), measured in one central and four peripheral ROIs for reconstructed image volumes at the central slice. Average difference and average measured standard deviation (\pm SD) were calculated.

	CT #	SD
Centre	7	120
Left	21	101
Top	51	103
Right	52	108
Bottom	29	115
Average difference from the centre	-30.9 ± 15.7	
Average SD	109.4 ± 8.0	

Figure 3.17 shows a line profile plotted across the central slice of a reconstructed image volume. Signal intensities within the central region of the slice demonstrated a uniform response with regards to CT number and image noise. **Table 3.2** contains the measured values used to quantify the system's uniformity from a reconstructed axial slice (120kVp, 51.2 mAs).

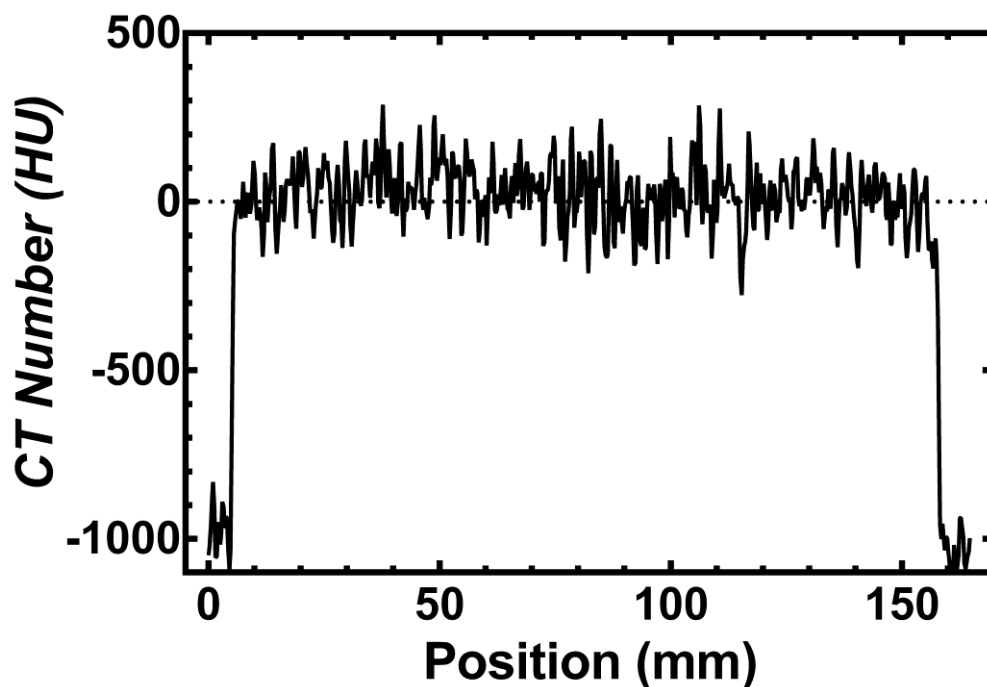


Figure 3.17: Radial signal profile plotted across the central slice of a reconstructed image volume. (120 kVp, 64 mAs)

3.3.8 Geometric Accuracy

Average distance between centroids of the four beads, in the axial direction, was calculated to be 39.87 ± 0.30 mm compared to the nominal 40 mm spacing ($p=0.45$). In the transverse plane, the average distance between the centroids of the tungsten-carbide beads was found to be 15.01 ± 0.10 mm ($p=0.06$) in the (X-Y) plane and 15.01 ± 0.09 mm ($p=0.42$) in the z-direction (slice direction). These results demonstrate excellent in-plane and out-of-plane geometric accuracy for image volumes reconstructed using the ceiling-mounted x-ray radiographic system.

3.3.9 3D Printed Calibration Cube

Figure 3.18 shows various reconstructed axial slices of the 3D printed calibration cube, illustrating the difference between uncorrected and corrected projection images.

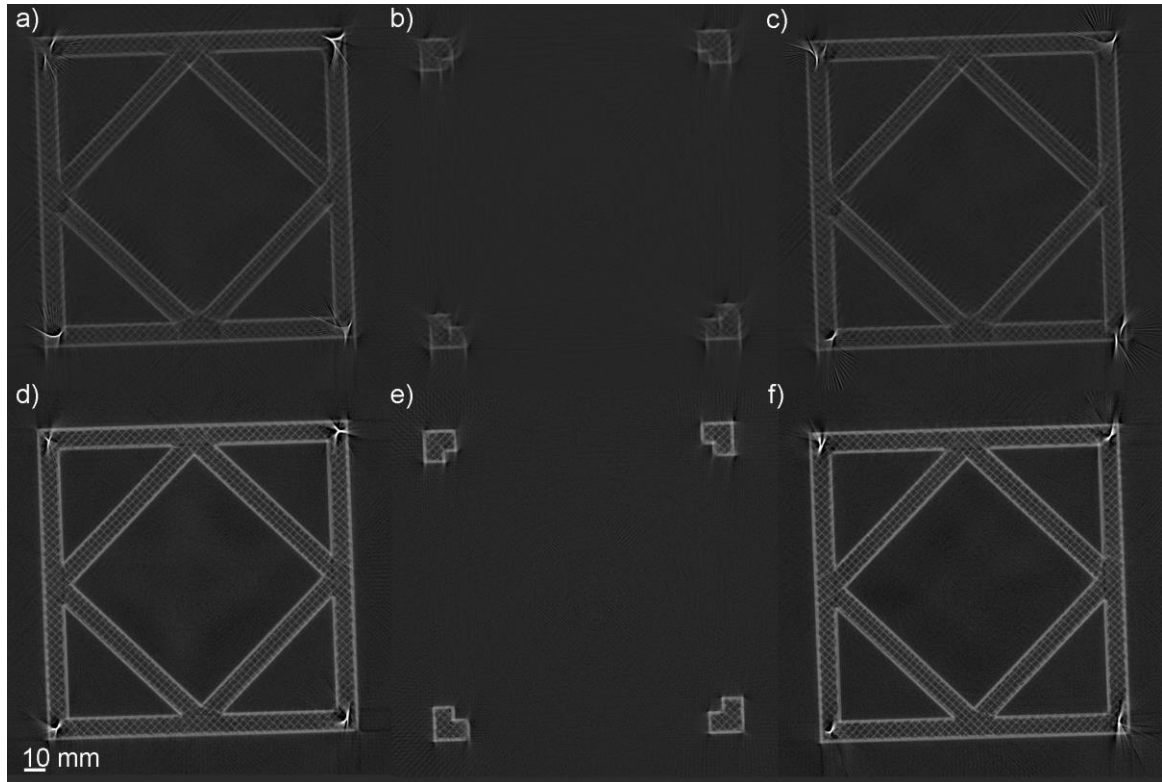


Figure 3.18: Reconstructed axial slices taken from the top, middle, and bottom of uncorrected (a-c) and corrected (d-f) image volumes, respectively.

3.3.10 Cadaveric Specimen

Figure 3.19 shows various reconstructed views in the axial, coronal, and sagittal planes, where the differences between uncorrected, residual-corrected, and artefact-corrected reconstructed image volumes are demonstrated.

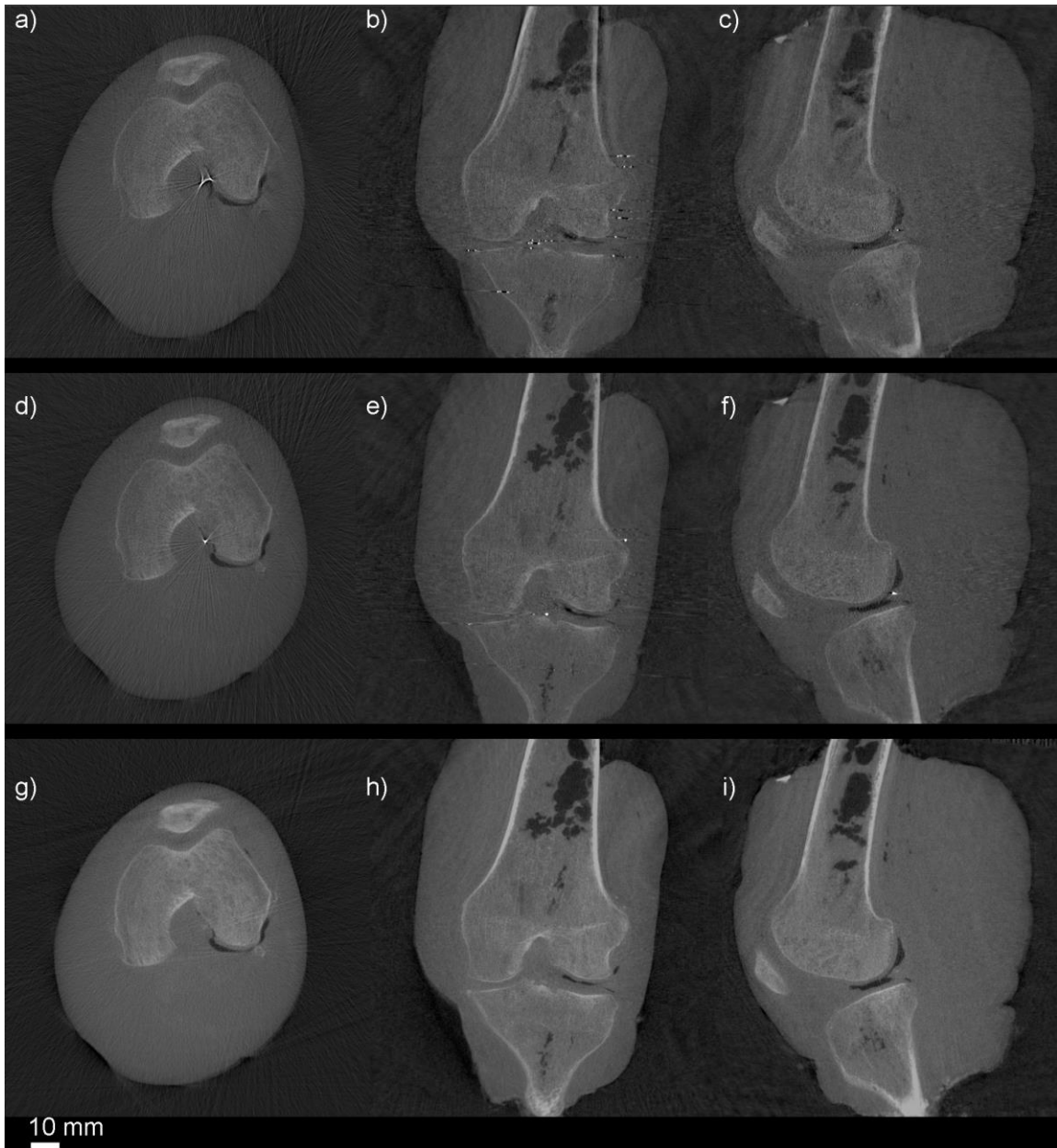


Figure 3.19: Projection views of the frozen cadaveric knee in the axial, coronal, and sagittal planes. The uncorrected (a-c), residual-corrected (d-f), and artefact-corrected (g-i) reconstructed image volumes.

3.3.11 Effective Dose Estimation

Based on ICRP 103 weighting coefficients, the effective dose was calculated to be 20 – 40 μSv for a single weight-bearing ceiling-mounted CBCT scan of both lower extremities using 300 - 576 projection images for volumetric reconstructions (120 kVp, 0.2 mAs per projection). The effective dose for the frozen cadaveric specimen was 14 μSv for single leg while in an upright position using 400 images used in the reconstruction (85 kVp, 0.25 mAs per projection).

3.4 Discussion

We have demonstrated the quantitative and qualitative imaging performance of CBCT reconstructions of the lower extremities resulting from the ceiling-mounted x-ray fluoroscopy imaging system with the capability for integrated weight-bearing radiography and dynamic kinematic imaging. The imaging system can produce accurate weight-bearing CBCT reconstructions with corrections for highly reproducible mechanical imperfections in gantry motion throughout a day. The imperfections in gantry motion were exceptionally reproducible, which allowed for prospective image-based calibration to correct images prior to backprojection.¹³ Although perturbations in gantry motion were highly reproducible within two months, the auto-positioning feature slightly varies the initial position of the source and detector between automatic positions scans; therefore, geometric calibration is required prior to CBCT data acquisition with the ceiling-mounted x-ray fluoroscopy system. The ceiling-mounted x-ray fluoroscopy imaging system can acquire image volumes with a larger FOV (32 cm x 27 cm vs. 16 cm x 13 cm) when compared to current commercially available weight-bearing CBCT scanners. Flexible, yet highly reproducible, trajectories allow for the capability to obtain 3D volumetric images of the hip, knee, ankle, foot, and spine while in a normal weight-bearing stance. In addition to CBCT image volumes, this system can acquire dynamic 2D radiographic images, facilitating 2D to 3D co-registration.

Image quality of reconstructed image volumes are dependent on the accuracy of data from each angular position around the centre of rotation, which must be substantially better than the expected spatial resolution of the final volumetric image.¹³ Although the

ceiling-mounted x-ray fluoroscopy system displays geometric imperfections (maximum side-to-side deviation of 10.3 pixels or 3.3 mm), we have proven these are remarkably reproducible, allowing accurate image-based corrections on a calibration acquired prior to image projection acquisition. Currently, there are two existing approaches for the characterization of gantry motion during CBCT projection image acquisitions, which are either: (1) assume an effective centre of rotation for an equatorial orbit using a single marker bead located near the centre of rotation, or (2) prospective geometric projection matrices to correct for geometric imperfections determined from a minimum of six marker beads, on a view-by-view basis. Respectively, these approaches can be classified as either (1) first-order corrections that account for in-plane variations from the ideal orbital trajectory, or (2) second-order corrections that resolve out-of-plane deviations that may occur.⁷ In our study, we implemented a simplified approach (1) that uses the averaged U , V centroid from the eight vertices in the 3D printed calibration cube to determine in-plane image-based corrections for imperfections in gantry motion, based on a sinusoidal fit of the isocentre.^{7, 13} The techniques allows for simple first-order approximations for displacements from sinusoidal fit, in $\tau(\beta)$ and $\xi(\beta)$ (U and V), to be applied as image-based corrections. During initialization of gantry motion, the largest imperfections were observed due to sudden acceleration from the starting position. Standard deviation of 2.47 pixels (0.79 mm) and 0.20 pixels (0.06 mm) for the respective U and V coordinates for various image acquisitions within a year confirms the exceptional reproducibility of the gantry rotation, which was comparable to previous studies.¹³ A limitation of our study is the 38s acquisition time required to complete one projection image acquisition with the ceiling-mounted x-ray fluoroscopy system. Previous researchers have developed numerous motion compensation techniques that account and correct for involuntary motion during projection image acquisition.^{1, 5, 43} These studies successfully implemented a motion compensation corrections across a range of motion amplitudes, from sub-mm to centimetre drifts.⁴³ Overall, imperfections of the ceiling-mounted gantry rotation were remarkably reproducible over a year, allowing for the use of calibrations previously acquired for image-based corrections.

The second approach, computation of prospective geometric projection matrices, utilizes a minimum of six marker beads to define prospective intrinsic and extrinsic geometric

matrices to describe the relationship between 2D pixels (U, V) on a radiographic image and the 3D voxel (X, Y, Z) in the reconstructed image.^{5, 13, 30, 41, 45} Intrinsic parameters include pixel size ($\Delta U, \Delta V$), source-to-detector distance (SDD), and location of the piercing point on the detector (U_0, V_0); whereas the extrinsic parameters describe rotations and translations of the ceiling-mounted gantry relative to the origin of the geometric calibration object. In our study, this approach yielded unrealistic values for intrinsic geometric parameters that fluctuated simultaneously throughout each image acquisition, as other researchers have observed in the past.⁵¹ Consistent with our approach, intrinsic geometric matrices were averaged and fixed to remain constant, then used to generate the extrinsic projection matrices. The extrinsic translation and rotation matrices were highly reproducible throughout a day, yet vary over time due to small variations in the initial orientation of the source and detector, caused by the auto-positioning feature. The extrinsic rotations in the X- and Z-planes exhibited significant deviations from the average value at two points approximately 180° apart, which indicate that the 3D printed calibration cube may not be well-conditioned for those calibration positions. Other researchers have recommended approximately five times the number of samples to achieve higher accuracy of geometric calibration.¹⁸ According to Li et al.,³⁰ a minimum of 5.5 (6) point correspondences are required to solve for the prospective calibration matrices, and point correspondence data may be inaccurate due to digitization and image noise. Implementation of prospective geometric calibration is computationally intensive, and does not allow use of standard cone-beam backprojection algorithms.¹³

With our approach, we have successfully demonstrated various image quality parameters within a reconstructed image volume, in terms of linearity, spatial resolution, uniformity, noise, and geometric accuracy. Additionally, we have successfully reconstructed a single frozen cadaveric knee specimen in an upright position. Previous work has performed a quantitative analysis CBCT reconstructed image volumes from an O-arm using the same image quality phantom.³⁶ Reconstructed image volumes exhibited a highly linear response over the ranges of densities analyzed, representing the linear attenuation coefficients of cortical bone, cartilage, muscle, and other soft tissues that will be encountered in future studies. The spatial resolution of reconstructed image volumes from the ceiling-mounted gantry surpassed the O-arm in both axial and transverse planes;³⁶

however, spatial resolution differed slightly between axial and transverse plane measurements. This may have been caused by excessive noise in the edge-response function, which influences the derivation of the edge response function to the line spread function when calculating MTF.⁴⁶ High spatial resolution is important for the detection of subtle fractures that do not present on radiographs, and for the visualization of the trabecular architecture of subchondral bone.³⁷ Geometric accuracy within reconstructed image volumes was excellent, indicating reliable and accurate measurements for application to patient-to-image registrations.¹⁶ In clinical practice, extremity CBCT scanners have been successfully used in evaluations of joint arthrography, bone healing, fracture detection, and joint alignment.^{19, 21, 27, 29} Uniformity and noise measurements are dependent on the diameter of the object within the FOV. In our study, reconstructed images volumes displayed a cupping effect on the line profile across the central slice, indicating the occurrence of beam-hardening. The detector used in this study produces images with a 12 bit depth (i.e. 4096 grey levels), but displays non-linear (but correctable) response over all exposures used in the study due to limited dynamic range. In order to reduce noise without increasing radiation dose, enhancement of detector quantum efficiency is essential.²⁸

The effective dose was estimated using a commercial Monte Carlo simulation program for calculating patient dose in medical x-ray examinations. The effective dose was estimated to be 20 μSv per CBCT acquisition reconstructed using 300 projection images (120 kVp, 60 mAs). For the frozen cadaveric specimen, the effective dose was estimated to be 14 μSv while in an upright position reconstructed with 400 projection images (85 kVp, 80mAs) using a full orbital trajectory. The resulting effective dose is comparable to current commercially available weight-bearing CBCT scanners,^{25, 26, 31} and is equivalent to approximately two chest x-rays per projection image acquisition.³³ The stochastic effects of ionizing radiation arising from diagnostic imaging has been associated with a cancer risk coefficient of $5.5 \times 10^{-2} \text{ Sv}^{-1}$, thereby a scan from this ceiling-mounted x-ray fluoroscopy system carries a $1.1 \times 10^{-6} \%$ increase to the stochastic effects of radiation over a lifetime.⁴⁹ The effective dose associated with CBCT acquisitions from a ceiling-mounted x-ray fluoroscopy system is minimal compared to 2.2 mSv, comprising of less than 1% of the average annual total effective dose from background radiation for

Canadian residents.¹⁷ This ceiling-mounted x-ray fluoroscopy system demonstrates potential for weight-bearing imaging of the lower extremity in biomechanically relevant positions to assess the effects of various musculoskeletal treatments, while generating a lower dose when compared to conventional CT.

3.5 Conclusion

We have demonstrated for the first time that a ceiling-mounted single-plane x-ray fluoroscopy system can generate accurate CBCT reconstructions using image-based corrections for highly reproducible imperfections in gantry motion. Implementation of a simple image-shift correction protocol allows the implementation of standard cone-beam reconstruction algorithms to produce accurate 3D reconstructions. Deviations from the perfect orbital trajectory were highly reproducible within a day and over a year, characterized from a sinusoidal fit of a synthetic point at the centre of the projection image, as well as extrinsic geometric projection matrices. An image-quality phantom assessed image quality parameters of reconstructed image volumes in terms of spatial resolution, linearity, geometric accuracy, image noise, and uniformity. The successful reconstruction of an upright cadaveric knee specimen demonstrates the significant clinical potential of this system. The ceiling-mounted x-ray fluoroscopy system allows for a larger FOV compared to currently available CBCT scanners. Future studies will include: image acquisition with an offset detector to increase the FOV, 2D to 3D co-registration for kinematic analysis of the knee during gait, and simultaneous weight-bearing acquisitions of both lower extremities.

3.6 References

1. Berger, M., Muller, K., Aichert, A., Unberath, M., Thies, J., Choi, J. H., . . . Maier, A. (2016). Marker-free motion correction in weight-bearing cone-beam CT of the knee joint. *Med Phys*, 43(3), 1235-1248.
2. Brandt, K. D., Fife, R. S., Braunstein, E. M., & Katz, B. (2010). Radiographic grading of the severity of knee osteoarthritis: Relation of the Kellgren and Lawrence grade to a grade based on joint space narrowing, and correlation with arthroscopic evidence of articular cartilage degeneration. *Arthritis & Rheumatism*, 34(11), 1381-1386.

3. Carrino, J. A., Al Muhit, A., Zbijewski, W., Thawait, G. K., Stayman, J. W., Packard, N., . . . Siewerdsen, J. H. (2014). Dedicated cone-beam CT system for extremity imaging. *Radiology*, *270*(3), 816-824.
4. Cho, Y., Moseley, D. J., Siewerdsen, J. H., & Jaffray, D. A. (2005). Accurate technique for complete geometric calibration of cone-beam computed tomography systems. *Med Phys*, *32*(4), 968-983.
5. Choi, J. H., Maier, A., Keil, A., Pal, S., McWalter, E. J., Beaupre, G. S., . . . Fahrig, R. (2014). Fiducial marker-based correction for involuntary motion in weight-bearing C-arm CT scanning of knees. II. Experiment. *Med Phys*, *41*(6), 061902.
6. Concepcion, J. A., Carpinelli, J. D., Kuo-Petravic, G., & Reisman, S. (1992). CT fan beam reconstruction with a nonstationary axis of rotation. *IEEE Trans Med Imaging*, *11*(1), 111-116.
7. Daly, M. J., Siewerdsen, J. H., Cho, Y. B., Jaffray, D. A., & Irish, J. C. (2008). Geometric calibration of a mobile C-arm for intraoperative cone-beam CT. *Med Phys*, *35*(5), 2124-2136.
8. Dirschl, D. R., & Dawson, P. A. (2004). Injury severity assessment in tibial plateau fractures. *Clin Orthop Relat Res*, *423*(423), 85-92.
9. Draper, C. E., Besier, T. F., Fredericson, M., Santos, J. M., Beaupre, G. S., Delp, S. L., & Gold, G. E. (2011). Differences in patellofemoral kinematics between weight-bearing and non-weight-bearing conditions in patients with patellofemoral pain. *Journal of orthopaedic research : official publication of the Orthopaedic Research Society*, *29*(3), 312-317.
10. Droege, R. T., & Morin, R. L. (1982). A practical method to measure the MTF of CT scanners. *Med Phys*, *9*(5), 758-760.
11. Droege, R. T., & Rzeszutarski, M. S. (1985). An MTF method immune to aliasing. *Med Phys*, *12*(6), 721-725.
12. Du, L. Y., Umoh, J., Nikolov, H. N., Pollmann, S. I., Lee, T. Y., & Holdsworth, D. W. (2007). A quality assurance phantom for the performance evaluation of volumetric micro-CT systems. *Phys Med Biol*, *52*(23), 7087-7108.
13. Fahrig, R., & Holdsworth, D. W. (2000). Three-dimensional computed tomographic reconstruction using a C-arm mounted XRII: image-based correction of gantry motion nonidealities. *Med Phys*, *27*(1), 30-38.
14. Feldkamp, L. A., Davis, L. C., & Kress, J. W. (1984). Practical Cone-Beam Algorithm. *J Opt Soc Am A*, *1*(6), 612-619.

15. Ferri, M., Scharfenberger, A. V., Goplen, G., Daniels, T. R., & Pearce, D. (2008). Weightbearing CT scan of severe flexible pes planus deformities. *Foot Ankle Int*, 29(2), 199-204.
16. Fitzpatrick, J. M., West, J. B., & Maurer, C. R., Jr. (1998). Predicting error in rigid-body point-based registration. *IEEE Trans Med Imaging*, 17(5), 694-702.
17. Grasty, R. L., & LaMarre, J. R. (2004). The annual effective dose from natural sources of ionising radiation in Canada. *Radiat Prot Dosimetry*, 108(3), 215-226.
18. Hartley, R., & Zisserman, A. (2004). *Multiple view geometry in computer vision*. Cambridge: Cambridge University Press.
19. Hirschmann, A., Buck, F. M., Fucntese, S. F., & Pfirrmann, C. W. (2015). Upright CT of the knee: the effect of weight-bearing on joint alignment. *Eur Radiol*, 25(11), 3398-3404.
20. Hirschmann, M. T., Konala, P., Amsler, F., Iranpour, F., Friederich, N. F., & Cobb, J. P. (2011). The position and orientation of total knee replacement components: a comparison of conventional radiographs, transverse 2D-CT slices and 3D-CT reconstruction. *J Bone Joint Surg Br*, 93(5), 629-633.
21. Huang, A. J., Chang, C. Y., Thomas, B. J., MacMahon, P. J., & Palmer, W. E. (2015). Using cone-beam CT as a low-dose 3D imaging technique for the extremities: initial experience in 50 subjects. *Skeletal Radiol*, 44(6), 797-809.
22. Jaffray, D. A., Siewerdsen, J. H., Wong, J. W., & Martinez, A. A. (2002). Flat-panel cone-beam computed tomography for image-guided radiation therapy. *Int J Radiat Oncol Biol Phys*, 53(5), 1337-1349.
23. Kan, H., Arai, Y., Kobayashi, M., Nakagawa, S., Inoue, H., Hino, M., . . . Kubo, T. (2017). Fixed-flexion view X-ray of the knee superior in detection and follow-up of knee osteoarthritis. *Medicine (Baltimore)*, 96(49), e9126.
24. Knorlein, B. J., Baier, D. B., Gatesy, S. M., Laurence-Chasen, J. D., & Brainerd, E. L. (2016). Validation of XMALab software for marker-based XROMM. *J Exp Biol*, 219(Pt 23), 3701-3711.
25. Koivisto, J., Kiljunen, T., Kadesjo, N., Shi, X. Q., & Wolff, J. (2015). Effective radiation dose of a MSCT, two CBCT and one conventional radiography device in the ankle region. *J Foot Ankle Res*, 8(1), 8.
26. Koivisto, J., Kiljunen, T., Wolff, J., & Kortensniemi, M. (2013). Assessment of effective radiation dose of an extremity CBCT, MSCT and conventional X ray for knee area using MOSFET dosimeters. *Radiat Prot Dosimetry*, 157(4), 515-524.
27. Kokkonen, H. T., Suomalainen, J. S., Joukainen, A., Kroger, H., Sirola, J., Jurvelin, J. S., . . . Toyras, J. (2014). In vivo diagnostics of human knee cartilage

- lesions using delayed CBCT arthrography. *Journal of orthopaedic research : official publication of the Orthopaedic Research Society*, 32(3), 403-412.
28. Lee, S. C., Kim, H. K., Chun, I. K., Cho, M. H., Lee, S. Y., & Cho, M. H. (2003). A flat-panel detector based micro-CT system: performance evaluation for small-animal imaging. *Phys Med Biol*, 48(24), 4173-4185.
 29. Lepojarvi, S., Niinimaki, J., Pakarinen, H., & Leskela, H. V. (2016). Rotational Dynamics of the Normal Distal Tibiofibular Joint With Weight-Bearing Computed Tomography. *Foot Ankle Int*, 37(6), 627-635.
 30. Li, X., Da, Z., & Liu, B. (2010). A generic geometric calibration method for tomographic imaging systems with flat-panel detectors--a detailed implementation guide. *Med Phys*, 37(7), 3844-3854.
 31. Ludlow, J. B., & Ivanovic, M. (2014). Weightbearing CBCT, MDCT, and 2D imaging dosimetry of the foot and ankle. *International Journal of Diagnostic Imaging*, 1(2), 1.
 32. Marzo, J., Kluczynski, M., Notino, A., & Bisson, L. (2016). Comparison of a Novel Weightbearing Cone Beam Computed Tomography Scanner Versus a Conventional Computed Tomography Scanner for Measuring Patellar Instability. *Orthop J Sports Med*, 4(12), 2325967116673560.
 33. Mettler, F. A., Jr., Huda, W., Yoshizumi, T. T., & Mahesh, M. (2008). Effective doses in radiology and diagnostic nuclear medicine: a catalog. *Radiology*, 248(1), 254-263.
 34. Neubauer, J., Neubauer, C., Gerstmair, A., Krauss, T., Reising, K., Zajonc, H., . . . Voigt, J. (2016). Comparison of the Radiation Dose from Cone Beam Computed Tomography and Multidetector Computed Tomography in Examinations of the Hand. *Rofo*, 188(5), 488-493.
 35. Otsu, N. (1979). A Threshold Selection Method from Gray-Level Histograms. 5.
 36. Petrov, I. E., Nikolov, H. N., Holdsworth, D. W., & Drangova, M. (2011, 2011/03/03/). *Image performance evaluation of a 3D surgical imaging platform*. Paper presented at the SPIE Medical Imaging.
 37. Posadzy, M., Desimpel, J., & Vanhoenacker, F. (2017). Staging of Osteochondral Lesions of the Talus: MRI and Cone Beam CT. *Journal of the Belgian Society of Radiology*, 101(S2).
 38. Powers, C. M., Ward, S. R., Fredericson, M., Guillet, M., & Shellock, F. G. (2003). Patellofemoral kinematics during weight-bearing and non-weight-bearing knee extension in persons with lateral subluxation of the patella: a preliminary study. *J Orthop Sports Phys Ther*, 33(11), 677-685.

39. Punnoose, J., Xu, J., Sisniega, A., Zbijewski, W., & Siewerdsen, J. H. (2016). Technical Note: spektr 3.0-A computational tool for x-ray spectrum modeling and analysis. *Med Phys*, 43(8), 4711.
40. Rogers, S. S., Waigh, T. A., Zhao, X., & Lu, J. R. (2007). Precise particle tracking against a complicated background: polynomial fitting with Gaussian weight. *Phys Biol*, 4(3), 220-227.
41. Rougee, A., Picard, C., Ponchut, C., & Troussel, Y. (1993). Geometrical calibration of X-ray imaging chains for three-dimensional reconstruction. *Comput Med Imaging Graph*, 17(4-5), 295-300.
42. Sisniega, A., Stayman, J. W., Cao, Q., Yorkston, J., Siewerdsen, J. H., & Zbijewski, W. (2016, 2016/03/22/). *Image-based motion compensation for high-resolution extremities cone-beam CT*. Paper presented at the SPIE Medical Imaging.
43. Sisniega, A., Stayman, J. W., Yorkston, J., Siewerdsen, J. H., & Zbijewski, W. (2017). Motion compensation in extremity cone-beam CT using a penalized image sharpness criterion. *Phys Med Biol*, 62(9), 3712-3734.
44. Stehling, C., Souza, R. B., Hellio Le Graverand, M. P., Wyman, B. T., Li, X., Majumdar, S., & Link, T. M. (2012). Loading of the knee during 3.0T MRI is associated with significantly increased medial meniscus extrusion in mild and moderate osteoarthritis. *Eur J Radiol*, 81(8), 1839-1845.
45. Strobel, N. K., Heigl, B., Brunner, T. M., Schuetz, O., Mitschke, M. M., Wiesent, K., & Mertelmeier, T. (2003, 2003/06/09/). *Improving 3D image quality of x-ray C-arm imaging systems by using properly designed pose determination systems for calibrating the projection geometry*. Paper presented at the Medical Imaging 2003.
46. Takenaga, T., Katsuragawa, S., Goto, M., Hatemura, M., Uchiyama, Y., & Shiraishi, J. (2015). Modulation transfer function measurement of CT images by use of a circular edge method with a logistic curve-fitting technique. *Radiol Phys Technol*, 8(1), 53-59.
47. Tapiovaara, M., & Siiskonen, T. (2008). A PC-based Monte Carlo program for calculating patient doses in medical x-ray examinations (2nd Ed.). 31.
48. Tuominen, E. K., Kankare, J., Koskinen, S. K., & Mattila, K. T. (2013). Weight-bearing CT imaging of the lower extremity. *AJR Am J Roentgenol*, 200(1), 146-148.
49. Valentin, J. (2007). The 2007 Recommendations of the International Commission on Radiological Protection. ICRP publication 103. *Ann ICRP*, 37(2-4), 1-332.

50. Wagenaar, F. C., Koeter, S., Anderson, P. G., & Wymenga, A. B. (2007). Conventional radiography cannot replace CT scanning in detecting tibial tubercle lateralisation. *Knee*, *14*(1), 51-54.
51. Wiesent, K., Barth, K., Navab, N., Durlak, P., Brunner, T., Schuetz, O., & Seissler, W. (2000). Enhanced 3-D-reconstruction algorithm for C-arm systems suitable for interventional procedures. *IEEE Trans Med Imaging*, *19*(5), 391-403.
52. Xu, Y., Yang, S., Ma, J., Li, B., Wu, S., Qi, H., & Zhou, L. (2017). Simultaneous calibration phantom commission and geometry calibration in cone beam CT. *Phys Med Biol*, *62*(17), N375-N390.
53. Zbijewski, W., De Jean, P., Prakash, P., Ding, Y., Stayman, J. W., Packard, N., . . . Siewerdsen, J. H. (2011). A dedicated cone-beam CT system for musculoskeletal extremities imaging: design, optimization, and initial performance characterization. *Med Phys*, *38*(8), 4700-4713.

Chapter 4

4 Conclusions and Future Directions

4.1 Summary of Results

Total knee arthroplasty (TKA) has become the gold standard for treatment of end-stage osteoarthritis (OA) and has seen substantial increases for implementation of this technique. Although TKA is a highly successful, safe, and cost-effective method for treating end-stage OA, many patients continue to have functional limitations.¹³ Approximately 20% of patients still remain unsatisfied with outcomes related to pain relief and functionality.⁴ In some studies, various patients with OA developed new gait patterns to compensate for pain, which consequently result in increased joint loads within the contralateral hip, knee, and ankle.¹² Within ten years of their initial TKA, for approximately 40% of patients, the contralateral knee will undergo accelerated OA disease progression, resulting in a second TKA.^{10, 18} This has led to the implementation of various techniques to study joint motion and loading in the weight-bearing lower extremities to improve patient outcomes, in terms of pain management and restoration of functionality.^{2, 3} Overall, weight-bearing imaging is one of the best methods to evaluate the biomechanical function and OA progression in the knee.¹¹

Previous researchers have used high-speed gait analysis to categorize gait patterns between healthy and OA patients,¹² and identify differences between the operated and non-operated knee joint within the same patient.¹ However, this technique is dependent on the positioning of external reflective markers on the skin, which may not accurately represent motion underlying bony structures,¹⁹ and it cannot provide quantitative measurements about joint micro-motion. Radiography is a non-invasive medical imaging modality that creates a single, static, two-dimensional radiographic image with ionizing radiation of bone and soft tissue within the field-of-view (FOV). In clinical settings, the success of TKA has been evaluated with anteroposterior and lateral radiographs, although reproducibility of these images can be limited by patient positioning and orientation of the detector.¹⁶ Despite the ability to effectively track late-stage disease progression of OA, radiography is a two-dimensional representation of a three-dimensional structure

that cannot accurately distinguish between soft tissue with similar linear attenuation coefficients.¹⁵ Radiostereometric analysis (RSA) utilizes simultaneous bi-planar x-ray exposures to obtain three-dimensional measurements of migration in orthopaedic implants.¹⁷ Although this technique yields accurate measurements, it can only evaluate implanted markers of a single joint in a static image and is limited by a small FOV due to the required intersection of the x-ray sources. Fluoroscopy is another radiographic imaging modality that can obtain multiple images to create a dynamic radiographic video of a patient. This modality enables dynamic single-planar or bi-planar RSA of the lower extremity and has become the gold standard for assessments of soft-tissue artefacts from motion capture gait analysis.^{6, 7, 20} Despite the fact that fluoroscopy can provide three-dimensional measurements of the lower extremities, similar to previously described radiographic imaging modalities, it is still a two-dimensional representation of a three-dimensional object. Computed tomography, unlike previously described radiographic imaging modalities, removes the superimposition of tissues, and distinguishes between two materials with similar densities. Clinical CT scans are unable to obtain functional weight-bearing images due to scanner design limitations. Recent studies have applied an axial load to a patient's leg to simulate weight-bearing in the lower extremity while in a supine position.⁵ Cone-beam computed tomography (CBCT) is based on the same principles as a clinical CT scanner, but allow for a variety of scanner designs that could potentially overcome the limitations of radiography, fluoroscopy, and conventional computed tomography.

In Chapter 2, titled "Quantitative Performance Evaluation of a Peripheral Cone Beam CT Scanner with Weight-bearing Capabilities", we described a technique to quantify image quality parameters of image volumes reconstructed from various algorithms. The hypothesis was that a peripheral cone-beam CT scanner would generate different measurements relating to image quality based on the diameter of the phantom, or reconstruction algorithm implemented was shown to be correct. All image quality measurements were acquired at a 200 μm resolution, and compared to standards set by the manufacturer of the CBCT scanner. Various image quality tests included: spatial resolution, linearity, image noise, uniformity, geometric accuracy, and effective dose. Large- (154 mm) and small- (70 mm) diameter image quality phantoms were scanned ten

times at 96 kVp and 90 kVp, respectively; for image noise, tube current varied from 1 to 12 mA, totalling 12 scans, resulting in exposures ranging from 6 to 108 mAs. Effective dose was estimated using a PC-based Monte Carlo method, as well as a CTDI-based estimate with organ specific weighting coefficients. In this study, we demonstrated that the system's performance exceeds the manufacturer's guidelines for all image quality tests using the small-diameter phantom. As expected, the large-diameter phantom, representing the lower extremity, exhibited increase in image noise and non-uniformity. Overall, the peripheral CBCT imaging system shows potential for weight-bearing 3D volumetric studies for evaluations of musculoskeletal treatments and their impact on joint biomechanics, while providing optimal image quality at a low dose. Our analysis of noise performance vs exposure indicates that exposure should be maintained below approximately 40 mAs, to optimize performance and minimize dose.

In Chapter 3, titled "Three-dimensional computed tomographic reconstruction in a natural weight-bearing stance using ceiling-mounted x-ray fluoroscopy", a technique to generate reconstructed image volumes with a commercially available ceiling-mounted x-ray fluoroscopy while rotating around an object of interest was implemented. The hypothesis that imperfections in ceiling-mounted gantry motion were highly reproducible, and could be used for image-based corrections was shown to be valid. Gantry motion was characterized throughout a year using a 3D printed calibration cube with a modification of the single marker bead method, and was also used to compute prospective geometric calibration matrices using 2D-3D point correspondence. In addition, effective dose resulting from one image acquisition was estimated using a PC-based Monte Carlo simulation. Image-based corrections using the modified single-marker approach were applied before backprojection, and resultant reconstructed image volumes were evaluated using a large-diameter image quality phantom. Within one day, imperfections in gantry motion were remarkably reproducible, resulting in standard deviations 0.58 pixels (0.19 mm) and 0.56 pixels (0.18 mm) for the respective U and V coordinates. Over a year, gantry motion was remarkably reproducible resulting in 2.47 pixels (0.79 mm) and 0.20 pixels (0.06 mm) for the U and V coordinates, respectively. These results indicate imperfections in gantry motion are exceptionally reproducible over a year, and image-based calibrations can be applied to previously acquired datasets. In

this study, we demonstrated this ceiling-mounted x-ray fluoroscopy system can accurately reconstruct image volumes at a dose equivalent to commercially available CBCT scanners.

4.1. Related Future Directions

The validation of image quality resulting from reconstructed image volumes using an image quality phantom to quantify various image quality parameters will enable numerous studies to take place. These studies include comparisons of non-weight-bearing versus weight-bearing joint alignment, *in vivo* visualization of the meniscus, involuntary motion compensation corrections, and evaluations of medial tibio-femoral osteoarthritis. Reconstructed image volumes can provide unmatched biomechanical information of joint loading and alignment in the lower extremity.¹⁴ In clinical orthopaedics, advanced imaging modalities, such as CBCT, have become invaluable for detection of complex fractures that do not present on plain radiographs. Weight-bearing volumetric imaging is ideal for surgical measurements regarding patellar instability since these images can provide a true functional representation of the knee joint.⁹ Other researchers have demonstrated CBCT arthrography can be used clinically within the knee to detect cartilage lesions of varying severity and diagnose the degeneration of tissue surrounding the lesions through the use of contrast-enhanced images.⁸

As described in Chapters 2 and 3, the quantification of various imaging quality parameters resulting from reconstructed image volumes can be used to directly compare reconstructed image volumes from various cone-beam CT scanners. These studies ensure reconstructed image volumes are reliable and accurate portrayals of a joint in the lower extremity while in a weight-bearing position. Therefore, the reconstructed image volumes could be used as computational bone models for finite element modelling or 2D-3D registration in dynamic single-plane flat-plane fluoroscopy to assess joint loading and kinematics. Overall, this thesis developed a novel ceiling-mounted CBCT system with the capability to acquire 3D image volumes of both knees in a weight-bearing position, and quantified various image quality parameters within reconstructed image volumes from a commercially available peripheral CBCT scanner, and our novel ceiling-mounted CBCT system. The novel ceiling-mounted CBCT system provides a unique combination

of 2D dynamic single-planar fluoroscopy, and 3D volumetric weight-bearing imaging. This approach is more broadly applicable to sites that have medical imaging space constraints, and it will facilitate 2D to 3D co-registration with 3D CBCT image volumes and 2D dynamic single-plane images produced by one ceiling-mounted fluoroscopic x-ray system.

4.2. References

1. Alnahdi, A. H., Zeni, J. A., & Snyder-Mackler, L. (2011). Gait after unilateral total knee arthroplasty: frontal plane analysis. *Journal of orthopaedic research : official publication of the Orthopaedic Research Society*, 29(5), 647-652.
2. Andriacchi, T. P., & Mundermann, A. (2006). The role of ambulatory mechanics in the initiation and progression of knee osteoarthritis. *Current opinion in rheumatology*, 18(5), 514-518.
3. Banks, S. A., & Hodge, W. A. (1996). Accurate measurement of three-dimensional knee replacement kinematics using single-plane fluoroscopy. *IEEE Trans Biomed Eng*, 43(6), 638-649.
4. Bourne, R. B., Chesworth, B. M., Davis, A. M., Mahomed, N. N., & Charron, K. D. (2010). Patient satisfaction after total knee arthroplasty: who is satisfied and who is not? *Clin Orthop Relat Res*, 468(1), 57-63.
5. Ferri, M., Scharfenberger, A. V., Goplen, G., Daniels, T. R., & Pearce, D. (2008). Weightbearing CT scan of severe flexible pes planus deformities. *Foot Ankle Int*, 29(2), 199-204.
6. Garling, E. H., Kaptein, B. L., Mertens, B., Barendregt, W., Veeger, H. E., Nelissen, R. G., & Valstar, E. R. (2007). Soft-tissue artefact assessment during step-up using fluoroscopy and skin-mounted markers. *Journal of biomechanics*, 40 Suppl 1, S18-24.
7. Iaquinto, J. M., Tsai, R., Haynor, D. R., Fassbind, M. J., Sangeorzan, B. J., & Ledoux, W. R. (2014). Marker-based validation of a biplane fluoroscopy system for quantifying foot kinematics. *Medical engineering & physics*, 36(3), 391-396.
8. Kokkonen, H. T., Suomalainen, J. S., Joukainen, A., Kroger, H., Sirola, J., Jurvelin, J. S., . . . Toyras, J. (2014). In vivo diagnostics of human knee cartilage lesions using delayed CBCT arthrography. *Journal of orthopaedic research : official publication of the Orthopaedic Research Society*, 32(3), 403-412.
9. Marzo, J., Kluczynski, M., Notino, A., & Bisson, L. (2016). Comparison of a Novel Weightbearing Cone Beam Computed Tomography Scanner Versus a

Conventional Computed Tomography Scanner for Measuring Patellar Instability. *Orthop J Sports Med*, 4(12), 2325967116673560.

10. McMahon, M., & Block, J. A. (2003). The risk of contralateral total knee arthroplasty after knee replacement for osteoarthritis. *J Rheumatol*, 30(8), 1822-1824.
11. Miyazaki, T., Wada, M., Kawahara, H., Sato, M., Baba, H., & Shimada, S. (2002). Dynamic load at baseline can predict radiographic disease progression in medial compartment knee osteoarthritis. *Annals of the Rheumatic Diseases*, 61(7), 617-622.
12. Mundermann, A., Dyrby, C. O., & Andriacchi, T. P. (2005). Secondary gait changes in patients with medial compartment knee osteoarthritis: increased load at the ankle, knee, and hip during walking. *Arthritis Rheum*, 52(9), 2835-2844.
13. Noble, P. C., Gordon, M. J., Weiss, J. M., Reddix, R. N., Conditt, M. A., & Mathis, K. B. (2005). Does Total Knee Replacement Restore Normal Knee Function? *Clinical Orthopaedics and Related Research*, &NA;(431), 157-165.
14. Richter, M., Seidl, B., Zech, S., & Hahn, S. (2014). PedCAT for 3D-imaging in standing position allows for more accurate bone position (angle) measurement than radiographs or CT. *Foot Ankle Surg*, 20(3), 201-207.
15. Romans, L. E. (2010). *Computed Tomography for Technologists: A Comprehensive Text*: Lippincott Williams & Wilkins.
16. Sarmah, S. S., Patel, S., Hossain, F. S., & Haddad, F. S. (2012). The radiological assessment of total and unicompartmental knee replacements. *J Bone Joint Surg Br*, 94(10), 1321-1329.
17. Selvik, G. (1990). Roentgen stereophotogrammetric analysis. *Acta Radiol*, 31(2), 113-126.
18. Shakoor, N., Block, J. A., Shott, S., & Case, J. P. (2002). Nonrandom evolution of end-stage osteoarthritis of the lower limbs. *Arthritis Rheum*, 46(12), 3185-3189.
19. Stagni, R., Fantozzi, S., & Cappello, A. (2006). Propagation of anatomical landmark misplacement to knee kinematics: performance of single and double calibration. *Gait Posture*, 24(2), 137-141.
20. Yuan, X., Ryd, L., Tanner, K. E., & Lidgren, L. (2002). Roentgen single-plane photogrammetric analysis (RSPA.) A new approach to the study of musculoskeletal movement. *J Bone Joint Surg Br*, 84(6), 908-914.

Curriculum Vitae

Rudolphe J. Baronette

Education

- 2015-2018 **M.Sc. Medical Biophysics**
Western University
- 2010-2015 **B.Sc. Medical Radiation Sciences**
McMaster University
- B.Sc. Life Sciences**
McMaster University
- Advanced College Diploma, Medical Radiation Sciences**
Mohawk College

Scholarships and Awards

- 2016 **Cum Laude Abstract Award**
Imaging Network of Ontario
- 2015 **Collaborative Training Program in Musculoskeletal Health
Research Transdisciplinary Bone & Joint Award**
Bone & Joint Institute, Western University
- 2010-2014 **McMaster All-Canadian Academic Scholar**
McMaster University

Abstracts and Presentations

1. **Baronette RJ**, Yuan X, Pollmann SI, Teeter MG, Holdsworth DW. Performance evaluation of a peripheral cone-beam CT scanner with weight-bearing capabilities. Poster presentation at the 2018 Canadian Bone & Joint Conference, London, ON.
2. **Baronette RJ**, Yuan X, Pollmann SI, Teeter MG, Holdsworth DW. Performance evaluation of a peripheral cone-beam CT scanner with weight-bearing capabilities. Poster presentation at the 2018 Imaging Network of Ontario Conference, Toronto, ON.
3. **Baronette RJ**, Yuan X, Teeter MG, Holdsworth DW. Calibrating single-plane fluoroscopy using a 3D printed calibration object. Poster presentation at the 2017 Imaging Network of Ontario Conference, London, ON.

4. **Baronette RJ**, Yuan X, Teeter MG, Holdsworth DW. Calibrating single-plane fluoroscopy using a 3D printed calibration object. Poster presentation at the 2017 London Health Research Day, London, ON.
5. **Baronette RJ**, Yuan X, Teeter MG, Holdsworth DW. Performance evaluation of a peripheral cone-beam CT scanner with weight-bearing capabilities. Poster presentation at the 2016 Canadian Bone & Joint Conference, London, ON.
6. **Baronette RJ**, Yuan X, Teeter MG, Holdsworth DW. Performance evaluation of a peripheral cone-beam CT scanner with weight-bearing capabilities. Poster presentation at the 2016 Imaging Network of Ontario Conference, Toronto, ON.
7. **Baronette RJ**, Yuan X, Teeter MG, Holdsworth DW. Performance evaluation of a peripheral cone-beam CT scanner with weight-bearing capabilities. Poster presentation at the 2016 London Health Research Day, London, ON.

Athletic Achievements

- 1st all-time, 4 x 400m relay, McMaster University.
- 2nd all-time, 300m dash, McMaster University.
- 7th overall, 4 x 200m relay, 2013 Canadian Interuniversity Sport Track & Field Championships, Edmonton, AB.
- 8th overall, 300m dash, 2013 Canadian Interuniversity Sport Track & Field Championships, Edmonton, AB.
- Silver medal, 4 x 200m relay, 2013 Ontario University Athletics Track & Field Championships, Toronto, ON.
- Bronze medal, 4 x 200m and 4 x 400m relay, 2011 Ontario University Athletics Track & Field Championships, Toronto, ON.